To the Graduate Council:

I am submitting herewith a dissertation written by Dah-Liang Guan entitled "Microstructure and Compressive Strength of As-cast and Aged Nb-rich Nb-Al-Ti Intermetallics." I have examined the final copy of this dissertation for form and content and recommend that it be accepted in partial fulfillment of the requirements for the degree of Doctor of Philosophy, with a major in Metallurgical Engineering.

Charlie R. Brooks

Charlie R. Brooks, Major Professor

We have read this dissertation
and recommend its acceptance:

John D. Landes

Peter K. Liaw

Easo P. George

Carl J. McHargue

Accepted for the Council:

Carolyn R. Womack

Associate Vice Chancellor
and Dean of The Graduate School

# MICROSTRUCTURE AND COMPRESSIVE STRENGTH OF AS-CAST AND AGED Nb-RICH Nb-Al-Ti INTERMETALLICS

A Dissertation

Presented for the

Doctor of Philosophy

Degree

The University of Tennessee, Knoxville

Dah-Liang Guan

May 1998

Copyright © Dah-Liang Guan, 1998

All rights reserved

# DEDICATION

The dissertation is dedicated to my parents,

Mr. Yeou-Shu Guan
( 官 有 樞 )

and

Mrs. Gan-Mey Shyu,
( 徐 柑 妹 )

and to my wife,

Yuh-Ju Lan
( 藍 玉 珠 )

For their love, support and encouragement throughout.

# ACKNOWLEDGEMENTS

I would like to express my greatest appreciation and gratitude to my advisor, Dr. Charlie R. Brooks, for his guidance, encouragement and understanding throughout this dissertation research. He has generously advised me during each stage of my doctoral program with wisdom and patience. I am especially indebted to Dr. Carl J. McHargue for the financial support and many suggestions throughout. This research was partially sponsored by the Division of Materials sciences, U. S. Department of Energy, under contract DE–AC05–960R22464 with Lockheed Martin Energy Research Corp., and through the SHaRE Program under contract DE–AC05–760R00033 with Oak Ridge Associated Universities. I would also like to thank my other committee members, Dr. Peter K. Liaw, Dr. John D. Landes and Dr. Easo P. George for their many suggestions and much advice on this dissertation research.

I would like to give my special thanks to Dr. Chain T. Liu, group leader of Alloying Behavior and Design Group, Metals and Ceramics Division, Oak Ridge National Laboratory (ORNL), for allowing me to use the equipment to cast the Group II alloys and for obtaining the chemical analysis. I also thank Dr. Peter K. Liaw for allowing me to use the MTS to conduct the compression tests and for supplying the Group I alloys. Dr. Edward A. Kenik, Microscopy and Microanalytical Science Group, Metals and Ceramics Division, ORNL, is thanked for helping me to conduct the transmission electron microscopy and teaching me useful skills

to get better results under SHaRE program. I am grateful to Mr. Gregory L. Jones for helping me conduct the compression tests and heat treatments. Without their assistance, the research work could not have been completed so smoothly.

Appreciation and particular gratitude are given to Dr. Weiju Ren and his wife, Dr. Shelly Xinlei Ren, who contributed their time and knowledge in the suggestions for the study. Their encouragement and concerns made me feel comfortable to pursue a doctoral degree and helped to make my dream come true.

I am grateful to Mr. F. Stephen Proffitt and his wife, Zelma R. Proffitt. We have become good friends since I came to the United States of America. They assisted me in improving my speaking, listening and writing in English. I appreciate so much that they always helped me whenever I had difficulties and whenever I needed help. I also give thanks to Dr. Jih-Tzong Wang, Dr. Miinshiou Huang, Dr. Su-Ching Chai, Mr. Chiu-Hung Chiu and his wife, Mei-Shin Mong, and my classmates, Mr. Qing He, Mr. John J. Zhu, Mr. Wayne W. Chao and Mrs. Elaine S. Qiao, for their support and encouragement.

Finally, I would like to devote this achievement to my wife, Yuh-Ju Lan, for her constant love, caring, understanding and encouragement. Her long lasting support and help are greatly appreciated. I give my deepest gratitude to my parents, my brothers and sister for their love and support. I also wish to thank my daughter, Ying-Yuh, and my son, Jenn-Kai, for their understanding and patience while looking forward to the day of our family reunion.

# ABSTRACT

As-cast Nb-Al-Ti alloys containing 15 at.% Al and 10, 25 and 40 at.% Ti were tested in compression at 298, 673, 873 and 1173 K (25, 400, 600 and 900°C) at strain rates from $10^{-5}$ to $5x10^{-2}$ $s^{-1}$, to a strain of 5%. The yield strength decreased with increasing temperature for each alloy at all strain rates, and increased with increasing strain rates. The stress-strain curves showed serrated yielding at test temperatures of 673 and 873 K (400 and 600°C) and the lower strain rates. The cause of this was not determined. All alloys showed a yield point drop when tested at 1173 K (900°C), and transmission electron microscopy indicated this was due to recovery occurring during testing. The Ti content (and hence the Nb content) had a marked effect of strength. At a given strain rate and test temperature, the strength increased considerably with increasing Nb content (decreased with increasing Ti content). This was attributed to solid solution strengthening of the ordered B2 structure, and in the 10% Ti (75% Nb) alloy, to the presence of some $\delta$ phase.

Aging treatments were carried out at 873, 1173 and 1373 K (600, 900 and 1100°C) after which compression testing was conducted at 1173 K (900°C) at a strain rate of $10^{-4}$ $s^{-1}$. Aging the 40% Ti alloy at 873 and 1173 K (600 and 900°C) for 10 and 100 hours, and 10 hours at 1373 K (1100°C), did not change the strength significantly. Aging the 10 and 25% Ti alloy for 10 hours at 1173 K (900°C) did not significantly change the strength, but aging for 100 hours increased it about

20%. Aging for 10 hours at 1373 K (1100°C) increased the strength 30 to 40% above that of the as-cast level. For a given alloy, the increase in strength correlates with increasing amounts of $\delta$ formed during aging. As was found for the as-cast condition, there is a marked increase in strength with less Ti (more Nb) content and this is believed due to solid strengthening of the B2 matrix.

# TABLE OF CONTENTS


**I. INTRODUCTION** . . . . . 1

**II. LITERATURE REVIEW** . . . . . 9

2.1 Phase Diagrams . . . . . 9

2.1.1 Pure Niobium . . . . . 9

2.1.2 Ti-Al Phase Diagram . . . . . 10

2.1.3 Nb-Al Phase Diagram . . . . . 11

2.1.4 Ti-Nb Phase Diagram . . . . . 17

2.1.5 Ti-Al-Nb Phase Diagram . . . . . 17

2.2 The Ti-Al Intermetallics . . . . . 22

2.2.1 The TiAl Alloys . . . . . 22

2.2.2 The $Ti_3Al$ Alloys . . . . . 23

2.3 Microstructures of the Ti-Al-Nb Intermetallics . . . . . 25

2.3.1 The A15 ($\delta$) Phase . . . . . 25

2.3.2 The A2 ($\beta$) Phase . . . . . 27

2.3.3 The B2 Phase . . . . . 27

2.3.4 The $\omega$ Phase . . . . . 29

2.3.5 Ti-Rich Aged Alloys . . . . . 29

2.4 Mechanical Properties of the Ti-Al-Nb Intermetallics . . . . . 31

2.4.1 Tensile Behavior of Ti-Rich Alloys . . . . . 31

2.4.2 Fracture Toughness of Ti-Rich Alloys . . . . . 32
2.4.3 Fatigue Properties of Ti-Rich Alloys . . . . . 33
2.4.4 Creep Behavior of Ti-Rich Alloys . . . . . 33
2.4.5 Compressive and Tensile Behavior of Nb-Rich Alloys . . . . 34
2.4.6 Pesudo-twinning in Nb-Rich Alloys . . . . . 34
2.4.7 Strain Aging in Nb-Rich Alloys . . . . . 35

**III. EXPERIMENTAL PROCEDURES . . . . . 36**

3.1 Materials Preparation . . . . . 36
3.2 Heat Treatments . . . . . 37
3.3 Compression Test . . . . . 37
3.4 Optical Microscopy . . . . . 39
3.5 Scanning Electron Microscopy . . . . . 39
3.6 Transmission Electron Microscopy . . . . . 40

**IV. RESULTS AND DISCUSSION . . . . . 41**

4.1 Stress-Strain Behavior of Group I Alloys . . . . . 41
4.2 Serrated Stress-Strain Curves of Group I Alloys . . . . . 46
4.3 Yield Drop Behavior . . . . . 47
4.4 Yield Strength versus Strain Rate of Group I Alloys . . . . . 50
4.5 Microstructures of Group I As-Cast Alloys . . . . . 50
4.6 Microstructures of Compression Tested Specimens of Group I Alloys 57
4.7 Stress-Strain Behavior of Group II Alloys . . . . . 66

4.8 Yield Strength versus Aging Temperature of Group II Alloys . . . . 70

4.9 Microstructures of Compression Tested Specimens of Group II Alloys 70

4.10 Dislocation Morphology . . . . . 114

**V. DISCUSSION OF RESULTS . . . . . 117**

5.1 Microstructure and Mechanical Properties of As-Cast Alloys . . . . 117

5.1.1 Microstructure of As-Cast Alloys . . . . . 117

5.1.2 Microstructure of As-Cast Alloys after Testing at 900°C . . 119

5.1.3 Yield Strength of As-Cast Material at 900°C . . . . . 119

5.2 Microstructure and Mechanical Properties of Heat Treated Alloys . 121

5.2.1 Microstructure of Heat Treated Alloys . . . . . 121

5.2.2 Microstructure of Heat Treated Alloys after Testing at 900°C 123

5.2.3 Effect of Heat Treatment on Yield Strength . . . . . 124

5.3 Summary . . . . . 125

**VI. CONCLUSIONS AND RECOMMENDATIONS . . . . . 128**

6.1 Conclusions . . . . . 128

6.2 Recommendations . . . . . 129

**BIBLIOGRAPHY . . . . . 131**

**VITA . . . . . 141**

# LIST OF TABLES


2.1 Ti-Al crystal structure data. . . . . 13

2.2 Nb-Al crystal structure data. . . . . 15

2.3 Ti-Nb crystal structure data. . . . . 19

2.4 The phases and notations of Ti-Al-Nb alloys. . . . . 26

3.1 Chemical compositions of group II alloys. . . . . 38

3.2 Heat treatment conditions. . . . . 38

4.1 Compressive yield strength at various temperatures and strain rates. 51

4.2 Compressive yield strength at testing temperature of 900°C and strain rate of $10^{-4}$ $s^{-1}$ for various heat treatment temperatures and holding times. . . . . 71

5.1 Summary of Microstructures of As-Cast Alloys and of alloys after testing at 900°C at a strain rate of $10^{-4}$ $s^{-1}$. The structure after testing is shown in brackets. The time to heat to 900°C and make the test was about 15 minutes. . . . . 118

5.2 Microstructure of heat treated and tested alloys. The structure after testing at 900°C at a strain rate of $10^{-4}$ $s^{-1}$ is shown in brackets. . 122

# LIST OF FIGURES


2.1 Ti-Al phase diagram. . . . . 12

2.2 Nb-Al phase diagram. . . . . 14

2.3 Ti-Nb phase diagram. . . . . 18

2.4 Ti-Al-Nb phase diagram at 1473 K (1200°C). Note $\star$ locates the investigated alloys. . . . . 21

2.5 The schematic structure diagram of A15 unit cell. . . . . 27

2.6 The schematic structure diagram of B2 unit cell. . . . . 28

4.1 Compressive stress versus strain curves of Nb-15Al-10Ti alloys. . . . 42

4.2 Compressive stress versus strain curves of Nb-15Al-25Ti alloys. . . . 43

4.3 Compressive stress versus strain curves of Nb-15Al-40Ti alloys. . . . 44

4.4 Magnified compressive stress-strain curve of Nb-15Al-25Ti tested at 600°C at a strain rate of $10^{-4}$ $s^{-1}$ showing serrated behavior. . . . 48

4.5 Compressive yield strength versus strain rate for group I alloys. . . 52

4.6 Microstructure of the as-cast Nb-15Al-10Ti alloy. A structure has formed at the grain boundaries, and its distribution in not homogeneous. . . . . 53

4.7 Microstructure of as-cast Nb-15Al-10Ti alloy showing details of the side-plates which have grown from the grain boundaries. . . . . 55

4.8 Microstructure of the as-cast Nb-15Al-10Ti alloy showing cracks in the grain boundary layer. . . . . 56

4.9 Microstructure of the as-cast Nb-15Al-40Ti alloy showing single phase. 56

4.10 Microstructure of the as-cast Nb-15Al-10Ti alloy after compression testing at 900°C at a strain rate of $5x10^{-2}$ $s^{-1}$. Note cracking along grain boundary phase. . . . . 58

4.11 Microstructure of the as-cast Nb-15Al-10Ti alloy after compression testing at 900°C at a strain rate of $5x10^{-2}$ $s^{-1}$, showing what appears to be additional growth of the side-plates during testing. The time at 900°C was about 5 min. . . . . 58

4.12 Areas such as noted in Figure 4.10 showing extensive cracking of the grain boundary $\delta$ phase. . . . . 59

4.13 Microstructure of the as-cast Nb-15Al-10Ti alloy after compression testing at 900°C at a strain rate of $10^{-5}$ $s^{-1}$. The time at 900°C was about 90 min. . . . . 60

4.14 Details of the side-plates in Figure 4.13 showing what appears to be growth from the tips, presumably occurring during the 90 minutes testing period. . . . . 60

4.15 Unetched microstructure of the Nb-15Al-25Ti alloy, tested at room temperature and a strain rate of $10^{-4}$ $s^{-1}$, showing grain boundary cracks. . . . . 62

4.16 Micrograph of Nb–15Al–40Ti alloy tested at 600°C and strain rate of $10^{-5}$ $s^{-1}$. (a) DF image showing APB obtained using $<001>_{B2}$ type superlattice reflection. (b) The corresponding SAD pattern taken in $<001>_{B2}$ zone axis showing B2 type superlattice spots. . . 63

4.17 Micrograph of Nb–15Al–40Ti alloy tested at 600°C and strain rate of $10^{-5}$ $s^{-1}$. (a) BF image showing dislocations tangled and crossed. (b) The corresponding SAD pattern taken in $[012]_{B2}$ zone axis. . . . 64

4.18 Micrograph of Nb–15Al–40Ti alloy tested at 900°C and strain rate of $10^{-4}$ $s^{-1}$. (a) BF image showing dislocations tangled and scattered. (b) The corresponding SAD pattern taken in $<011>_{B2}$ zone axis showing B2 type superlattice spots. . . . . 65

4.19 Compressive stress versus strain curves of Nb-15Al-10Ti group II alloys tested at 1173 K (900°C) and a strain rate of $10^{-4}$ $s^{-1}$. . . . . 67

4.20 Compressive stress versus strain curves of Nb-15Al-25Ti group II alloys tested at 1173 K (900°C) and a strain rate of $10^{-4}$ $s^{-1}$. . . . . 68

4.21 Compressive stress versus strain curves of Nb-15Al-40Ti group II alloys tested at 1173 K (900°C) and a strain rate of $10^{-4}$ $s^{-1}$. . . . . 69

4.22 Compressive yield strength versus aging temperature for group II alloys tested at 900°C and strain rate of $10^{-4}$ $s^{-1}$. Also shown are data for as-cast group I alloys. The numbers in brackets are estimates of the amount of $\delta$ present before testing. . . . . 72

4.23 Compressive yield stress for the as-cast Nb-15Al-10Ti and Nb-15Al-40Ti alloys compared to data of Shyue *et at.* [20]. The strain rate was $10^{-4}$ $s^{-1}$. . . . . 73

4.24 Microstructures of the as-cast Nb-15Al-10Ti alloy. (a) first heat. (b) second heat. (c) third heat. (d) fourth heat. (e) fifth heat. . . . 74

4.25 Unetched microstructure of the as-cast Nb-15Al-10Ti alloy. (a) BSE image. Brighter image is Nb-rich region in cored due to high cooling rate during solidification. (b) SE image. . . . . 76

4.26 Microstructures of the as-cast Nb-15Al-25Ti alloy. (a) first heat. (b) second heat. (c) third heat. (d) fourth heat. The morphology of (d) is different from others. . . . . 77

4.27 Microstructure of the as-cast Nb-15Al-40Ti alloy showing particles (at A) in the matrix. . . . . 78

4.28 Microstructure of the as-cast and tested Nb-15Al-10Ti alloy. . . . . 78

4.29 Microstructure of the as-cast and tested Nb-15Al-25Ti alloy. . . . . 79

4.30 Microstructure of the as-cast and tested Nb-15Al-40Ti alloy. . . . . 79

4.31 Microstructures of the Nb-15Al-10Ti alloy, heat-treated at 873 K (600°C). (a) holding for 10 hours and as-heat-treated. (b) holding for 10 hours and tested. (c) holding for 100 hours and as-heat-treated. (d) holding for 100 hours and tested. . . . . 80

4.32 Microstructures of the Nb-15Al-25Ti alloy, heat-treated at 873 K (600°C). (a) holding for 10 hours and as-heat-treated. (b) holding for 10 hours and tested. (c) holding for 100 hours and as-heat-treated. (d) holding for 100 hours and tested. . . . . 82

4.33 Microstructures of the Nb-15Al-40Ti alloy, heat-treated at 873 K (600°C). (a) holding for 10 hours and as-heat-treated. (b) holding for 10 hours and tested. (c) holding for 100 hours and as-heat-treated. (d) holding for 100 hours and tested. . . . . 83

4.34 Microstructures of the Nb-15Al-10Ti alloy, heat-treated at 1173 K (900°C). (a) holding for 10 hours and as-heat-treated. (b) holding for 10 hours and tested. (c) holding for 100 hours and tested. . . . . 85

4.35 Microstructures of the Nb-15Al-25Ti alloy, heat-treated at 1173 K (900°C). (a) holding for 10 hours and as-heat-treated. (b) holding for 10 hours and tested. (c) holding for 100 hours and tested. . . . . 86

4.36 Microstructures of the Nb-15Al-40Ti alloy, heat-treated at 1173 K (900°C). (a) holding for 10 hours and as-heat-treated. (b) holding for 10 hours and tested. (c) holding for 100 hours and tested. . . . . 88

4.37 Microstructure of the tested Nb-15Al-10Ti alloy, heat-treated at 1373 K (1100°C) for 10 hours. . . . . 89

4.38 Microstructure of the tested Nb-15Al-25Ti alloy, heat-treated at 1373 K (1100°C) for 10 hours. . . . . 89

4.39 Microstructure of the tested Nb-15Al-40Ti alloy, heat-treated at 1373 K (1100°C) for 10 hours. . . . . 90

4.40 Microstructure of the as-cast Nb-15Al-10Ti alloy, tested at 900°C and strain rate of $10^{-4}$ $s^{-1}$, showing cracks (arrows) in $\delta$ phase. . . 92

4.41 Microstructure of the tested Nb-15Al-40Ti alloy, heat-treated at 900°C for 100 hours, showing $\delta$ phase along the grain boundries and cracks (arrows) in $\delta$ phase. . . . . 92

4.42 Typical EDS obtained from the Figure 4.41 (a) is a spectrum from $\delta$ phase along the grain boundaries. (b) is a spectrum from inside the grain. The ratio of Nb to Ti is 1.33 and 1.24 for (a) and (b), respectively. . . . . 93

4.43 Microstructure of the tested Nb-15Al-25Ti alloys, heat-treated at 900°C for 10 hours. (a) as-heat-treated material. (b) tested material. Note the morphology and the volume fraction of $\delta$ phase are almost the same. . . . . 95

4.44 SEM images taken from TEM sample of the tested Nb-15Al-10Ti alloy, heat-treated at 900°C for 10 hours. (a) the holes are along or in the $\delta$ phase. (b) close-up the hole shows side-plates. The etching solution was 10 vol.% $H_2SO_4$ in methanol. . . . . 96

4.45 Microstructure of as-cast and tested Nb-15Al-10Ti alloy. (a) bright-field image showing subgrain structure. (b) corresponding CBED taken from <111>$_{B2}$ zone axis. (c) corresponding SAD taken from <111>$_{B2}$ zone axis. . . . . 97

4.46 Microstructure of the tested Nb-15Al-10Ti alloy, heat-treated at 600°C for 10 hours. (a) dark-field image showing anti-phase boundaries. (b) corresponding SAD taken from <110>$_{B2}$ zone axis and streaks which may be caused by $\omega$ phase. . . . . 98

4.47 Microstructure of the tested Nb-15Al-10Ti alloy, heat-treated at 600°C for 100 hours. (a) bright-field image showing dislocation dipoles. (b) corresponding SAD taken from <100>$_{B2}$ zone axis showing superlattice spots. . . . . 98

4.48 Microstructure of the as-cast and tested Nb-15Al-25Ti alloys. (a) bright-field image showing periodic parallel tangled dislocations. (b) corresponding SAD taken from <110>$_{B2}$ zone axis. . . . . 99

4.49 Microstructure of the as-cast and tested Nb-15Al-25Ti alloys. (a) bright-field image showing dislocation bands. (b) corresponding SAD taken from <110>$_{B2}$ zone axis. . . . . 100

4.50 Microstructure of the as-cast and tested Nb-15Al-25Ti alloys. (a) bright-field image showing the periodic dislocation bands and dipoles. (b) corresponding SAD taken from <110>$_{B2}$ zone axis. . . . . 101

4.51 Microstructure of the tested Nb-15Al-40Ti alloy, heat-treated at 600°C for 10 hours. (a) bright-field image showing periodic dislocations line-up. (b) corresponding SAD taken from $<110>_{B2}$ zone axis. . . . . 102

4.52 Microstructure of the tested Nb-15Al-40Ti alloy, heat-treated at 600°C for 100 hours, (a) dark-field image showing anti-phase boundaries. (b) corresponding SAD taken from $<100>_{B2}$ zone axis. . . . . 103

4.53 Microstructure of the tested Nb-15Al-40Ti alloy, heat-treated at 1100°C for 10 hours. (a) bright-field image showing dislocation dipoles in B2 matrix. (b) corresponding SAD taken from $<100>_{B2}$ zone axis. . . . . 104

4.54 Microstructure of the tested Nb-15Al-40Ti alloy, heat-treated at 1100°C for 10 hours. (a) bright-field image showing parallel dislocations. (b) close-up of the B2 matrix showing parallel strip structure. (c) corresponding SAD taken from $<100>_{B2}$ zone axis. . . . . 105

4.55 Microstructure of the tested Nb-15Al-40Ti alloy, heat-treated at 1100°C for 10 hours. (a) bright-field image showing dislocation dipoles in the slip band. (b) corresponding SAD taken from $<100>_{B2}$ zone axis. . . . . 106

4.56 Microstructure of the tested Nb-15Al-40Ti alloy, heat-treated at 1100°C for 10 hours. (a) bright-fielf image. (b) corresponding dark-field image showing anti-phase boundaries. (c) corresponding SAD taken from $<100>_{B2}$ zone axis. (d) corresponding CBED taken from $<100>_{B2}$ zone axis. . . . . 107

4.57 Microstructure of the tested Nb-15Al-40Ti alloy, heat-treated at 1100°C for 10 hours. (a) bright-field image showing dislocation intersecting bands. (b) corresponding SAD taken from $<100>_{B2}$ zone axis. . . . . 108

4.58 Dark-field image of the as-cast and tested Nb-15Al-40Ti alloy showing anti-phase boundaries and dislocations taken from $<110>_{B2}$ zone axis. Note dislocations pass through the anti-phase boundaries. . . . . 108

4.59 Microstructure of the tested Nb-15Al-10Ti alloy, heat-treated at 900°C for 100 hours. (a) bright-field image showing dislocation intersecting bands and single dislocations distribute in the matrix. (b) corresponding SAD taken from $<\bar{1}13>_{B2}$ zone axis. . . . . 110

4.60 Microstructure of the tested Nb-15Al-10Ti alloy, heat-treated at 600°C for 100 hours. (a) bright-field image showing $\delta$ phase. (b) corresponding CBED whole patterns with $<100>_{A15}$ zone axis showing 2mm symmetry. (c) corresponding SAD taken from $<100>_{A15}$ zone axis. . . . . 111

4.61 Microstructure of the tested Nb-15Al-25Ti alloys, heat-treated at 1100°C for 10 hours. (a) bright-field image showing $o$ phase in the B2 matrix. (b) corresponding CBED of $o$ phase taken from $<100>_o$ zone axis. (c) corresponding SAD of $o$ phase taken from $<100>_o$ zone axis. . . . . 112

4.62 Microstructure of the tested Nb-15Al-40Ti alloy, heat-treated at 900°C for 10 hours. (a) bright-field image showing $o$ phase. (b) corresponding CBED taken from $<001>_o$ zone axis. . . . . 113

4.63 Microstructure of the tested Nb-15Al-40Ti alloy, heat-treated at 1100°C for 10 hours. (a) bright-field image showing dislocations in the slip bands. (b) corresponding SAD taken from $<110>_{B2}$ zone axis. . . . . 115

4.64 Bright-field image of the tested Nb-15Al-10Ti alloy, heat-treated at 900°C for 100 hours, showing long dislocations tangled structure taken from $<111>_{B2}$ zone axis. . . . . 115

5.1 Compressive yield strength versus Ti content for as-cast samples tested at 900°C at a strain rate of $10^{-4}$ $s^{-1}$. . . . . 120

# CHAPTER I

# INTRODUCTION

In order to increase the efficiency of power producing systems, the operating temperatures must be increased. In some components, such as heat exchangers, turbine blades, steam headers and turbine rotors, the temperatures are expected to be raised to about 1000°C, almost doubling the conventional operating temperatures of approximately 500°C at which many of the current systems are operating.

To develop high-temperature application materials, a cooperative program was initiated among the Air Force, Navy, Army, Defense Advanced Research Projects Agency, National Aeronautics and Space Administration (NASA), and the turbine engine industry which represents virtually all of the current, government-funded research and development in the area of turbine propulsion [1, 2]. The goal is to double turbine propulsion capability by the turn of the century. The approach to achieve this goal focuses on three key areas: aerothermodynamics (more efficient combustion and hotter flow paths), structures (radical new designs), and high-temperature, lightweight materials. In the overall scheme, the role of advanced materials is crucial, for improvements in both aerothermodynamic and structural design are dependent on the continued development and implementation of advanced materials.

Investigations are aimed at understanding materials behavior at ambient and elevated temperatures. Such studies include processing science, strengthening mechanisms, phase transformations, plasticity, creep, fatigue, environmental effects, and dynamic and static fracture. The purpose is to understand the relationships among alloy chemistry, nanostructure, microstructure or macrostructure, material processing and mechanical behavior [2].

The commonly used high temperature materials like superalloys suffer from the disadvantage of high density. Starting with their use in J57 Turbojet rotors in 1954, light-weight titanium alloys have played an important role in performance improvements achieved in gas turbine engines, offering weight reduction opportunities. However, the most advanced titanium alloys like IMI-834 and Ti-1100 lose strength and oxidation resistance at about 870 K (597°C) [3]. Intermetallic phases are responsible for the room temperature as well as high-temperature properties of many commercial alloys, for example: $CuAl_2$ and MgZn in high strength Al-alloys of AA 2XXX and 7XXX type; $Ni_3Al$ in Ni-based superalloys; NiAl in alnico magnets; SbSn in bearing alloys; etc. [4]. Aluminides, silicides and beryllides are some of the important intermetallic systems for high-temperature applications.

Of the numerous material classes being contemplated for structures, titanium aluminides are of primary importance in the 600 to 1000°C range. However, a limited number of titanium aluminide components have been successfully demonstrated in ground test engines.

For the past two decades, many studies have been conducted on ordered intermetallics, a unique class of metallic materials that form long-range ordered crystal structures below a critical temperature in the solid state. Some of these ordered intermetallics, especially those based on aluminides and silicides, possess many attractive properties for structural use at elevated temperatures in hostile environments. These intermetallics have relatively low density, high melting points, good thermal conductivity, and superb high-temperature strength. As a result, these intermetallics are particularly suited for structural applications at elevated temperatures [5, 6, 7, 8, 9, 10]. The Ti-Al system has been identified as a potential candidate material for the Integrated High Performance Turbine Engine Technology (IHPTET) Initiative and the National Aerospace Plane (NASP) program. Alloys based on $Ti_3Al$ ($\alpha_2$) and TiAl ($\gamma$) phases are currently under development.

Although titanium aluminides exhibit a number of attractive properties in the 600 to 1000°C range, they also exhibit some undesirable mechanical properties, such as poor ductility and brittleness at room temperature. There is a general need to achieve high material performance standards while insuring reliability of the structure throughout the design life. Generally, monolithic and composite titanium aluminide materials are intended for applications requiring good high-temperature strength and creep resistance, while maintaining "adequate" ductility, fracture toughness, fatigue behavior, and impact crack resistance at room temperature, and for use in hydrogen-fueled hypersonic vehicles at cryogenic temperatures.

Moreover, the materials must be microstructurally stable over the design life of the structure, and effects of a service environment (such as air, combustion gases, hydrogen) must not seriously degrade the material over its intended life [1, 2, 8].

The materials to be used are required to withstand much dirtier environments than before to cut down the fuel cost and to service the worsening energy crisis. A longer service life is required and it must be more accurately predicted than before. In general, the aluminides and silicides contain sufficient amounts of aluminum and silicon to form, in oxidizing environments, oxide scales that are often compact and protective [5, 10, 11].

However, the aluminides and silicides, like other ordered intermetallics, generally exhibit brittle fracture and low ductility at ambient temperatures. Poor fracture resistance and fabricability have restricted the use of these intermetallics as engineering materials in most cases. Because of concentrated efforts, however, significant progress has been made in the understanding of the lack of ductility in these intermetallics, and both intrinsic and extrinsic factors governing their brittle fracture behavior have been identified. Perhaps the most significant recent development is the realization that an extrinsic factor, moisture-induced hydrogen embrittlement, is a major cause of poor ductility and brittle fracture in many aluminide and silicide alloys [1, 2, 5, 11]. The brittleness was explained in various ways, the main reasons being: a limited number of slip systems, impeded cross-slip, difficulty of strain transfer from one grain to another, formation of dislocation bar-

riers typical of ordered alloys, segregation of harmful impurities in grain boundaries [12, 13, 14]

Alloys based on the $Ti_3Al$ ($\alpha_2$) compound are currently experiencing limited use as advanced aerospace materials. To date, the alloys with the most desirable properties contain additions of $\beta$ stabilitizers, such as Nb, which promote the formation of the two-phase mixture of $\alpha_2 + \beta$ or $\alpha_2$ + B2 [14, 15, 16, 17, 18]. The ordering behavior of the $\beta$ phase is likely to influence the ductility of such alloys [19]. In particular, the two-phase $Ti_2AlNb$-based materials with second phase Nb have a good specific strength combined with an improved room temperature ductility and fracture toughness with respect to conventional titanium aluminides, without any loss of high-temperature strength [14, 20]. Therefore, the Ti-Al-Nb ternary system has assumed considerable significance in recent years [21, 22, 23]. The properties of the Ti-Al-Nb alloys depend to a large extent on type, number, amount, and form of the phases present. Unfortunately, the phase relationships in these systems have not been established in sufficient detail to allow their more widespread application [16].

In Japan and in the United States, the compound $Nb_3Al$ (A15) has been examined for its potential as a high-temperature structural material. The microstructure and mechanical behavior of single phase, binary $Nb_3Al$, two-phase $Nb_3Al$-Nb, and ternary $Nb_3AlX$ (X=Mo, Ta, Cr, Ti, Si, Sn, and Ge) have been examined. Titanium aluminide alloys based on TiAl offer potential benefits as intermetallics

for structural applications due to their low density and attractive properties at high temperatures. However, their strength and ductility are very dependent on microstructural morphologies, and much research is being devoted to obtaining optimal properties [24]. The large grain size and solute segregation associated with conventional castings have forced much of the work to be focused on obtaining finer microstructures, both in terms of grain sizes as well as lamellar spacings [25, 26, 27]. Thermomechanical treatments have been used to produce a large variety of structural morphologies ranging from fully lamellar ($\alpha_2 + \gamma$) to duplex and equiaxed and in which the proportion of each phase is also variable. The lamellar structures are beneficial for toughness and high-temperature strength; however, they have poor room-temperature ductility.

The recent approach for the development of intermetallic materials is essentially based on identifying binary intermetallic compounds, such as nickel, titanium and niobium aluminides as well as certain silicides, which exhibit some basic promising properties. However, these binary compounds generally suffer serious drawbacks, brittleness and lack of useful strength from an engineering standpoint. Moreover, the number of potentially interesting structural compounds is limited. Each of these binary compounds has a given crystal symmetry and, if it is complex, the compound is not deformable, and one does not expect much macroscopic ductility even at fairly high temperatures; in other words, the material has a ceramic-like behavior. If the crystal structure is simple or less complex, there are serious

prospects for ductilization and making the material workable [28].

Numerous attempts have been made in this direction, to make the crystal structure simple or less complex. Besides simplifying the crystal structure, grain size refinement or suppression of grain boundary movement also improves the ductility. In spite of some successful or even spectacular examples produced by such efforts, e.g., in $Ni_3Al$ and $Ti_3Al$, the materials science community has yet to provide a new processable material which possesses acceptable mechanical properties [28, 29].

The Nb-Ti-Al alloys have been classified within the spectrum of advanced intermetallic materials, but its disadvantage is its brittleness at room temperature. However, their lower density and higher temperature capability compared to present aerospace materials provide for a lighter weight component, with structural integrity, which would receive added protection from a suitable metallic coating [11, 30]. The Nb-Ti-Al alloys show attractive oxidation and oxygen embrittlement resistance compared to Ni-based alloys, as well as good tensile yield strength and ductility up to 1200°C. Results [11] reveal that strengthening for high-temperature service can be improved via appropriate additions of Cr, Hf and certain refractory elements.

Much work remains to be done to understand the fundamental aspects of the Ti-Al-Nb ternary system so as to provide data for microstructural control during processing. The precise transformation behavior and the influence of these phases on the alloy properties remain unclear. Although the density of Nb-rich alloys is

slightly higher than Ti-rich alloys, the melting points of Nb-rich alloys are much higher than Ti-rich alloys and potentially have improved mechanical properties [11, 20, 31]. Therefore, the purpose of this research is to examine the effect of heat treatment and microstructure on compressive strength from 600 to 1100°C of Nb-15%Al-10%Ti, -25%Ti and -40%Ti alloys. [Note all compositions are in atomic per cent.]

# CHAPTER II

# LITERATURE REVIEW

## 2.1 Phase Diagrams

The properties of a material depend to a large extent on the type, number, amount and form of the phases present. So it is essential to know the conditions under which these phases exist and the conditions under which changes in phases will occur. Phase diagrams are the most useful tools in understanding the effect of temperature and composition on the phase present in a material. Considering the importance of the ternary Ti-Al-Nb system, the three binary phase diagrams, Ti-Al, Al-Nb, and Ti-Nb are discussed first in the following sections.

### 2.1.1 Pure Niobium

Niobium is the 41st element in the periodic table. Also known as columbium, it has a higher melting temperature (2740 K (2467°C)) and lower density (8.55 g/cm$^3$ at 300 K (27°C)) than nickel (1726 K (1453°C) and 8.90 g/cm$^3$), which is the base material for the superalloys currently used in high temperature applications. Nb exhibits a body-centered cubic (bcc) crystal structural. It has been used for nuclear fuel element cladding as well as structural components due to its low neutron

capture cross section and its high strength at elevated temperatures. The Young's modulus of Nb decreases linearly with increasing temperature from a value of 111,700 MPa at room temperature to 97,200 MPa at 1093 K (820°C) [32].

Oxygen, carbon and hydrogen have a very high solubility in niobium. Nb reacts with oxygen of low partial pressure more effectively than many other metals [33, 34]. If handled in air, water or acids, the surface of Nb forms a layer of adsorbates and oxides. From the phase diagram of Nb-O system [35], one sees that oxygen has a solubility up to 1 at.%. The gaseous oxidation of single crystal Nb was observed and it was concluded that severe stress development within the oxide film played a dominant role in the break-away process of a protective oxide layer and that the critical thickness for crack nucleation varied with crystal orientation [20]. Progress in improving the oxidation resistance of Nb by such means as alloying or coating would be an important factor in determining its high-temperature applications.

### 2.1.2 Ti-Al Phase Diagram

Based on the available literature and thermodynamic modeling, Murray [36] has proposed a comprehensive binary Ti-Al phase diagram. Many difficulties are faced in the experimental determination of the phase diagram due to the strong effect of interstitial elements, such as oxygen and hydrogen on phase stability. The equilibrium phases in the Ti-Al system are: the disordered solution phases (liquid, hcp $\alpha$-Ti, bcc $\beta$-Ti, fcc Al) and the ordered intermetallic compounds, such as $\alpha_2$-$Ti_3Al$ with an ordered hexagonal close-packed structure, $\gamma$-TiAl and $TiAl_3$, both

of which have an ordered fcc structure [37]. The most recent Ti-Al phase diagrams are assessed by Kattner *et al.* [37] and Okamoto [38]. The diagram published by Okamoto is reproduced in Figure 2.1. The crystal structure data are given in Table 2.1.

### 2.1.3 Nb-Al Phase Diagram

The Nb-Al system has been extensively studied both experimentally [39, 40, 41, 42] and theoretically [43, 44] because of the outstanding superconductive properties of $Nb_3Al$. The Nb-Al system is a relatively simple system with six phases: liquid L; bcc Nb solid solution; $\delta$-$Nb_3Al$; $\sigma$-$Nb_2Al$; $\eta$-$NbAl_3$; and fcc Al solid solution with limited solubility of Nb. The $Nb_3Al$ phase is a superconducting compound with a transition temperature of 18.6 K. The assessed Nb-Al phase diagram is shown in Figure 2.2. The special points and crystal structure data are given in Table 2.2 [45]. Al has significant solubility in Nb, while the maximum solubility of Nb in Al is less than 0.3 at.%.

#### The Terminal Nb Solid Solution

The maximum solubility of Al in Nb occurs at 23.0 at.% Al at the first peritectic temperature of 2233 K (1960°C) [40]. A metastable extension of the Nb solid solution with the bcc (A2) structure containing up to 27 at.% Al was achieved by rapid cooling [46, 47] and up to 50 at.% Al by sputtering [48], mechanical alloying [49], electron beam evaporation [50] and thin film reaction [51].

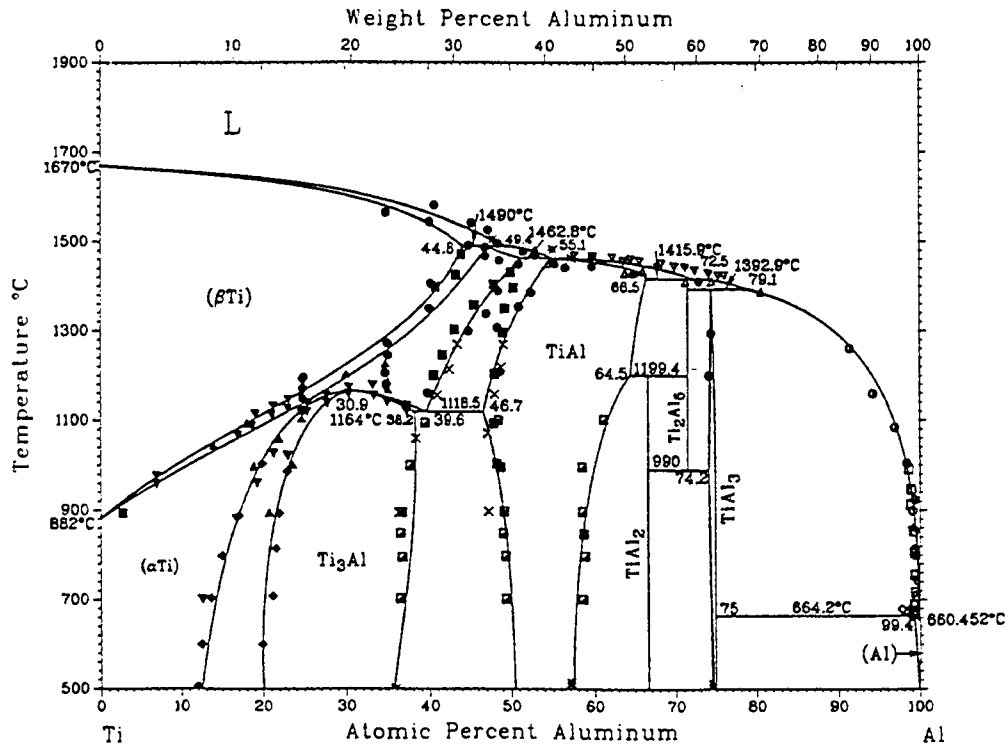



Figure 2.1: Ti-Al phase diagram.

Table 2.1: Ti-Al crystal structure data.

| Phase | Composition, atom percent Al | Pearson Symbol | Space Group | Strukturbericht Designation | Prototype |
|---|---|---|---|---|---|
| ($\beta$ Ti) | 0-44.8 | cI2 | Im3m | A2 | W |
| ($\alpha$ Ti) | 0-55.1 | hP2 | $P6_3/mmc$ | A3 | Mg |
| $Ti_3Al$ | 20-38.2 | hP8 | $P6_3/mmc$ | $DO_{19}$ | $Ni_3Sn$ |
| TiAl | 46.7-66.5 | tP4 | P4/mmm | $L1_0$ | AuCu |
| $TiAl_2$ | 66.7 | tI24 | $I4_1/amd$ | ... | ... |
| $Ti_2Al_5$ | 71.4 | ... | ... | ... | ... |
| $TiAl_3$ | 74.2-75 | tI8 | I4/mmm | $DO_{22}$ | $Al_3Ti$ |
| $\alpha$ $TiAl_3$ | 75 | t** | ... | ... | ... |
| (Al) | 99.4–100 | cF4 | Fm3m | Al | Cu |

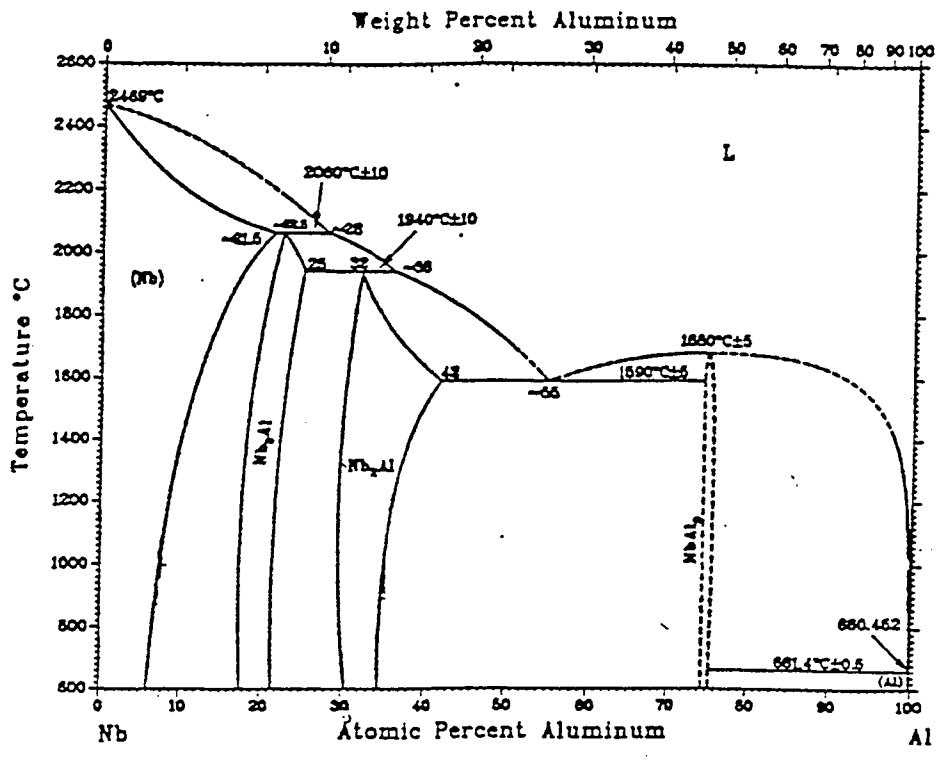



Figure 2.2: Nb-Al phase diagram.

Table 2.2: Nb-Al crystal structure data.

| Phase | Composition, atom percent Al | Pearson Symbol | Space Group | Strukturbericht Designation | Prototype |
|---|---|---|---|---|---|
| (Nb) | 0-21.5 | cI2 | Im3m | A2 | W |
| $Nb_3Al$ | 18.6-25 | cP8 | Pm3n | A15 | $Cr_3Si$ |
| $Nb_2Al$ | 30–42 | tP30 | $P4_2/mnm$ | $D8_b$ | $\sigma$ CrFe |
| $NbAl_3$ | 75 | tI8 | I4/mmm | $D0_{22}$ | $Al_3Ti$ |
| (Al) | 100 | cF4 | Fm3m | Al | Cu |

### The $Nb_3Al$ Phase

Lundin and Yamamoto [40] first reported that the A15 phase formed by a peritectic reaction ($Nb_{ss}$ + liquid $\longleftrightarrow$ A15). This mode of formation was later supported by observation of $Nb_{ss}$ + liquid $\longleftrightarrow$ $Nb_{0.775}Al_{0.225}$ at 2333 K (2060°C) [39]. A peritectoidal reaction: $Nb_{ss}$ + $Nb_2Al$ ($\sigma$ phase) $\longleftrightarrow$ A15, was also reported by Russian investigators.

The formation of $Nb_3Al$ from Nb solid solution was thought [40] to be a partial "massive transformation" to account for the observations of no composition change from one phase to the other and no bulk diffusion and the existence of a specific crystallographic relation involved.

### The $Nb_2Al$ and $NbAl_3$ Phases

Wood *et al.* [52] first reported the existence of the $\sigma$-$Nb_2Al$ phase which formed by a peritectic reaction: $Nb_3Al$ + liquid $\leftrightarrow$ $Nb_2Al$ reported at 2143 K (1870°C) by Jorda *et al.* [39] and 2213 K (1940°C) by Lundin *et al.* [40]. The maximum solubility of 41.3 at.% Al at 1823 K (1550°C) [39] and 1863 K (1590°C) [40] decreased to 32 at.% Al [39] and 30 at.% Al [40] aluminum at room temperature, while the Nb-rich solubility boundary changed slightly. The line compound $NbAl_3$ which formed by congruent melting at 1878 K (1605°C) [39] and 1953 K (1680°C) [40] had no detectable solubility range [39]. Diffusion coupling of solid aluminum and niobium showed that only $NbAl_3$ formed providing aluminum was present [53, 54].

### 2.1.4 Ti-Nb Phase Diagram

The equilibrium solid phases observed in the Ti-Nb system are: the bcc ($\beta$-Ti, Nb) solid solution with a complete range of solubility above 1155 K (882°C) , and the low temperature hcp $\alpha$-Ti solid solution with a maximum Nb solubility of 2.2 atomic percent at about 873 to 923 K (600 to 650°C) [36]. The $\beta \rightarrow \alpha$ transformation is sluggish and many metastable transformations are observed in this system during quenching. Phases of significance are the hcp $\alpha^{'}$-Ti form for low Nb contents and an orthorhombic distortion of the hcp form $\alpha^{''}$-Ti for higher Nb contents. In a broad range of alloys, hcp $\omega$ phase precipitates are observed during a slow quench from the $\beta$ field or during isothermal aging at temperatures below about 723 K (450°C). Figure 2.3 shows the assessed binary Ti-Nb phase diagram and crystal structure data are given in Table 2.3.

### 2.1.5 Ti-Al-Nb Phase Diagram

Niobium is a $\beta$-stabilizer [14, 15, 16, 17, 18, 55] in the Ti-Al system and sufficient additions of Nb help retain the high temperature $\beta$-phase which may undergo an ordering process upon cooling to give the B2 phase which has a CsCl structure. Techniques combining TEM and EDS showed that when dissolving in either TiAl ($L1_0$) or $Ti_3Al$ ($DO_{19}$) as a solid solution. Nb atoms preferentially occupied the Ti lattice sites [55]. Similar techniques applied to the Ti-24Al-11Nb (at.%) alloy showed that Nb atoms preferentially occupied Al sublattice sites in the ordered

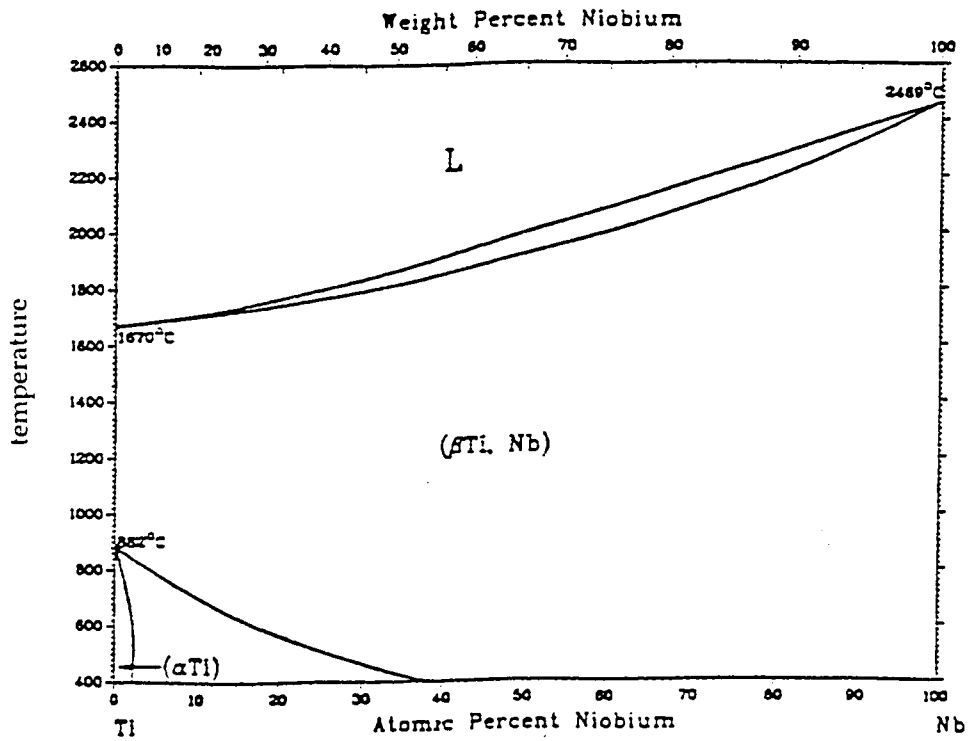



Figure 2.3: Ti-Nb phase diagram.

Table 2.3: Ti-Nb crystal structure data.

| Phase | Composition, atom percent Al | Pearson Symbol | Space Group | Strukturbericht Designation | Prototype |
|---|---|---|---|---|---|
| ($\alpha$ Ti) | 0–2.5 | hP2 | $P6_3/mmc$ | A3 | Mg |
| ($\alpha'$ Ti) | 0–5 | hP2 | $P6_3/mmc$ | A3 | Mg |
| ($\beta$ Ti, Nb) | 0–100 | cI2 | Im3m | A2 | W |
| ($\alpha''$ Ti) | 8–28 | oC4 | Cmcm | A20 | $\alpha$ U |
| $\omega$ | 9–30 | hP3 | P6/mmm | $\cdots$ | $\omega$ MnTi |

B2 phase [16, 19]. The lattice parameter of B2 phase in Ti-24Al-11Nb alloys was determined to be 3.24 Å [56], slightly greater than the value 3.22 Å of the disordered bcc solid solution.

The order-disorder transition temperature of the B2 phase was found to depend on the Nb concentration [16, 56, 57]. An evaluation of the structure factors of superlattice reflections in the B2 phase as a function of site occupancies [57] suggested that the {100} superlattice reflection intensity could be very low for certain compositions. Therefore, at low annealing temperature the alloys might still be ordered but have site occupancies different from alloys annealed at high temperatures.

Perepezko *et al.* [22] carried out a comprehensive study on phase relations in Ti-Al-Nb alloys at 1473 K (1200°C) and developed the ternary phase diagram as shown in Figure 2.4. Partial ternary isotherms of the Ti-Al-Nb system are available between 973 K (700°C) and 1673 (1400°C) [21, 30, 37, 58, 59, 60, 61]. Much of the phase stability studies are concentrated on the $Ti_3Al$-Nb alloys due to their practical significance. The solubility of niobium in $Ti_3Al$ at low temperature is considered to be 12 atomic percent. Recent studies showed that Ti-25Al-25Nb alloys contain an orthorhombic phase, *o*, belonging to Cmcm space group and these alloys exhibited better mechanical properties compared to the $\alpha_2$-based alloys [19, 62, 63, 64]. The effect of niobium addition on the transformation temperature of the *o* phase is unknown. Muraleedharan *et al.* [65] have estimated the transformation

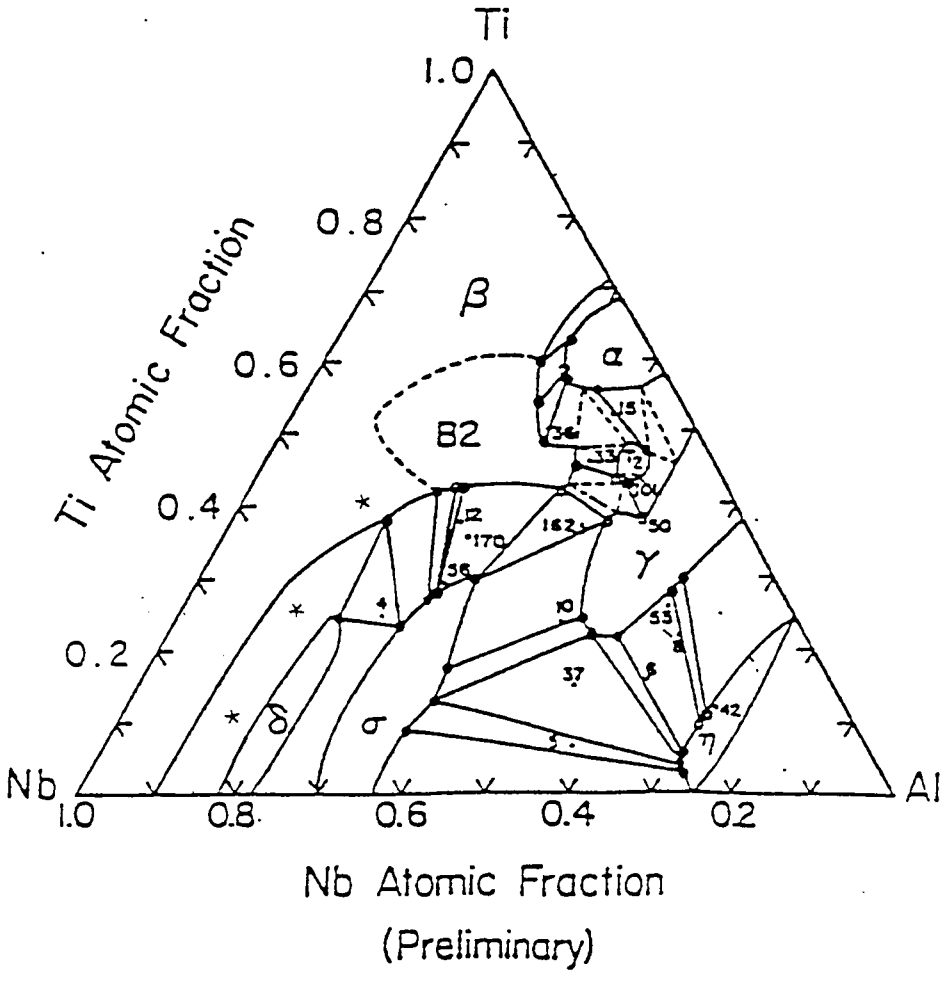



Figure 2.4: Ti-Al-Nb phase diagram at 1473 K (1200°C). Note $\star$ locates the investigated alloys.

temperature to be 1253 K (980°C) for Ti-24Al-15Nb composition and the same temperature is predicted by Bendersky *et al.* [66] for Ti-25Al-25Nb composition. $\omega$ and its related phases are observed in alloys containing the B2 phase when cooled to room temperature from elevated temperatures [67, 68].

The existence of aluminides such as $Ti_2AlMo$ and $Ti_2AlCr$ has been reported in the literature only with some ternary B2 compounds. Very recently, it has been recognized [28] that the B2 phase exists in the ternary Ti-Al-Nb system around the composition $Ti_{50}Al_{25}Nb_{25}$ (=$Ti_2AlNb$). It is interesting to note that the compositions of the $Ti_2AlX$ (X=Mo, Cr, Nb) phase are located on the tie-line $Ti_3Al$-$AlX_3$; therefore, $Ti_2AlX$ can be obtained from $Ti_3Al$ by substituting X for 25% of Ti.

## 2.2 The Ti-Al Intermetallics

### 2.2.1 The TiAl Alloys

Materials based on the TiAl intermetallic $\gamma$ phase, compared with $Ti_3Al$ alloys, have a higher elastic modulus, lower density, and better high temperature capability [1], but their room temperature ductility and fracture resistance are poor.

The $\gamma$ phase of the TiAl system has an ordered face-centered tetragonal, $L1_0$ structure composed of alternating {001} planes of Ti and Al atoms. Deformation occurs by slip on {111} planes. Initial attempts to improve ductility of single-phase $\gamma$ titanium aluminide through alloy additions of V, Nb, and W proved unsuccessful.

Research on $\gamma$ phase alloys focused on attempts to increase room temperature ductility and toughness in two-phase alloys via compositional modifications. It was found that additions of Mn and V improved ductility, while Nb and Ta improved strength. It appears that there has been marginal success in improving the room temperature tensile properties of the $\gamma + \alpha_2$ alloys, with some improvements in strength particularly at high temperature.

The $\gamma$ alloys are attractive because they offer excellent high-temperature environmental resistance and good stiffness and density, combined with excellent creep resistance. To date most of the alloys in this class have had low tensile ductilities (<1%) up to temperatures of 750°C [1]. There appear to be no solutions for improving $\gamma$ alloys.

### 2.2.2 The $Ti_3Al$ Alloys

The $\alpha_2$ ($Ti_3Al$) phase in the Ti-Al binary system is an intermetallic compound having an ordered hexagonal ($DO_{19}$) structure. Two-phase alloys based on this compound have, in comparison to conventional $\alpha + \beta$ titanium alloys, greater strengths at elevated temperatures, higher elastic moduli, and greater resistance to oxidation. However, the ordered structure that allows for the higher temperature capability of these alloys also results in restricted dislocation slip at lower temperatures, resulting in limited ductilities, fracture toughnesses, and impact resistance [1].

The brittleness exhibited by this compound in bulk polycrystalline form at low

temperatures was found to be attributable to a lack of an adequate number of independent slip systems. It was found [1] that niobium increases the number of active slip systems. However, because slip is still planar, only limited general deformation is accomplished prior to fracture. In addition, the aluminum level plays a large role in mechanical properties, as does the amount and identity of the $\beta$ stabilizers added. Good elevated-temperature strength, creep resistance, and environmental resistance are favored by a high aluminum content, a moderately high $\beta$ stabilizer content, and the avoidance of the use of vanadium as an alloying addition. Good room-temperature ductility and fracture toughness are enhanced by low aluminum content, low oxygen content, and a high $\beta$ stabilizer content that favors the use of niobium over molybdenum. The goal of these alloy development programs has been to achieve the good elevated-temperature properties (creep, environmental resistance, microstructure stability) needed for structural service, while having adequate low temperature properties (ductility, fracture toughness, impact resistance) and good tensile strength, fatigue strength, and crack growth resistance at all temperatures. It has proven impossible to date to achieve an alloy processing and microstructure combination which meets all of these goals simultaneously. In general, it is difficult to overcome the room-temperature low ductility; hence, their application has been limited.

## 2.3 Microstructures of the Ti-Al-Nb Intermetallics

The microstructures of Nb-Al-Ti alloys can be complex, depending on the alloy and the heat treatment. Since the research deals with Nb-rich alloys, only those phases of interest to the research will be reviewed here. At 1473 K (1200°C), these will be $\beta$, B2, $\delta$, and perhaps other phases in the vicinity of these (Figure 2.4). At lower temperatures, others will be of interest. The phases and microconstituents that are reviewed here are tabulated in Table 2.4, along with some of their characteristics.

### 2.3.1 The A15 ($\delta$) Phase

$Nb_3Al$ ($\delta$) crystallizes in a cubic structure of point group $m\bar{3}m$, space group $Pm\bar{3}n$. This structure is adopted by $\beta$-W and is denoted as the A15 structure in the Strukturbericht notation. The schematic of A15 structure is drawn in Figure 2.5. There are 48 general equivalent positions in the A15 structure; atoms are in special positions, Nb in 6c, Al in 2a. The A15 compounds generally do not exhibit plastic deformation, and are extremely brittle at temperature below 1475 K (1202°C) [17], while they can be ductile at high homologous temperature [69, 70] or under high hydrostatic pressure at room temperature [71]. Because the shortest complete lattice vector in this structure is <100>, dislocations with **b**=<100> presumably possess the lowest self-energy [72]. The fact that <100>{010} yield only three independent slip systems [73] in A15 structure, but at least five independent slip

Table 2.4: The phases and notations of Ti-Al-Nb alloys.

| Phase | Notation | Cell Structure | Space Group |
|---|---|---|---|
| $\alpha$Ti | $\alpha$ | hcp (A3) | $P6_3/mmc$ |
| ($\beta$Ti,Nb) | $\beta$ | disordered bcc (A2) | Im3m |
| TiAl | $\gamma$ | ordered fcc ($L1_0$) | P4/mmm |
| $Nb_2Al$ | $\sigma$ | ($D8_b$) | $P4_2/mnm$ |
| $Nb_3Al$ | $\delta$ | (A15) | Pm3n |
| $(Ti,Nb)Al_3$ | $\eta$ | ($D0_{22}$) | I4/mmm |
| $Ti_3Al$ | $\alpha_2$ | ordered hcp ($D0_{19}$) | $P6_3/mmc$ |
| | B2 | ordered bcc (B2) | $Pm\bar{3}m$ |
| | T | ordered bct | |
| $Ti_2AlNb$ | $o$ | orthorhombic | Cmcm |
| $Ti_4Al_3Nb$ | $\omega$ | ordered hcp ($B8_2$) | $P6_3/mmc$ |

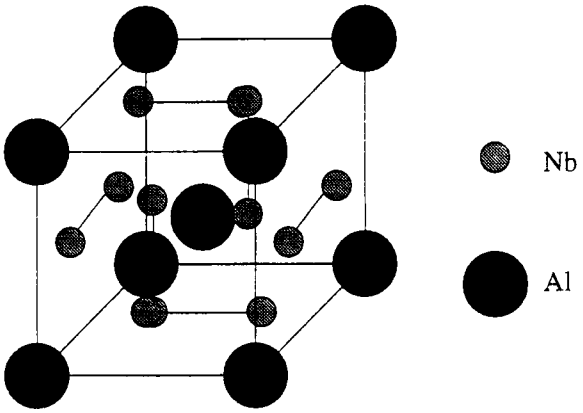



Figure 2.5: The schematic structure diagram of A15 unit cell.

systems are necessary to be ductile [74, 75], explains why a general plastic deformation is not possible at room temperature.

### 2.3.2 The A2 ($\beta$) Phase

Nb, $\beta$-Ti and ($\beta$-Ti, Nb) have a cubic structure of point group Im3m. This structure is adopted by W and is denoted the A2 structure in the Strukturbericht notation. The A2 ($\beta$) structure is body-centered cubic which may undergo an ordering process upon cooling to give the B2 phase.

### 2.3.3 The B2 Phase

Compounds of B2 structure are found in many alloy systems. The B2 crystal structure, shown in Figure 2.6, is also referred to as ordered body-centered cubic. which can be thought of as consisting of two interpenetrating simple cubic sublattices.

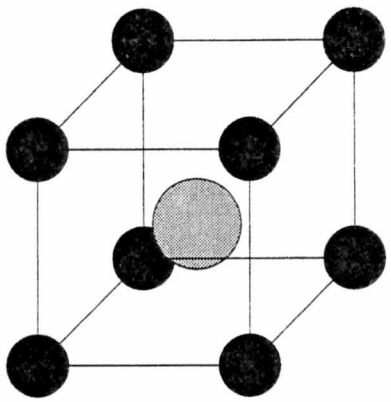


Figure 2.6: The schematic structure diagram of B2 unit cell.

A wide variety of transformation behavior in the high temperature $\beta$ phase can be produced through varying composition, cooling rates and heat treatment. The occurance of B2 ordering over a wide composition in Nb-rich alloys is observed during quenching from the $\beta$ phase field [17, 76, 77]. The $\omega$ phase also forms along with the B2 phase during quenching [17]. There is a tweed microstructure in the quenched Ti-Al-Nb alloys [77]. Dislocations of three types of Burgers vectors, namely <100>, <110> and <111>, have been observed in alloys with B2 structure [20, 78]. Several models [79, 80, 81] were developed to rationalize the factors that determine the type of operative dislocations.

A hard-sphere model [80] was proposed in which criteria controlling slip in B2 compounds were thought to be atom size ratio, type of binding and crystal orientation. Analysis of the hard sphere model indicated that slip systems {321}<111>, {211}<111> and {110}<111>, as seen in bcc materials, as well as {110}<110>,

{110}<100> and {100}<100>, are highly probable slip systems in B2 compounds. Other rationalizations for preferred operative slip systems in terms of the dislocation mobility and self-energy were also suggested [81]. It is not clear that any of the models can explain the observed slip systems in all the B2 compounds.

### 2.3.4 The $\omega$ Phase

Diffraction effects [77] clearly stand out as the $\omega$ forms. These include the strong <110> streaking in the <110>$\beta$ zone and extra maxima at $\frac{1}{2}$<110> positions in various zones such as <100> and <113>. Extinction of the streaks and strations observed under different diffracting conditions in the electron microscope are consistent with {110}<1$\bar{1}$0> shear strains. The $\frac{1}{2}$<110> satellite reflections appear related to the intense streaking in that both effects are always observed to occur concurrently and because the reflections commonly occur at streak intersections or along the streak.

### 2.3.5 Ti-Rich Aged Alloys

Peters *et al.* [82] constructed a time-temperature transformation (TTT) diagram for Ti-25Al-10Nb-3V-1Mo (at.%) alloy, from dilatometry data. At high isothermal transformation temperature (> 1153 K (880°C)) the $\alpha_2$ and B2 phases were dominant. In the temperature range 873-1073 K (600-800°C), the $\alpha_2$ and/or $o$ phases are formed. At temperatures between 573 and 823 K (300 and 550°C), a complex mixture of $\omega$, $o$ and $\alpha_2$ was found.

Hsiung *et al.* [83] constructed a Ti-24Al-11Nb alloy TTT diagram. The phase transition sequences that took place during isothermal aging of the quenched Ti-24Al-11Nb alloy depended upon the temperature range. For T < 923 K (650°C), both $\beta$/B2 $\rightarrow \omega$ and $\beta$/B2 $\rightarrow \alpha_2$ took place. For 923 K < T < 1173 K (650°C < T < 900°C), $\beta$/B2 $\rightarrow \alpha_2$ was prevalent. A complex reaction sequence was found for $\beta$/B2 transition: $\beta$/B2 $\rightarrow$ T (ordered bct) $\rightarrow o \rightarrow \alpha_2$. For 1173 K < T < 1423 K (900°C < T < 1150°C), a decomposition reaction $\beta \rightarrow \alpha_2$ (Nb-lean) + $\beta$ (Nb-rich) took place.

The continuous cooling transformation (CCT) of Ti-24Al-11Nb (at.%) alloys has been proposed by Weykamp *et al.* [84]. At even the most rapid rates the $\beta$ undergoes an ordering reaction to form the B2 structure. With decreasing cooling rate, the $\beta$ phase is observed to decompose into different phases.

During isothermal aging at temperatures below about 723 K (450°C), or during a slow quench from the $\beta$ field, the $\omega$ phase precipitates. The $\omega$ phase is a hexagonal close-packed structure of point group $P6_3/mmc$ [62, 63, 64].

The ordered orthorhombic phase $o$, which belongs to Cmcm space group, was observed in Ti-Al-Nb alloys [62, 63, 64]. The $o$ phase has been found upon slowly cooling from the temperature regime above 1473 K (1200°C), the $\beta$ stable regime, and after quenching from that temperature regime followed by isothermal aging. The $o$ phase is metastable; $o \rightarrow \alpha_2$ transition took place when the $o$ phase was further aged.

Bendersky *et al.* [68] found when a Ti-30Al-20Nb (at.%) alloy was annealed at 973-1173 K (700-900°C) for up to 18 days, the structure consisted of two intermetallic phases, $o$ and $\omega$. The identity of the two phases in the microstructure is independent of heat treatment path. Thus, the two phases appear to be in thermodynamic equilibrium between 973 and 1173 K (700 and 900°C). The distribution of the $o$ and $\omega$ phases in the alloy can be controlled either by changes in cooling rate or by temperature at which the quenched material is equilibrated.

## 2.4 Mechanical Properties of the Ti-Al-Nb Intermetallics

### 2.4.1 Tensile Behavior of Ti-Rich Alloys

The properties of $Ti_3Al$-Nb alloys are strongly affected by microstructure, which depends on the thermomechanical treatment. For example, the tensile strength of heat treated Ti-24Al-11Nb is strongly affected by acicular lath spacing. Fine lath spacing leads to an increase in strength. Increased cooling rates produce finer acicular microstructure and hence higher strengths [57], but this reduces the ductility at highest cooling rate, which is attributed to an increase in retained B2 phase.

Balsone [8] and Larsen *et al.* [1] indicated that interstitial oxygen is also observed to play a significant role on strength and ductility levels. There is an inverse relation between yield strength and ductility for the transformed $\beta$ structures. A ductility maximum is observed at 573 to 773 K (300 to 500°C) in some of the

low oxygen $\beta$ solutionized materials. Fractographic studies on the tensile samples tested in air and vacuum show that the decrease in ductility at high temperature is due to environmental degradation as well as $\beta$ decomposition. Increasing the Al level and the amount of $\beta$ stabilizers both result in increased yield strength.

### 2.4.2 Fracture Toughness of Ti-Rich Alloys

Fracture toughness appears to depend more on alloy composition than on microstructure. Nb increases the toughness by increasing the volume fraction of the $\beta$ phase, and Mo reduces toughness and ductility. Fracture toughness increases with temperature but appears to be independent of yield strength and tensile ductility. $Ti_3Al$-Nb alloys have competitive specific rupture strength [85]. Ti-24Al-11Nb has a fracture toughness which is less than half that of engineering alloys, such as Ti-6242S and the iron-base alloy 17-7 PH. Alloys with additional $\beta$ phase stabilizing elements, such as in Ti-25Al-10Nb-3V-1Mo, have improved elevated-temperature properties, but at a loss in fracture toughness. The fracture toughness of Ti-25Al-10Nb-3V-1Mo is comparable to that of the TiAl-based alloy Ti-48Al-1V-0.1C. Though Ti-24Al-11Nb is the toughest, its strength is poor. Although alloying improved the elevated-temperature impact resistance, the impact resistance is below that of the conventional materials, which is a cause of concern for applications, such as turbine engine compressor blades.

### 2.4.3 Fatigue Properties of Ti-Rich Alloys

Fracture mechanics and crack propagation are very important factors in the design of airframes and turbine engines. Fatigue crack propagation rate depends on numerous variables, such as temperature, stress ratio, frequency, environment, thermal-mechanical cycling and load-temperature spectrum. Fatigue properties are also affected by microstructure. High ductility alloys and fine and equiaxed grain microstructure, perform the best under low-cycle fatigue condition [86], while high-cycle fatigue strength appears to strongly depend on material's strength. In general, alloying effects seem to be the major factor rather than the microstructure.

### 2.4.4 Creep Behavior of Ti-Rich Alloys

Increasing the $\beta$ stabilizer content results in improved creep resistance in Ti-Al-Nb-Mo alloys [1, 8]. The results also show that fine grain microstructure has much higher creep resistance than coarse grain microstructure. The quench rate is another factor which affects the creep behavior. A lower steady-state creep rate was observed for the lower quench rate, while higher cooling rates increased the steady-state creep rate. Both Si and Zr additions appear to improve the creep resistance [87].

### 2.4.5 Compressive and Tensile Behavior of Nb-Rich Alloys

The compressive yield strength of the heat-treated, 1373 K (1100°C) for 50 h, Nb-15Al-10Ti alloy is higher than that of the IN718 alloy when the temperature is below 1173 K (900°C), and the Nb-rich alloy is less dense than the superalloy [20]. Shyue *et al.* [20] pointed out that the Nb-rich alloys exhibit good strength in compression over a wide temperature range; the yield strength varies from 1150 MPa at room temperature to 620 MPa at 1173 K (900°C).

They also showed that the Nb-15Al-40Ti alloys are inherently ductile at room temperature, with approximately 20% elongation prior to tensile failure. Both Nb-15Al-10Ti and Nb-15Al-40Ti alloys exhibit <111>{110}, <111>{112} and <111>{123} slip systems.

### 2.4.6 Pesudo-twinning in Nb-Rich Alloys

Yang *et al.* [76] indicated that the pesudo-twinning occurs when Nb-rich alloys are deformed. The mechanism causes a phase transformation from the B2 to an ordered orthorhombic structure. Mechanical twinning is observed in most bcc transition metals when they are deformed at low temperature and/or high strain rates. As the twinning shear results in the formation of a new phase, strictly speaking this process is not twinning but resembles the formation of stress-induced martensite, here refered to as pesudo-twinning.

A plate-like microstructure is commonly observed and found widely distributed

in the deformed Nb-15Al-25Ti alloy. The plate-like microstructure is a result of deformation twinning, with twinning plane $(\bar{1}1\bar{2})$.

### 2.4.7 Strain Aging in Nb-Rich Alloys

Wheeler *et al.* [88] observed strain aging phenomena. The dynamic strain aging is illustrated by serrated flow and negative strain rate sensitivity at intermediate temperature, 673 to 873 K (400 to 600°C). Deformation occurs in <111>{110} system, where large strains are accommodated in slip bands rather than by homogeneously distributed slip. The $o$ phase is formed and such precipitation is proposed to affect dislocation motion to account for the serrated yielding observed.

They also indicated that the cause of such serrated behavior has been attributed to the presence of a fine dispersion of the $\omega$ phase, and its re-precipitation following cutting by dislocations to give rise to the dynamic effects observed. It has been shown that deformation at intermediate temperature is indeed accompanied by yield point phenomena and serrated yielding, both consistent with a Portevin-Le Châtelier (PLC) effect. The dispersion of particles formed at temperatures around 773 K (500°C) are most probably the $o$ phase, or mixtures of both the $o$ and $\omega$ phases, where locking of dislocations seems to be more efficiently provided by the $o$ phase particles.

# CHAPTER III

# EXPERIMENTAL PROCEDURES

## 3.1 Materials Preparation

The nominal composition of the research alloys are Nb-15Al-10Ti, Nb-15Al-25Ti and Nb-15Al-40Ti, all in atomic per cent, designated as 10Ti, 25Ti and 40Ti, respectively. There are two groups of materials for this study. Group I was supplied by the Naval Air Development Center, and were prepared by transferred arc plasma melting in an argon atmosphere on a water-cooled hearth. The 40Ti alloy of Group II was prepared at Oak Ridge National Laboratory by arc-melting. This casting was then hot rolled from a round bar 25 mm in diameter to a plate 10 mm thick. Attempts to hot roll castings of 10Ti and 25Ti made by the method met with disaster; extensive cracking and shattering occurred. Thus the samples for these two compositions were fabricated by arc-melting and re-melting at least six times to promote homogeneity, then followed by rapid cooling to room temperature on a water-cooled copper hearth after the final melting. When referring to the 40Ti alloy of Group II it must be kept in mind that this material was initially in the hot rolled condition. The chemical compositions of the group II alloys are listed in Table 3.1. The chemical analysis of the group I alloys was not available due to

the limited amount of the materials.

## 3.2 Heat Treatments

Compression tests were conducted on group I alloys in as-cast condition. while group II alloys were first heat-treated at 873, 1173 and 1373 K (600, 900 and 1100°C) for either 10 or 100 hours, then compression tests conducted. The heat treatments given to the group II alloys are listed in Table 3.2. The samples were placed in quartz tubes, evacuated then back-filled with purified argon. At the end of the heat treatments they were quenched by breaking the quartz tube in water.

The dimensions of the group I alloys were 3 mm x 3 mm x 7 mm, while group II alloys were 5 mm x 5 mm x 15 mm. The specimens were cut by using either a low speed diamond saw or a high speed cutting wheel, and then ground through 4/0 paper.

## 3.3 Compression Test

Compression tests were conducted using a Material Test System machine equipped with furnace and vacuum system. The test conditions were different for group I and group II alloys.

For group I alloys, the specimens were tested at strain rates of approximately $5x10^{-2}$, $10^{-4}$ and $10^{-5}$ $s^{-1}$. The test was stopped at a total strain of approximately

Table 3.1: Chemical compositions of group II alloys.

| alloys | Nb | Al | Ti | C | S | N | O |
|---|---|---|---|---|---|---|---|
| Nb-15Al-10Ti | 74.99 | 14.17 | 10.75 | 0.052 | <0.002 | <0.006 | 0.024 |
| Nb-15Al-25Ti | 58.27 | 14.65 | 26.98 | 0.059 | <0.002 | 0.010 | 0.026 |
| Nb-15Al-40Ti | 43.72 | 13.59 | 42.57 | 0.096 | 0.002 | 0.009 | 0.016 |

note: all in atomic per cent

Table 3.2: Heat treatment conditions.

| temperature (°C) | holding time (hrs) | cooling method |
|---|---|---|
| 600 | 10 and 100 | water quench |
| 900 | 10 and 100 | water quench |
| 1100 | 10 | water quench |

5%. The experiments were conducted in an argon environment at 673, 873 and 1173 K (400, 600 and 900°C), and in air at room temperature.

For group II alloys, the specimens were deformed by compression at a strain rate of $10^{-4}$ $s^{-1}$, and tested to a strain of 5%. All the tests were conducted in an argon environment at 1173 K (900°C).

The stress-strain curves were obtained from the raw data, which were recorded by the personal computer, by using a graphic software package. The yield strengths were determined with 0.2% offset according to ASTM-E6.

## 3.4 Optical Microscopy

Preliminary microstructural observations were made by optical microscopy (OM). After testing, a small piece was cut from each sample, and the cut face was metallographically prepared by standard polishing methods. The surface was etched in a solution of 6 ml of nitric acid ($HNO_3$), 3 ml of hydrofluoric acid (HF) and 100 ml distilled water ($H_2O$) at 25°C for about 5 minutes to obtain optimum metallographic contrast.

## 3.5 Scanning Electron Microscopy

Scanning electron microscopy (SEM) was performed in a Cambridge Steroscan 360 equipped with an Energy Dispersive Spectrometer (EDS) with the same spec-

imens as those used for optical microscopy. Enhanced atomic number contrast to differentiate phases was obtained by imaging with back-scattered electrons.

## 3.6 Transmission Electron Microscopy

Transmission electron microscopy (TEM), conducted using a Philips CM12, was used for all the detailed microstructure observations as well as crystallographic analysis by Convergent Beam Electron Diffraction (CBED) techniques [89].

The specimens were prepared for transmission electron microscopy by sectioning, perpendicular to the compression test direction, the tested specimens into 0.5 mm thick slices. The slices were then hand ground to 3 mm discs and a thickness of about 150 $\mu$m. The 3 mm discs were electrochemically polished by a twin-jet polisher, using a solution of 10 vol.% sulfuric acid ($H_2SO_4$) in methanol ($CH_3OH$) at 233 K ($-40°C$) and a current of 100 mA. The thin foils were immediately cleaned with methanol many times and dipped into hydrofluoric acid (HF) for 10 seconds, and then cleaned with methanol to avoid contamination on the surface of the thin foil.

# CHAPTER IV

# RESULTS AND DISCUSSION

## 4.1 Stress-Strain Behavior of Group I Alloys

The stress-strain curves for the three as-cast alloys of 10Ti, 25Ti and 40Ti are presented in Figures 4.1-4.3. The shapes of these curves can be divided into three groups: (i) normal stress-strain curves, which do not exhibit a yield drop behavior (e.g., Fig. 4.2, 298 K (25°C), $10^{-5}$ $s^{-1}$), (ii) serrated stress-strain curves manifesting the periodic yielding phenomenon (e.g., Fig. 4.2, 873 K (600°C), $10^{-4}$ $s^{-1}$ and Fig. 4.3, 40Ti alloy at 873 K (600°C) and $10^{-4}$ $s^{-1}$) and (iii) stress-strain curves indicating yield drop behavior, i.e., an initial increase in the strength followed by a decrease in strength (e.g., Fig. 4.3, 1173 K (900°C), $10^{-4}$ $s^{-1}$).

In Figure 4.1, the stress-strain curves of the 10Ti alloy at 673 K (400°C) and strain rates of $5x10^{-2}$, $10^{-4}$ and $10^{-5}$ $s^{-1}$, and at 1173 K (900°C) and the high strain rate of $5x10^{-2}$ $s^{-1}$, exhibit the group (i) behavior. The stress-strain curves at 1173 K (900°C) and the lower strain rates of $10^{-4}$ and $10^{-5}$ $s^{-1}$ belong to group (iii). In Figure 4.2, the stress-strain curves of the 25Ti alloy at 298 K (25°C) and all strain rates, at 873 K (600°C) and the strain rate of $5x10^{-2}$ $s^{-1}$, as well as at 1173 K (900°C) and the strain rate of $5x10^{-2}$ $s^{-1}$, show the group (i) characteristics. The

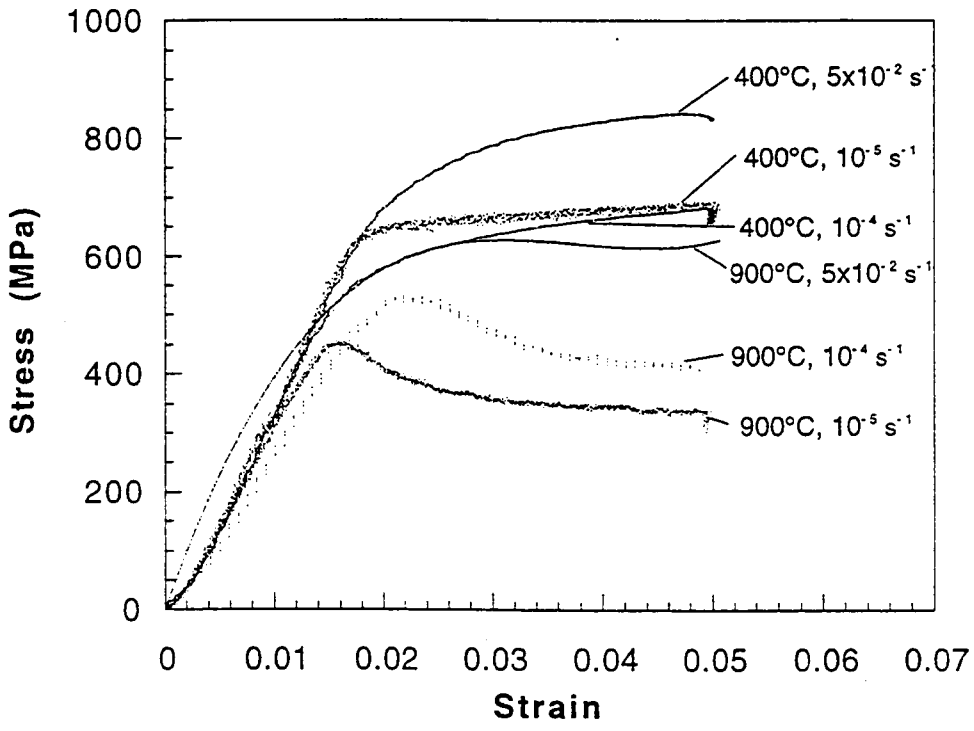



Figure 4.1: Compressive stress versus strain curves of Nb-15Al-10Ti alloys.

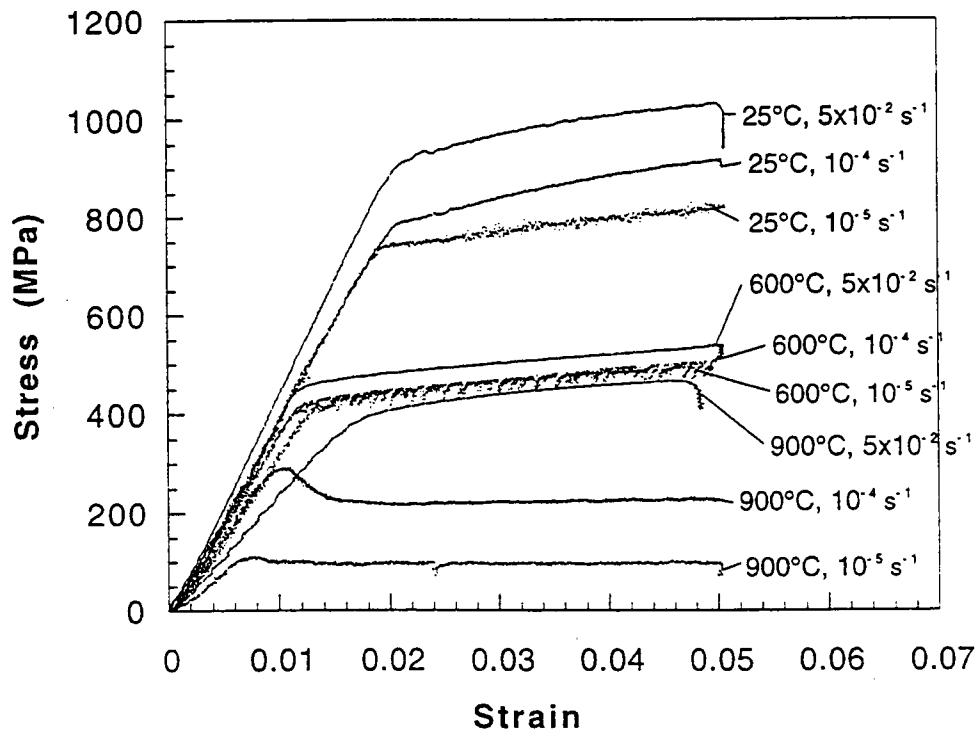



Figure 4.2: Compressive stress versus strain curves of Nb-15Al-25Ti alloys.

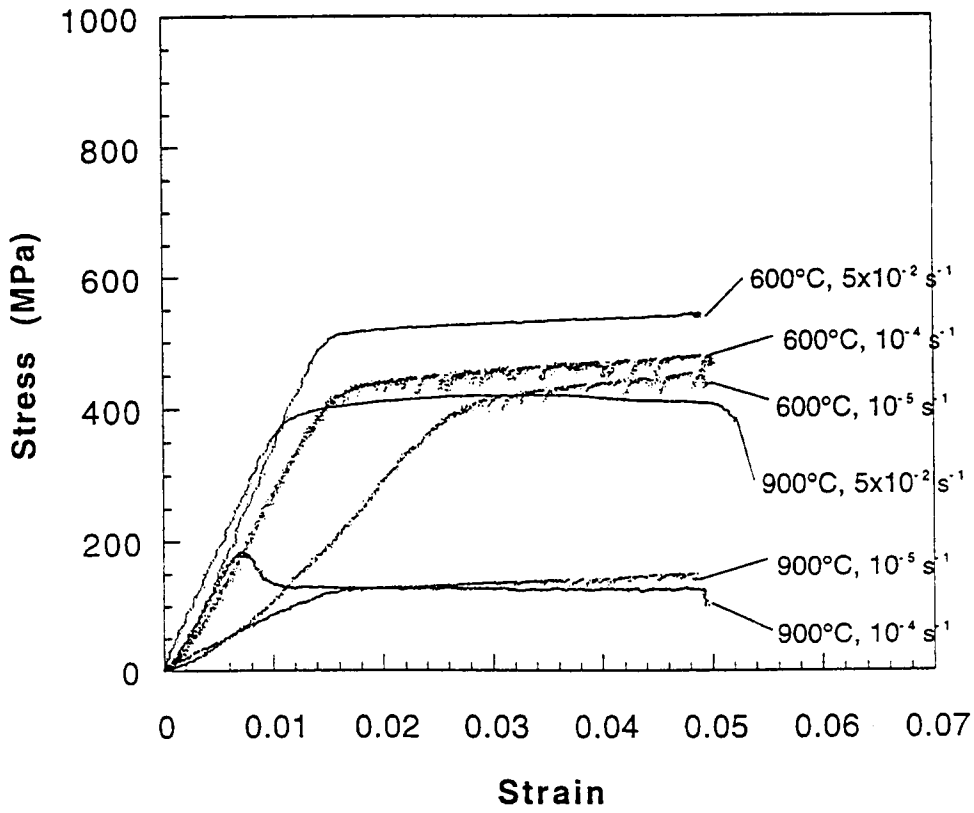



Figure 4.3: Compressive stress versus strain curves of Nb-15Al-40Ti alloys.

stress-strain curves at 873 K (600°C) and the strain rates of $10^{-4}$ and $10^{-5}$ $s^{-1}$ belong to group (ii). The stress-strain curves at 1173 K (900°C) and the strain rates of $10^{-4}$ and $10^{-5}$ $s^{-1}$ exhibit the group (iii) behavior. In Figure 4.3, the stress-strain curves of the 40Ti alloy at 873 K (600°C) and the strain rate of $5x10^{-2}$ $s^{-1}$, as well as at 1173 K (900°C) and the strain rates of $5x10^{-2}$ and $10^{-5}$ $s^{-1}$, belong to group (i). The stress-strain curves at 873 K (600°C) and the strain rates of $10^{-4}$ and $10^{-5}$ $s^{-1}$ show the group (ii) characteristics. The stress-strain curve at 1173 K (900°C) and the strain rate of $10^{-4}$ $s^{-1}$ belongs to group (iii).

As a summary for the three alloys investigated, the stress-strain curves at the lower temperatures of 298 and 673 K (25 and 400°C) and all strain rates exhibit the normal behavior without the presence of serrations or yield drop. The stress-strain curves at 873 and 1173 K (600 and 900°C) and the high strain rate of $5x10^{-2}$ $s^{-1}$ show the same behavior. At 873 K (600°C) and the lower strain rates of $10^{-4}$ and $10^{-5}$ $s^{-1}$, serrated stress-strain curves were observed. At the highest temperature of 1173 K (900°C) and lower strain rates of $10^{-4}$ and $10^{-5}$ $s^{-1}$, yield drop was typically observed. Note that for the 40Ti alloy, the yield drop behavior was not observed at 1173 K (900°C) and a strain rate of $10^{-5}$ $s^{-1}$.

## 4.2 Serrated Stress-Strain Curves of Group I Alloys

The serrated stress-strain behavior was observed at 873 K (600°C) and the low strain rates of $10^{-4}$ and $10^{-5}$ $s^{-1}$. The serrations in the stress-strain curves can be attributed to the strain aging phenomenon [90]. Many intermetallic compounds which exhibit low ductility show the stress-strain behavior reminiscent of the more brittle b.c.c. refractory metal. When tested in the as-cast state, where the initial mobile dislocation density is quite low, numerous intermetallic compounds show very low ductilities. Such behavior is indicative of a difficulty in dislocation generation rather than inherent lack of dislocation mobility [91]. It has long been known that the yield drop and inhomogeneous deformation can be suppressed by a mild, warm working treatment to provide a fresh pool of mobile dislocations. The population of mobile dislocations can also be affected by strong interactions between interstitial solute atoms and the highly strained region at the core of a dislocation [78]. Decoration of the core region with interstitial solutes renders the dislocations immobile, thus reducing the mobile dislocation density. The subsequent embrittlement is referred to as strain aging embrittlement.

Serrations have been observed in stress-strain curves at intermediate temperatures and related to dynamic interactions between mobile dislocations and solute atoms. It appears only at intermediate, not at high or low temperatures, because of the following reasons. At high temperatures the diffusivity of the solute atoms is high enough that the solute atoms and the dislocations move together, thereby

requiring no break-away of the dislocations [91]. At low temperatures, the diffusivity of the solute atoms is so low that no dynamic interaction can occur. Thus, the entire range of yielding phenomena can be consistently explained in terms of interactions between solute atoms.

The serration begins with the onset of localized plastic deformation, typical of solute drag interactions between the dislocations and interstitial solutes. Following the initial serration, the solutes can diffuse to the dislocations again, which yields repeated serration during further straining. This process is repeated during straining, thus resulting in periodic yielding throughout the whole stress-strain curve. The periodic flow stress (serrated yielding) behavior is usually observed during deformation at low strain rates and high temperatures [91], which is consistent with the present investigation, as shown in Figure 4.4.

## 4.3 Yield Drop Behavior

In general, the yield drop phenomenon as found in these alloys is due to either superplasticity [92, 93, 94, 95, 96, 97, 98, 99] or dynamic recrystallization [100, 101, 102, 103, 104]. The requirements for superplasticity are: a fine equiaxed and stable grain structure (10 microns or less), a high strain rate sensitivity, generally low strain rates ($< 10^{-2}$ $s^{-1}$), and a processing temperature of at least 0.5 times the absolute melting temperature. Other factors, including grain aspect ratio, grain size distribution, texture, and volume fractions of phases and their deformation

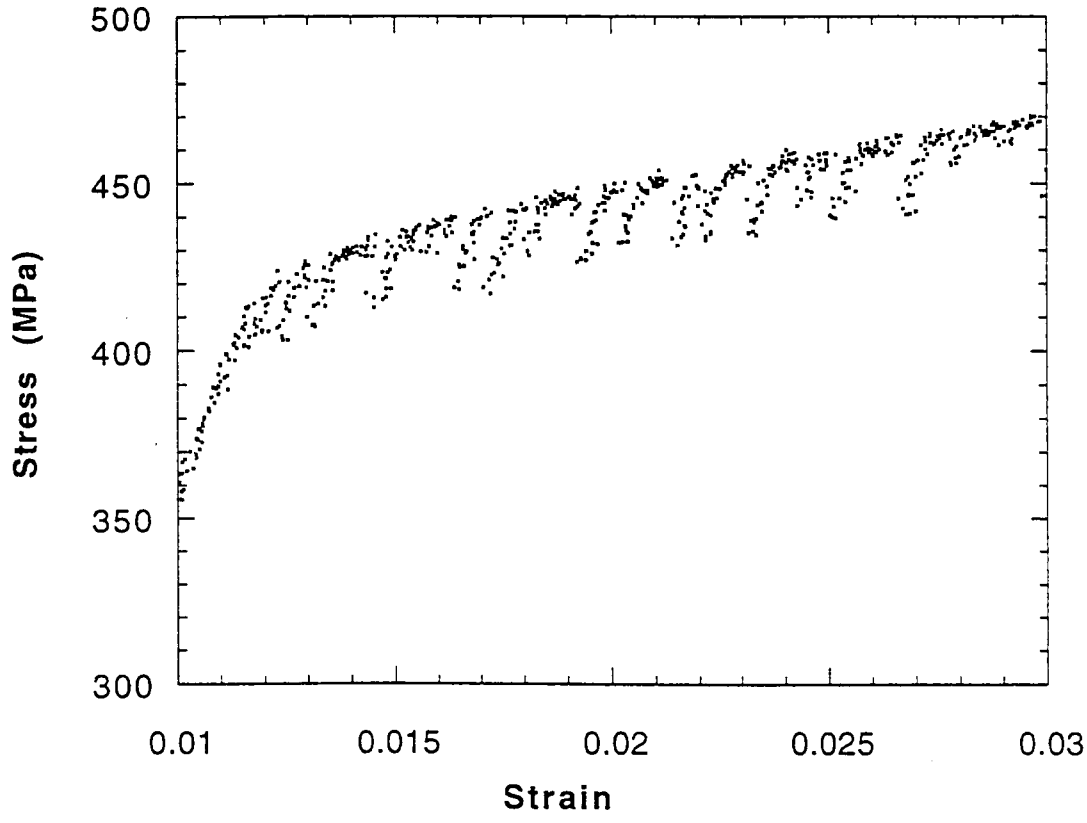



Figure 4.4: Magnified compressive stress-strain curve of Nb-15Al-25Ti tested at 600°C at a strain rate of $10^{-4}$ $s^{-1}$ showing serrated behavior.

characteristics, can also influence the superplastic behavior. In this study, the grain size of the materials was about 200 $\mu$m, before and after the testing. Therefore, superplasticity is not the mechanism of these tests.

Many years of investigation of high-temperature deformation mechanisms of crystalline metals have led to models correlating the mechanical characteristics of deformation with the structural changes taking place over a wide range of temperatures and strain rates. In these models, the global softening process (yield drop) is interpreted as resulting from dynamic recovery and dynamic recrystallization, with the addition of other softening mechanisms, such as adiabatic heating, coarsening of precipitates, modification of hard textures, and superplastic flow.

In some studies, the phenomenon of dynamic recrystallization has been treated as a quasi-homogeneous process characterized by a random distribution of the softening regions in the material. Other studies have emphasized, to a greater or lesser extent, the role of deformation bands as regions containing high deformation gradients and lattice misorientations, thereby becoming particularly preferential for the nucleation and development of new grains [101].

The group (iii) stress-strain curves displayed a peak stress in the initial stages of deformation, and then, the flow stress decreased to a constant value. The strain to the peak stress decreased as the deformation temperature was increased or the strain rate was decreased, as shown in Figure 4.2 and 4.3. This characteristic behavior indicates that the process is controlled by dynamic recrystallization [100,

101, 102, 103, 104] which can be proved by the presence of a dislocation subgrain structure, see Figure 4.45.

## 4.4 Yield Strength versus Strain Rate of Group I Alloys

The yield strength data from the tests are summarized in Table 4.1, and plotted in Figure 4.5. It can be seen that for the 10Ti and 25Ti alloys, the slopes of the yields stress versus strain rate curves at low strain rates ($< 10^{-4}$ $s^{-1}$) are higher than at high strain rates ($> 10^{-4}$ $s^{-1}$). In Figure 4.5, it can also be observed that at high strain rates ($> 10^{-4}$ $s^{-1}$), the curves are almost flat, which means that the yield strength is relatively independent of the strain rate. At low strain rates ($< 10^{-4}$ $s^{-1}$), however, the yield strength decreased sharply with decreasing strain rates. For all the alloys investigated, the yield strength decreased with an increase in test temperature. It is interesting to note that at 873 and 1173 K (600 and 900°C), the 10Ti alloy has a higher yield strength than the 25Ti and 40Ti alloys. These results are in good agreement with those of Shyue *et al.* [20, 78].

## 4.5 Microstructures of Group I As-Cast Alloys

The as-cast microstructure of the 10Ti alloy is typified by the micrographs in Figure 4.6. It is heterogeneous, with some regions appearing single phase but in most areas a two-phase structure has formed from the grain boundaries. In

Table 4.1: Compressive yield strength at various temperatures and strain rates.

| Alloy | Test Temperature (°C) | Compressive Yield Strength (MPa) | | |
|---|---|---|---|---|
| | | $5x10^{-2}$ $s^{-1}$ | $10^{-4}$ $s^{-1}$ | $10^{-5}$ $s^{-1}$ |
| Nb-15Al-10Ti | 400 | 684 | 664 | 632 |
| | 900 | 532 | 522 | 454 |
| Nb-15Al-25Ti | 25 | 902 | 851 | 730 |
| | 600 | 463 | 423 | 418 |
| | 900 | 402 | 285 | 112 |
| Nb-15Al-40Ti | 600 | 510 | 420 | 400 |
| | 900 | 360 | 180 | 113 |

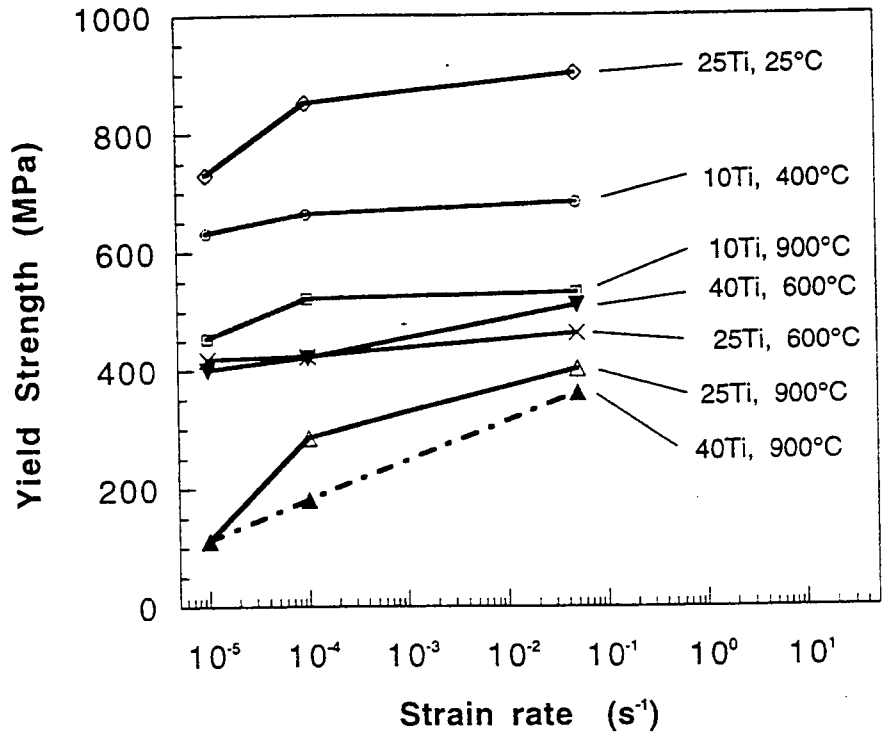



Figure 4.5: Compressive yield strength versus strain rate for group I alloys.

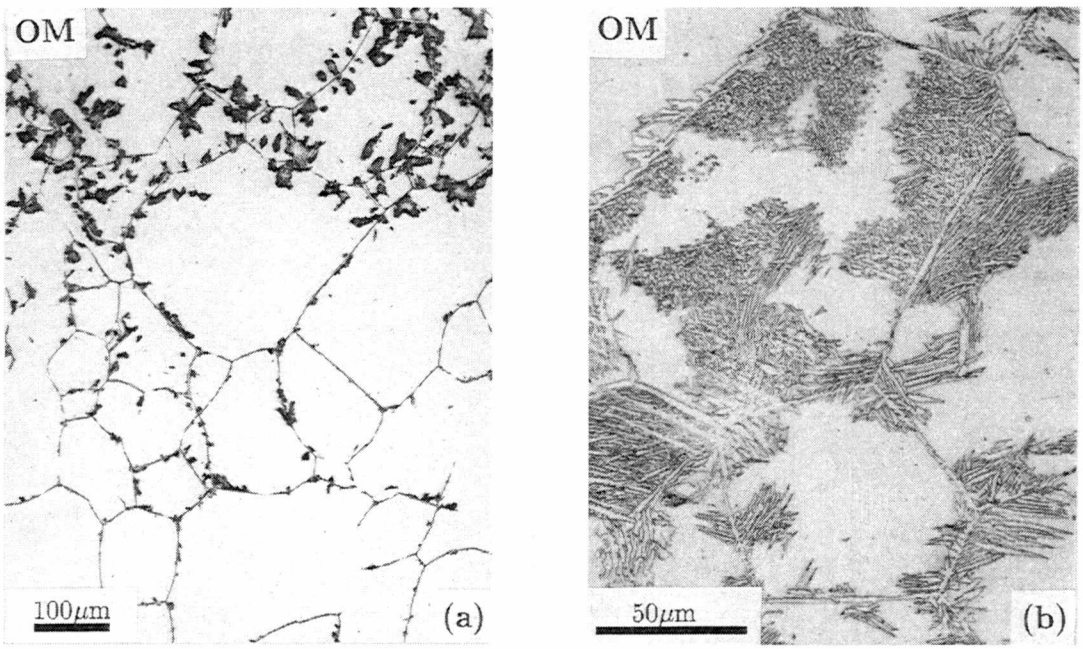



Figure 4.6: Microstructure of the as-cast Nb-15Al-10Ti alloy. A structure has formed at the grain boundaries, and its distribution in not homogeneous.

Figure 4.6b, dark areas are a structure containing a second phase. The variation in structure is probably due to chemical segregation associated with solidification. Transmission electron microscopy established that the matrix has the B2 structure, but there is diffuse streaking, similar to that reported by Naka *et al.* [28] for the as-cast condition, which they attribution to "elastic distortions from compositional fluctuations typical of a pre-precipitation stage". A phase has grown from the grain boundaries (Figure 4.7). The grain boundaries have a thin layer of these second phase (allotrimorph morphology [105]), from which side plates contiguous with it have grown (Figure 4.7a). In some areas these side plates have thickened to come into contact (Figure 4.7b).

The phase diagram in Figure 2.4 [22, 28] at 1473 K (1200°C) indicates that the 10Ti alloy should consist of the B2 and $\delta$ ($Nb_3Al$ + Ti) phases. It is assumed that the phase growing on and from the boundaries is $\delta$. In some locations, see Figure 4.8, arrows, cracking has occurred in the grain boundary $\delta$ layer, but not in the side-plates. The microstructures of the as-cast 25 and 40Ti alloys appeared to be single phase in optical microscopy (e.g., Figure 4.9). Electron diffraction showed the B2 structure, but there was some diffuse streaking, maybe associated with $\omega$ phase. The 25Ti alloy showed no grain boundary cracking, and the 40Ti alloy apparently did not.

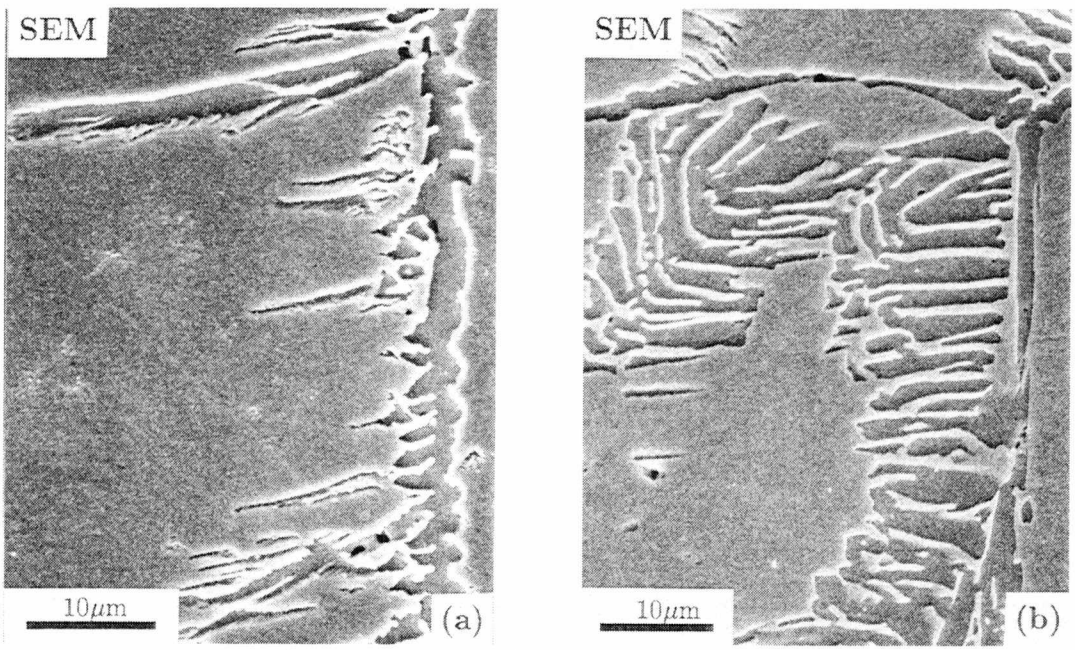



Figure 4.7: Microstructure of as-cast Nb-15Al-10Ti alloy showing details of the side-plates which have grown from the grain boundaries.

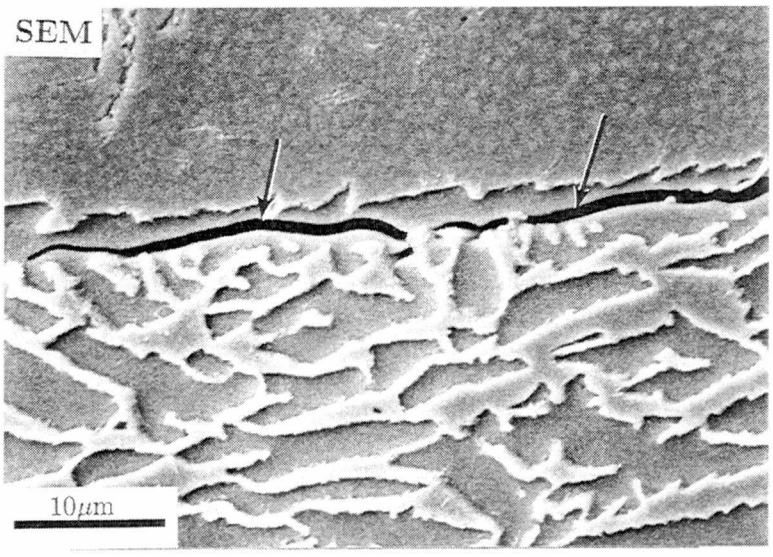



Figure 4.8: Microstructure of the as-cast Nb-15Al-10Ti alloy showing cracks in the grain boundary layer.

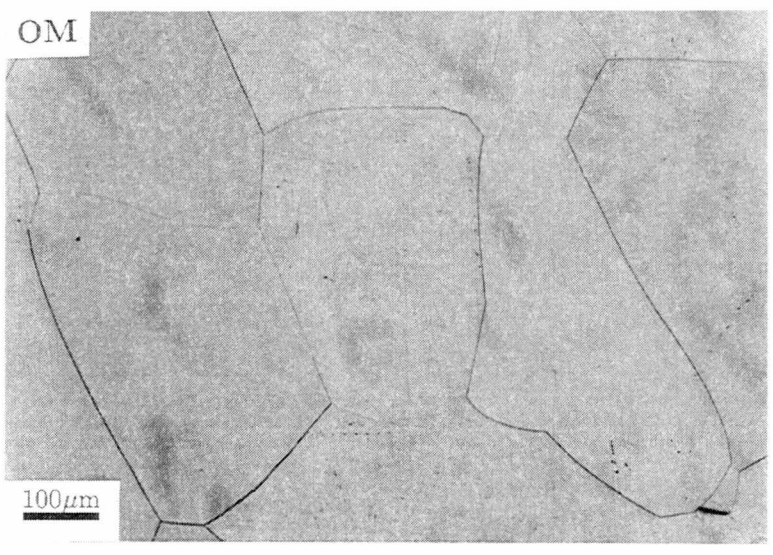



Figure 4.9: Microstructure of the as-cast Nb-15Al-40Ti alloy showing single phase.

## 4.6 Microstructures of Compression Tested Specimens of Group I Alloys

One feature of the testing that may affect the microstructure, which in turn may affect the mechanical properties, is additional transformation which occurs upon heating to the test temperature and during the test period. All tests were terminated after about 5% total strain. The time to attain this strain was about 5, 15 and 90 minutes for the strain rates of $5x10^{-2}$, $10^{-4}$ and $10^{-5}$ $s^{-1}$, respectively.

Figure 4.10 shows the microstructure of the Nb-15Al-10Ti alloy which was tested at 1173 K (900°C) at a strain rate of $5x10^{-2}$ $s^{-1}$. This sample showed the common yielding behavior (i.e., group i). This microstructure appears similar to that of the as-cast condition (Figure 4.6b), but Figure 4.11 shows that there may have been additional side-plate growth during the 5 minutes required for testing. Note in Figure 4.10 (at a) that there is extensive cracking along the grain boundary layer, and this is shown in more detail in Figure 4.12. Cracking is also present in the layer plates inside the grains, in b in Figure 4.10. No cracking was observed in the side-plates.

Figure 4.13 shows the microstructure of the Nb-15Al-10Ti alloy which was tested at 1173 K (900°C) at a strain rate of $10^{-5}$ $s^{-1}$. The grain boundary layer shows cracking (see arrows). Figure 4.14 shows that the tips of the side-plates appear to have grown during the 90 minutes required for testing. This sample showed a yield point (group iii behavior).

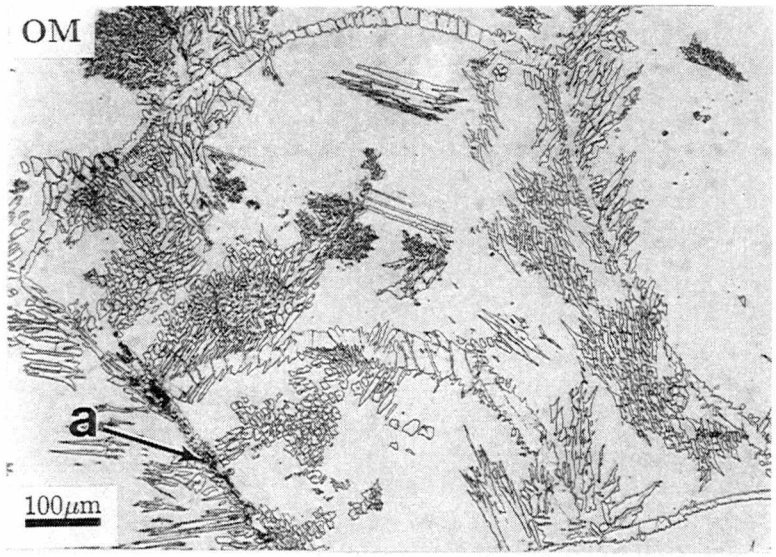



Figure 4.10: Microstructure of the as-cast Nb-15Al-10Ti alloy after compression testing at 900°C at a strain rate of $5x10^{-2}$ $s^{-1}$. Note cracking along grain boundary phase.

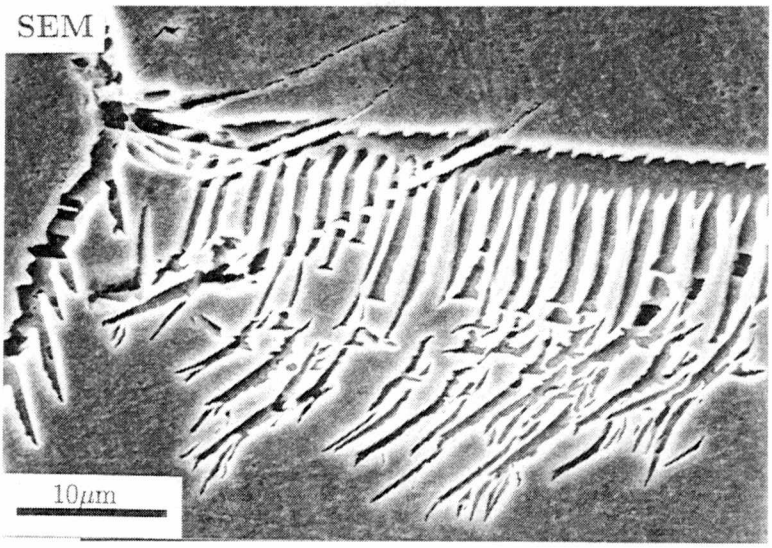



Figure 4.11: Microstructure of the as-cast Nb-15Al-10Ti alloy after compression testing at 900°C at a strain rate of $5x10^{-2}$ $s^{-1}$, showing what appears to be additional growth of the side-plates during testing. The time at 900°C was about 5 min.

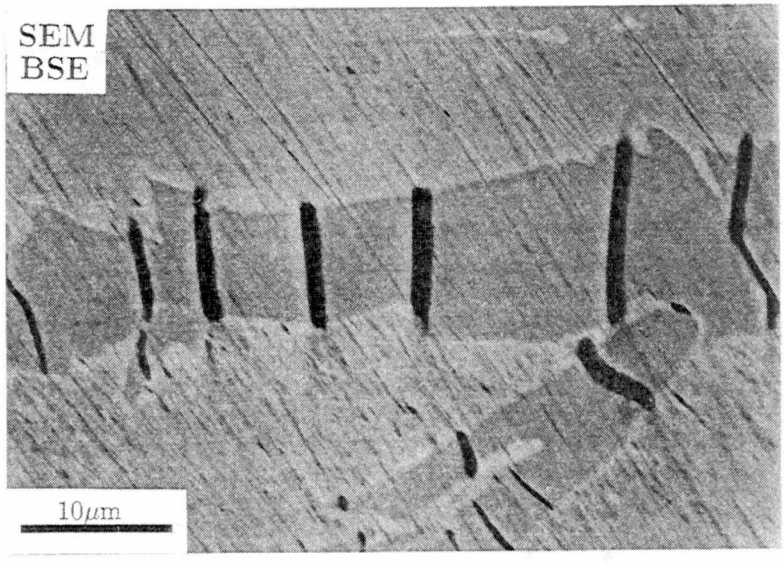



Figure 4.12: Areas such as noted in Figure 4.10 showing extensive cracking of the grain boundary $\delta$ phase.

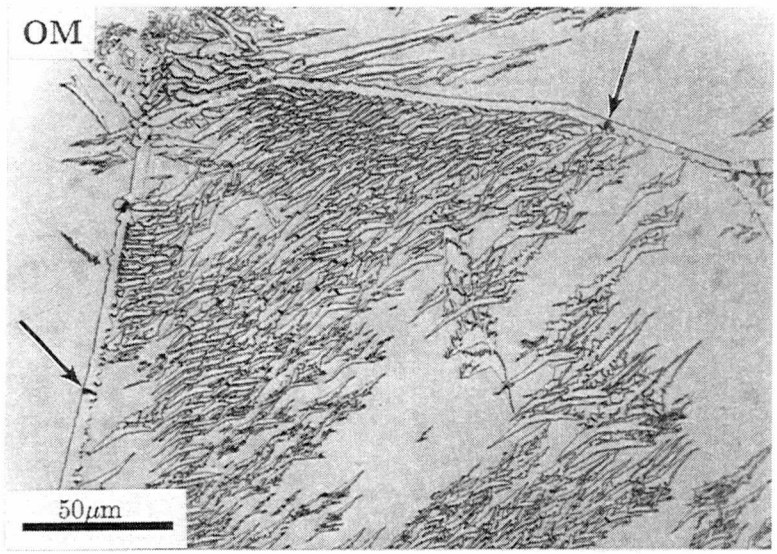



Figure 4.13: Microstructure of the as-cast Nb-15Al-10Ti alloy after compression testing at 900°C at a strain rate of $10^{-5}$ $s^{-1}$. The time at 900°C was about 90 min.

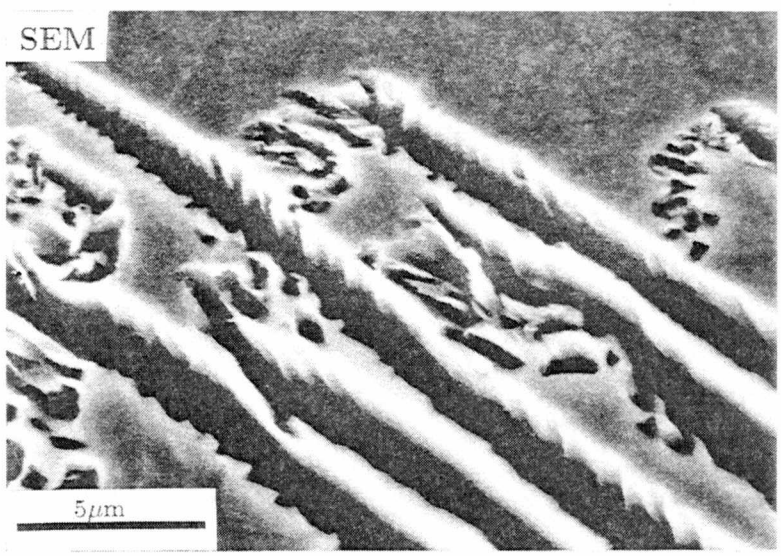



Figure 4.14: Details of the side-plates in Figure 4.13 showing what appears to be growth from the tips, presumably occurring during the 90 minutes testing period.

The Nb-15Al-25Ti alloy tested at 873 K (600°C) at a strain rate of $10^{-4}$ and $10^{-5}$ $s^{-1}$ showed serrated yielding (Figure 4.2) (group ii behavior). The microstructure was single phase, but there was grain boundary cracking (Figure 4.15).

Shyue *et al.* [20, 78] have determined mechanical properties of Nb-15Al, -10Ti and -40Ti alloys in the as-cast and in various heat treated conditions. They make no mention of cracks in the castings, nor in the compression-tested samples, although the terminal strain was only about 2%, not 5% as in this study. They also make no mention of either a yield point or serrated behavior. They indicated that in the as-cast condition, their alloys had mainly the B2 structure, but a plate-like precipitate formed with the $\delta$ structure, and implied that this is a brittle phase, whereas they found the $\beta$ to be ductile.

The matrix of the group I alloys is the B2 structure. For example, the selected area diffraction (SAD) pattern of the Nb–15Al–40Ti alloy tested at 873 K (600°C) and a strain rate of $10^{-5}$ $s^{-1}$ with the corresponding $<100>_{B2}$ zone axis is shown in Figure 4.16(b). Superlattice spots are clearly seen in the SAD pattern and anti-phase boundaries (APB) are also seen in the dark field (DF) image (Figure 4.16(a)).

The dislocation density in the tested alloys is very high. Tangled dislocations, such as shown in the bright field (BF) image of Figure 4.17, are exhibited in every alloy, since the specimens were examined after 5% strain. Occasionally single dislocations were found in the matrix, as shown in Figure 4.18.

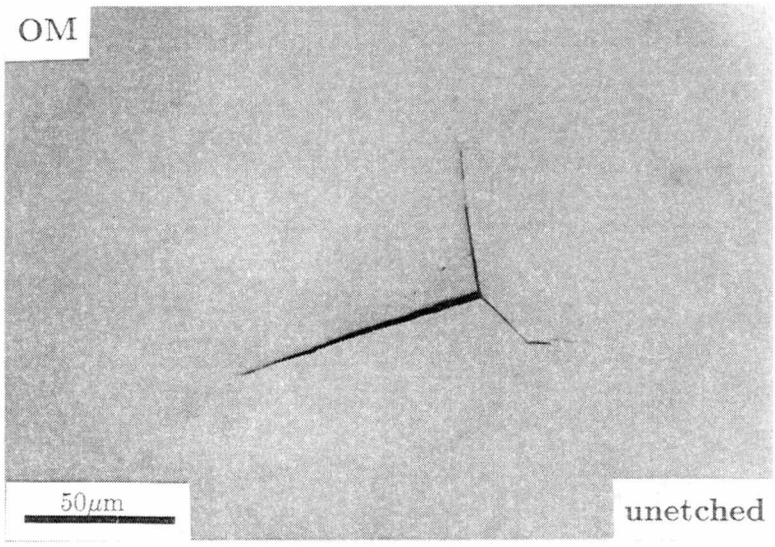



Figure 4.15: Unetched microstructure of the Nb-15Al-25Ti alloy, tested at room temperature and a strain rate of $10^{-4}$ $s^{-1}$, showing grain boundary cracks.

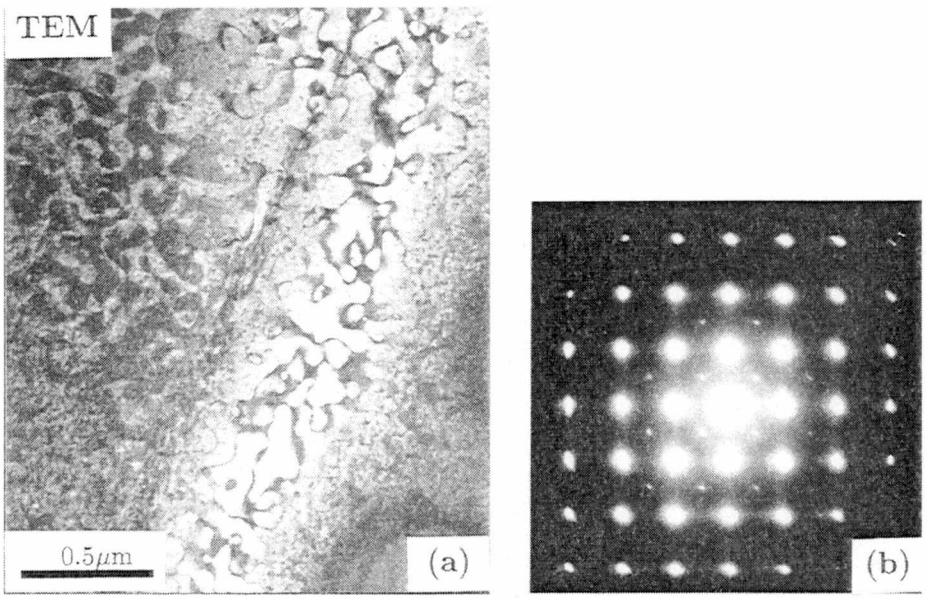



Figure 4.16: Micrograph of Nb–15Al–40Ti alloy tested at 600°C and strain rate of $10^{-5}$ $s^{-1}$. (a) DF image showing APB obtained using $<001>_{B2}$ type superlattice reflection. (b) The corresponding SAD pattern taken in $<001>_{B2}$ zone axis showing B2 type superlattice spots.

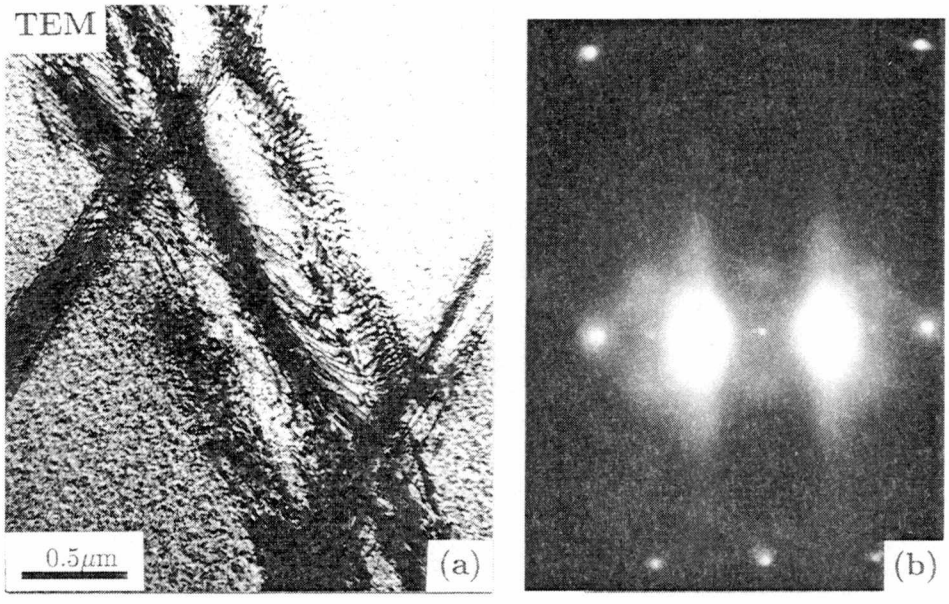



Figure 4.17: Micrograph of Nb–15Al–40Ti alloy tested at 600°C and strain rate of $10^{-5}$ $s^{-1}$. (a) BF image showing dislocations tangled and crossed. (b) The corresponding SAD pattern taken in $[012]_{B2}$ zone axis.

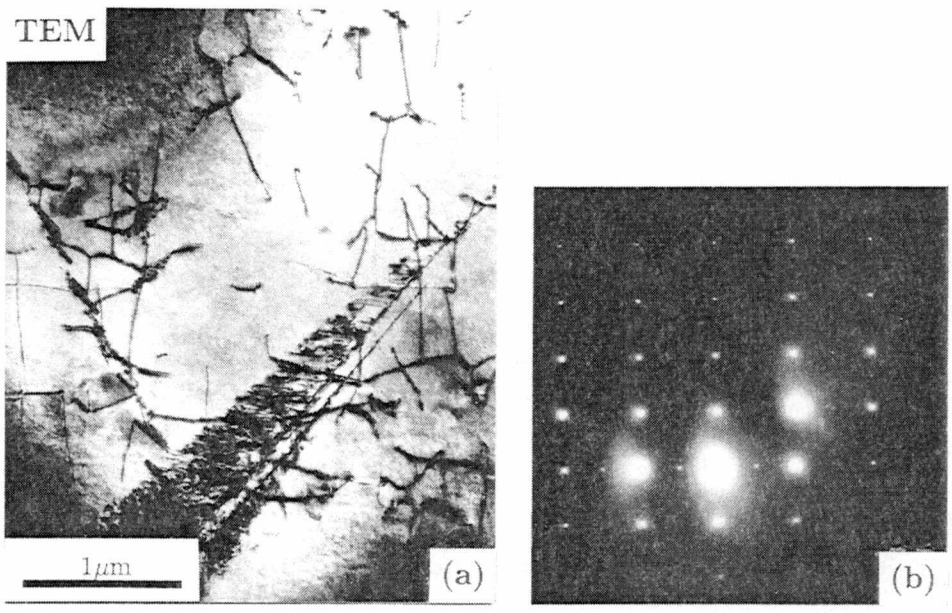



Figure 4.18: Micrograph of Nb–15Al–40Ti alloy tested at 900°C and strain rate of $10^{-4}$ $s^{-1}$. (a) BF image showing dislocations tangled and scattered. (b) The corresponding SAD pattern taken in $<011>_{B2}$ zone axis showing B2 type superlattice spots.

## 4.7 Stress-Strain Behavior of Group II Alloys

The stress-strain curves for the group II alloys of 10Ti, 25Ti and 40Ti are presented in Figure 4.19–4.21. All testing was done at 1173 K (900°C) and a strain rate of $10^{-4}$ $s^{-1}$. For group I alloys, there are three types of curves: (i) the normal stress-strain curves, which do not exhibit a yield drop behavior, (ii) the serrated stress-strain curves manifesting the periodic yielding phenomenon and (iii) the stress-strain curves indicating yield drop behavior, i.e., an initial increase in the strength followed by a decrease in strength. In group II alloys, there are only two types: group (i) behavior, which do not exhibit a yield drop behavior or serrated yielding, and group (iii) behavior, the yield drop behavior, which shows an initial increase in the strength followed by a decrease in strength.

In Figure 4.19, the stress-strain curves of 10Ti alloy, except for those heat treated at 1173 K (900°C) for 100 hours and heat treated at 1373 K (1100°C) for 10 hours, exhibit group (i) behavior; the others exhibit the group (iii) behavior. In Figure 4.20, the stress-strain curves of 25Ti alloy, heat treated at 873 K (600°C) for 10 hours and 100 hours, show the group (iii) behavior. Others show the group (i) behavior. In Figure 4.21, the stress-strain curves of 40Ti alloy exhibit the group (iii) behavior, except for heat treated at 1373 K (1100°C) for 10 hours, which exhibits the group (i) behavior.

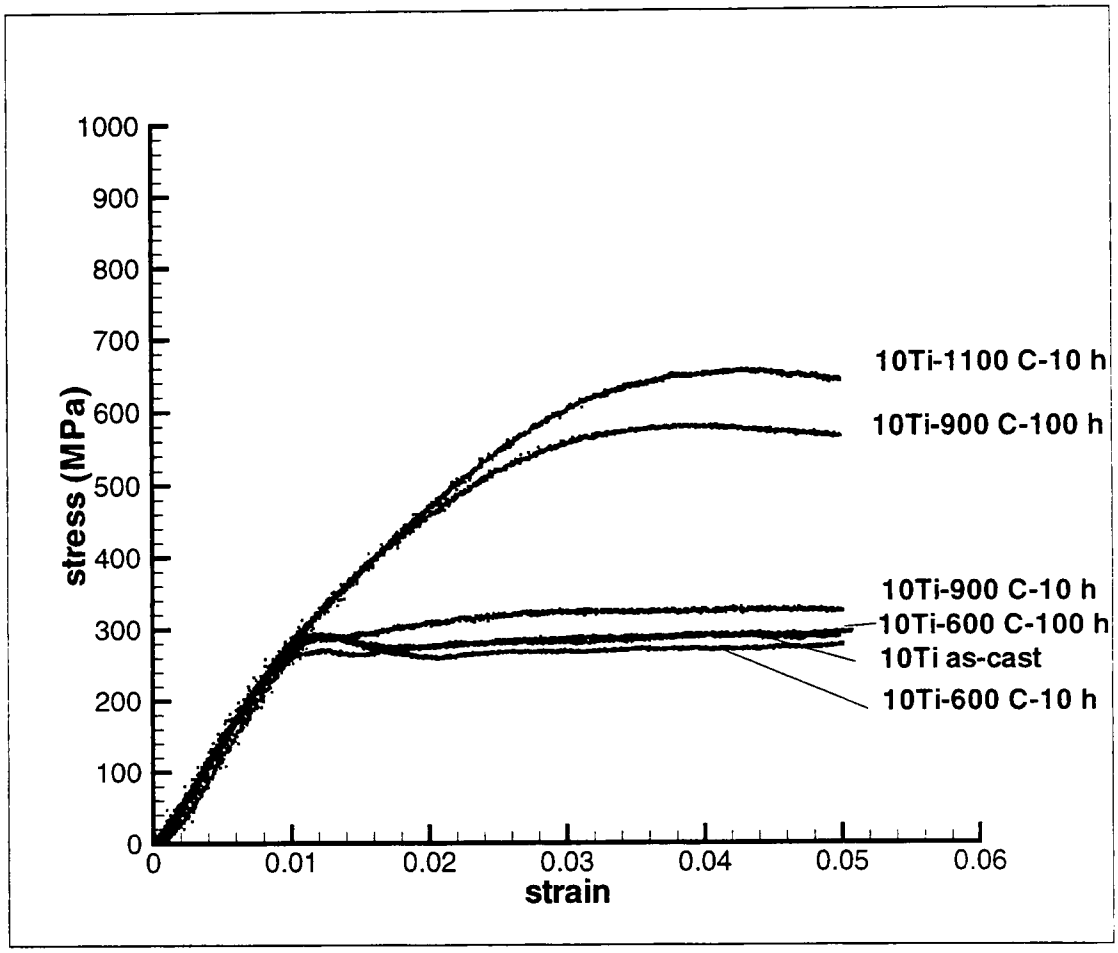



Figure 4.19: Compressive stress versus strain curves of Nb-15Al-10Ti group II alloys tested at 1173 K (900°C) and a strain rate of $10^{-4}$ $s^{-1}$.

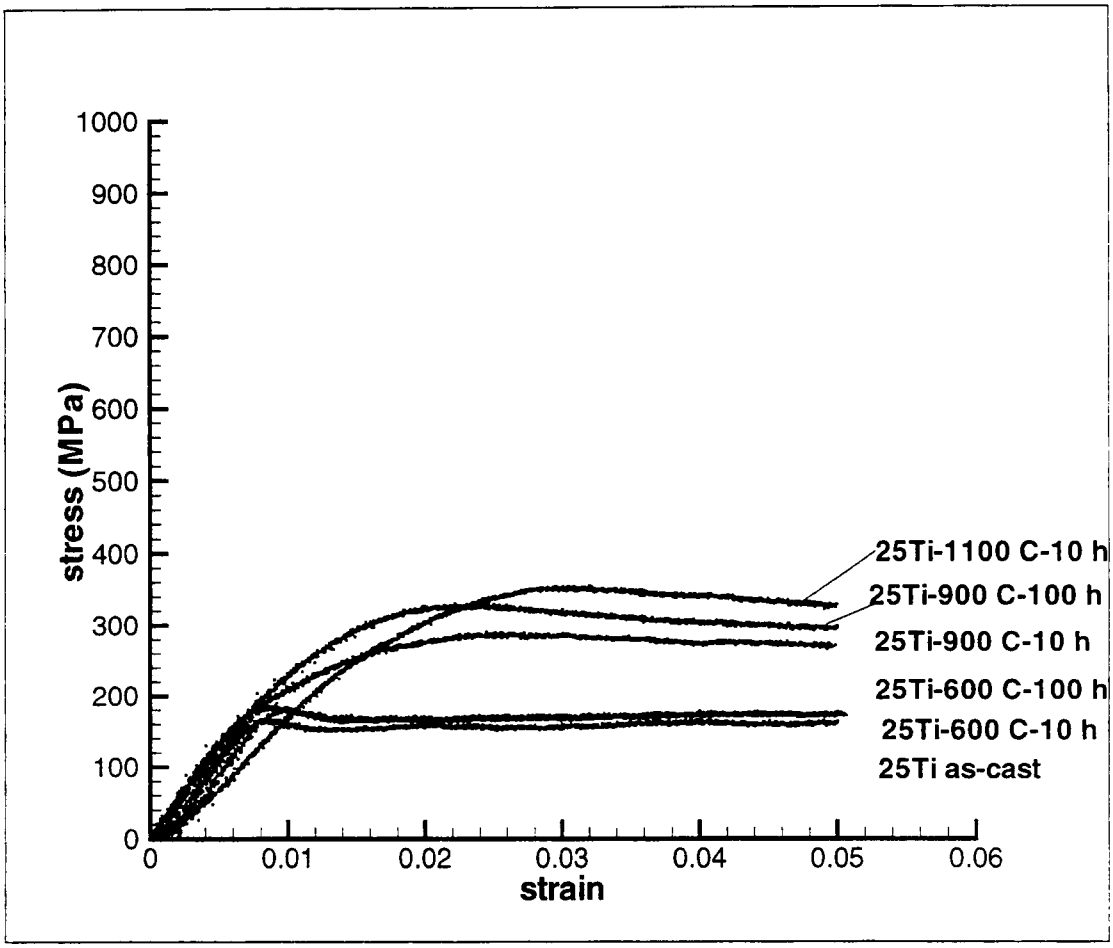



Figure 4.20: Compressive stress versus strain curves of Nb-15Al-25Ti group II alloys tested at 1173 K (900°C) and a strain rate of $10^{-4}$ $s^{-1}$.

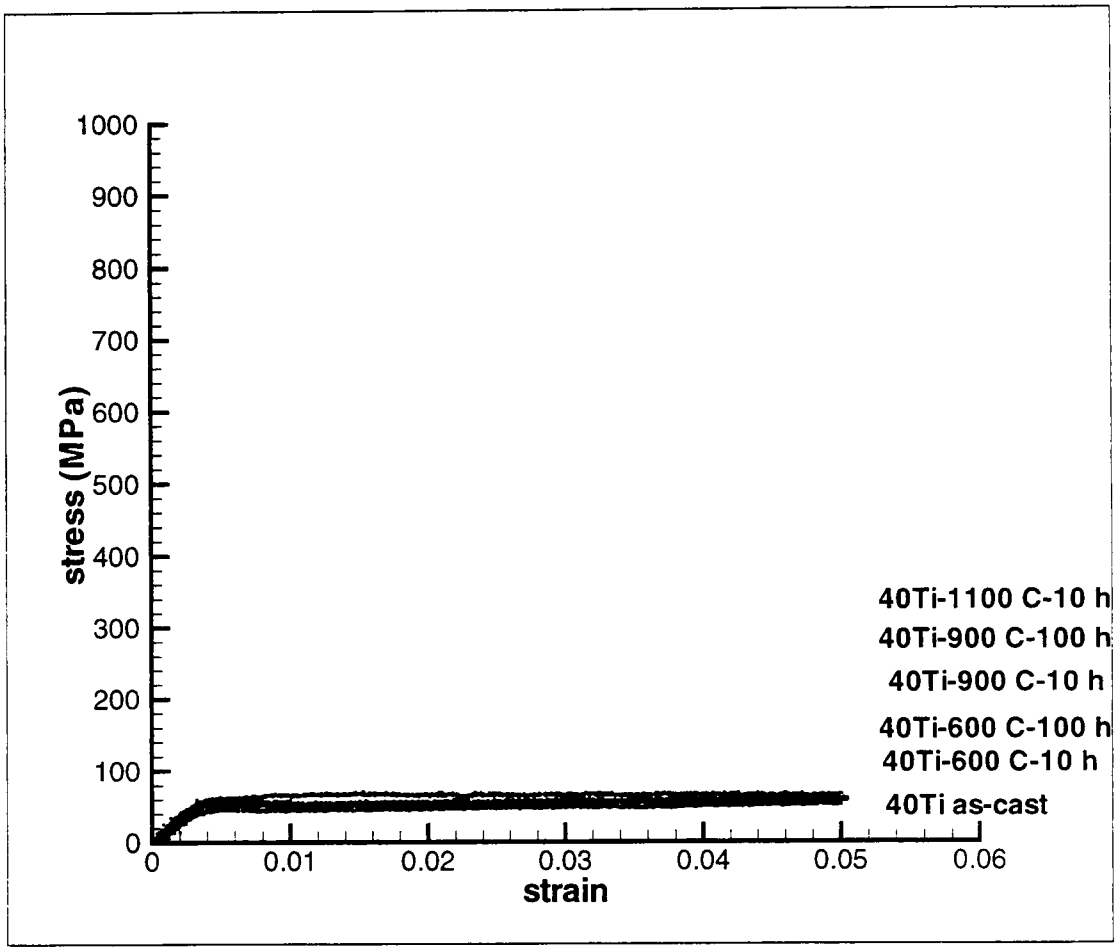



Figure 4.21: Compressive stress versus strain curves of Nb-15Al-40Ti group II alloys tested at 1173 K (900°C) and a strain rate of $10^{-4}$ $s^{-1}$.

## 4.8 Yield Strength versus Aging Temperature of Group II Alloys

The yield strength data of group II alloys are summarized in Table 4.2, and plotted in Figure 4.22. It can be seen that for heat treatment at 873 K (600°C) for 10 and 100 hours and for heat treatment at 1173 K (900°C) for 10 hours the yield strengths are almost the same as for the as-cast condition. For heat treatment at 1173 K (900°C) for 100 hours and heat treatment at 1373 K (1100°C) for 10 hours, the yield strength increased. Also the higher the niobium content, the higher the yield strength.

Compared with the group I alloys in the as-cast condition, the yield strengths of the group II alloys are lower. This will be discussed in a subsequent section. Figure 4.23 compares the results to those of Shyue *et al.* [20, 78]. 40Ti of group I alloy agrees with their data, but 10Ti alloy is higher than their result. However, for group II alloys, both 10Ti and 40Ti are lower than their result.

## 4.9 Microstructures of Compression Tested Specimens of Group II Alloys

The materials of group II alloys, Nb-15Al-10Ti, -25Ti and -40Ti, were cast at ORNL. The microstructures of as-cast 10Ti alloy, five heats, are shown in Figure 4.24. The dendrite structure caused by high cooling rate during casting is clearly exhibited in the figures. A SEM back scattered electron (BSE) image of

Table 4.2: Compressive yield strength at testing temperature of 900°C and strain rate of $10^{-4}$ $s^{-1}$ for various heat treatment temperatures and holding times.

| Alloy | Compressive Yield Strength (MPa) | | | | | |
|---|---|---|---|---|---|---|
| | as-cast | 600°C | | 900°C | | 1100°C |
| | | 10 hrs. | 100 hrs. | 10 hrs. | 100 hrs. | 10 hrs. |
| Nb-15Al-10Ti | 270 | 291 | 291 | 289 | 375 | 395 |
| Nb-15Al-25Ti | 165 | 180 | 184 | 197 | 250 | 274 |
| Nb-15Al-40Ti | 46 | 52 | 52 | 50 | 61 | 58 |

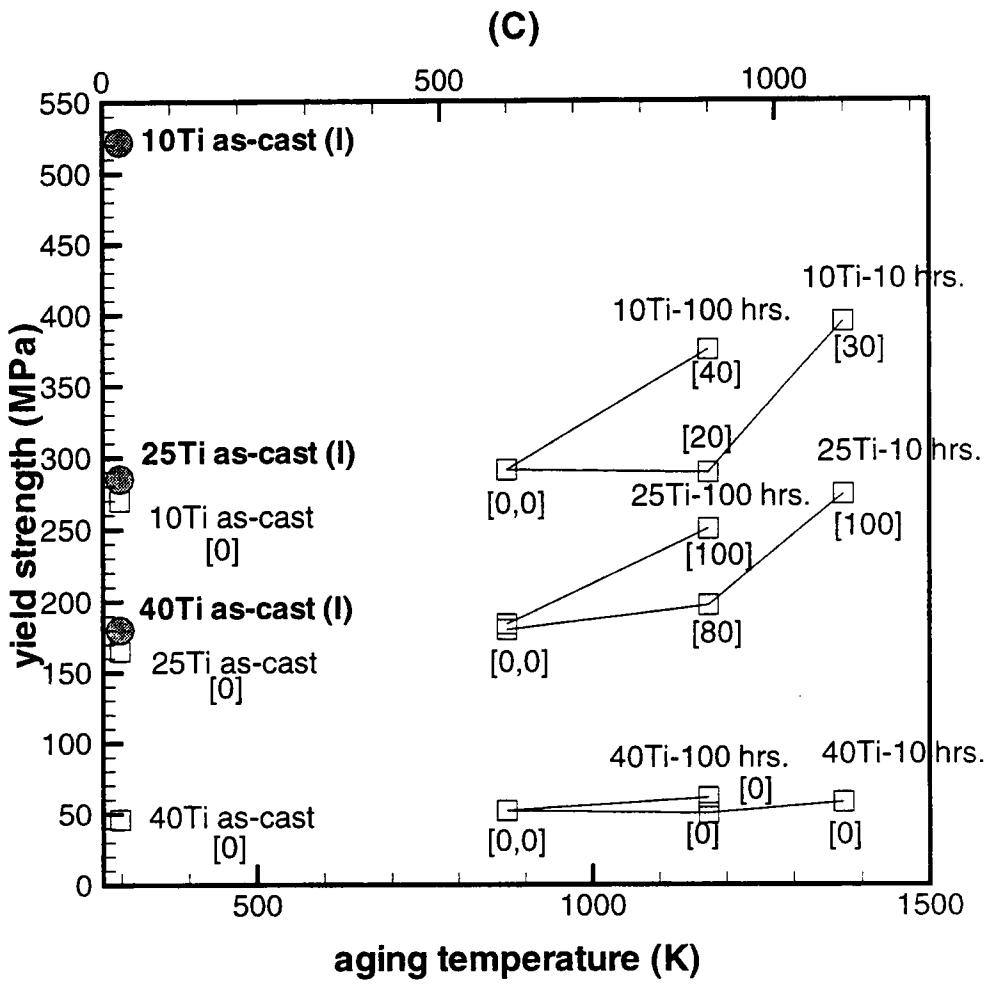



Figure 4.22: Compressive yield strength versus aging temperature for group II alloys tested at 900°C and strain rate of $10^{-4}$ $s^{-1}$. Also shown are data for as-cast group I alloys. The numbers in brackets are estimates of the amount of $\delta$ present before testing.

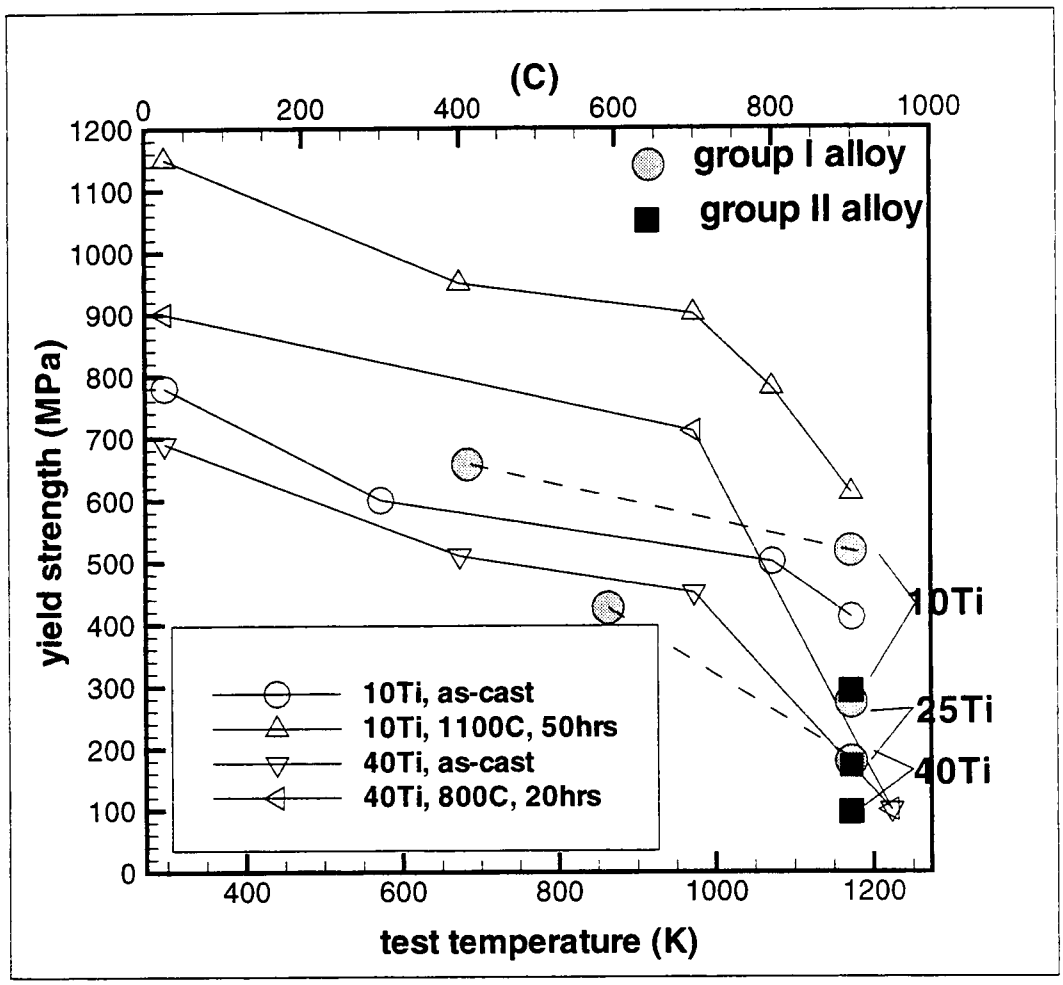



Figure 4.23: Compressive yield stress for the as-cast Nb-15Al-10Ti and Nb-15Al-40Ti alloys compared to data of Shyue *et at.* [20]. The strain rate was $10^{-4}$ $s^{-1}$.

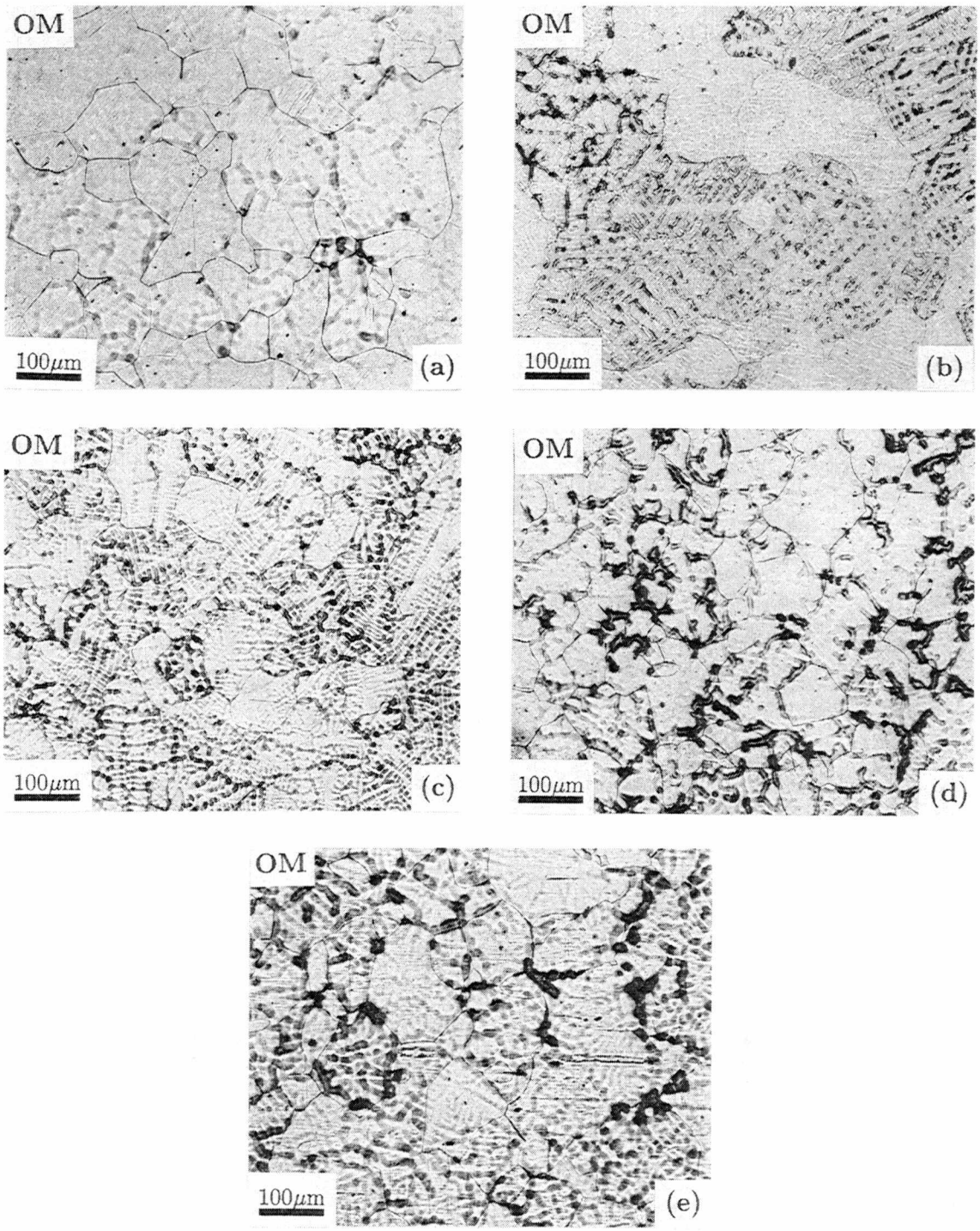



Figure 4.24: Microstructures of the as-cast Nb-15Al-10Ti alloy. (a) first heat. (b) second heat. (c) third heat. (d) fourth heat. (e) fifth heat.

the unetched microstructure, shown in Figure 4.25, shows the cored structure. The bright area is Nb-rich. The dendrite arms in Figure 4.24 (b) and (c) are finer than (a), (d) and (e).

Micrographs of as-cast 25Ti alloy, four heats, are shown in Figure 4.26. Coring is clearly found in the three heats of this alloy. One of the heats does not exhibit this structure, but shows a two-phase structure, i.e., Figure 4.26(d). The matrix is the B2 phase, while the special shapes inside the grains were found by EDS to be a Nb-rich phase.

A micrograph of 40Ti as-cast alloy, the only heat, is shown in Figure 4.27. Particles (at A) are exhibited.

Micrographs of as-cast and tested of 10Ti, 25Ti and 40Ti alloys are shown in Figure 4.28, 4.29 and 4.30, respectively. For 10Ti and 25Ti alloys, intergranular Widmanstätten plates, A15 ($\delta$) phase, were found both at grain boundaries and within the grains. Cracks were found in 10Ti alloy inside the $\delta$ phase, indicated by arrows in Figure 4.28. In addition to the plates, Nb-rich particles were found in the B2 matrix. As for the 40Ti alloy, it is almost the same structure compared to the as-cast condition (Figure 4.27).

Micrographs of 10Ti alloy, heat-treated at 873 K (600°C), are shown in Figure 4.31. (a) and (b) are for 10 hours holding time, while (c) and (d) are for 100 hours holding time. (a) and (c) are as-heat-treated, while (b) and (d) are tested. Nb-rich particles were found in both for 10 and 100 hours samples, but not in

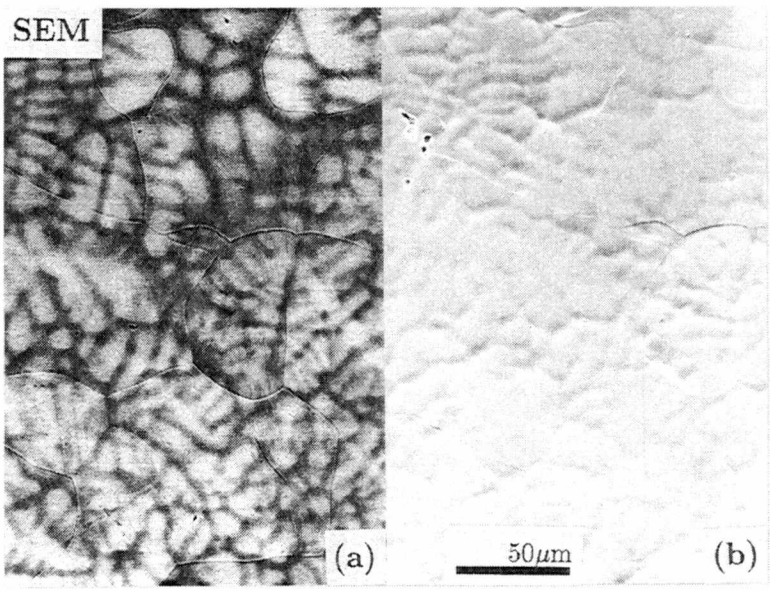



Figure 4.25: Unetched microstructure of the as-cast Nb-15Al-10Ti alloy. (a) BSE image. Brighter image is Nb-rich region in cored due to high cooling rate during solidification. (b) SE image.

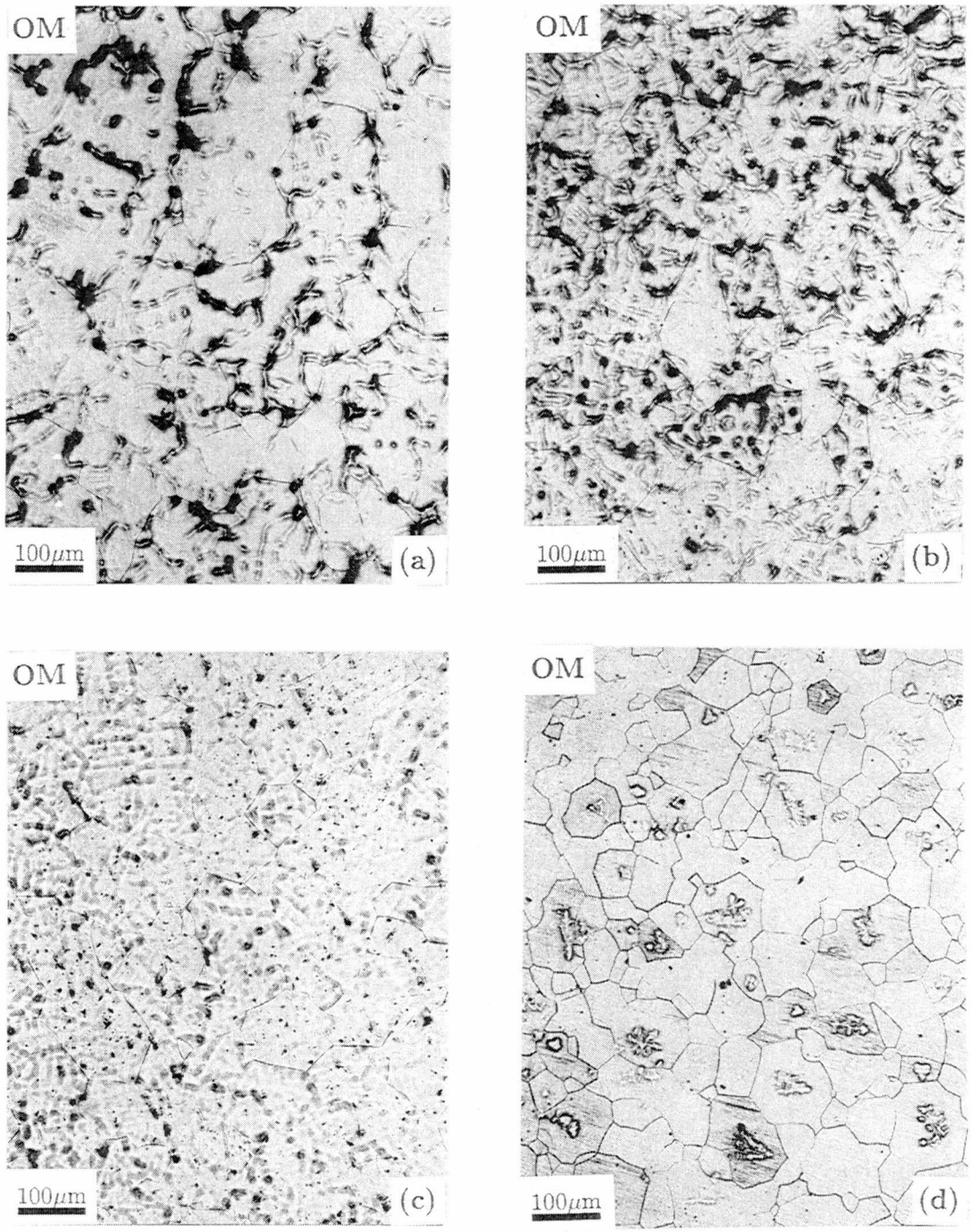



Figure 4.26: Microstructures of the as-cast Nb-15Al-25Ti alloy. (a) first heat. (b) second heat. (c) third heat. (d) fourth heat. The morphology of (d) is different from others.

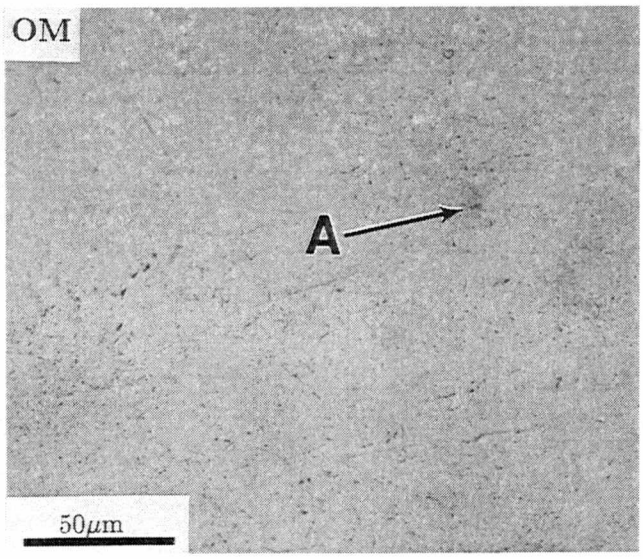



Figure 4.27: Microstructure of the as-cast Nb-15Al-40Ti alloy showing particles in the matrix.

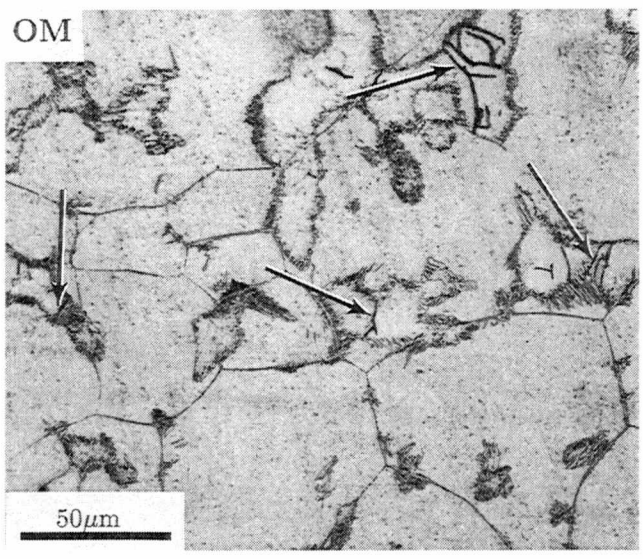



Figure 4.28: Microstructure of the as-cast and tested Nb-15Al-10Ti alloy.

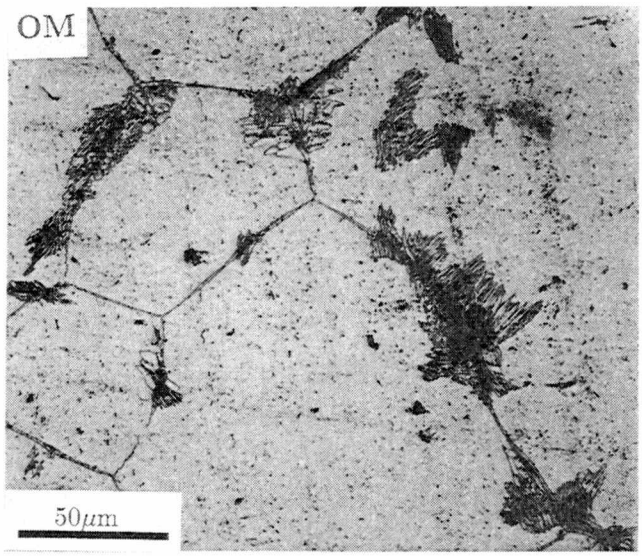



Figure 4.29: Microstructure of the as-cast and tested Nb-15Al-25Ti alloy.

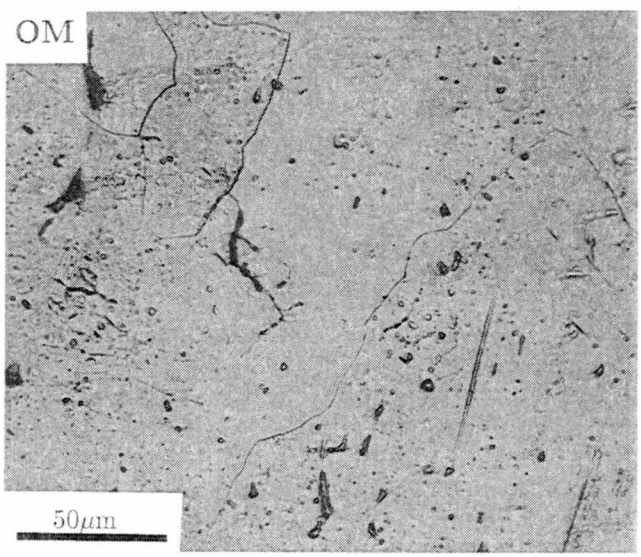



Figure 4.30: Microstructure of the as-cast and tested Nb-15Al-40Ti alloy.

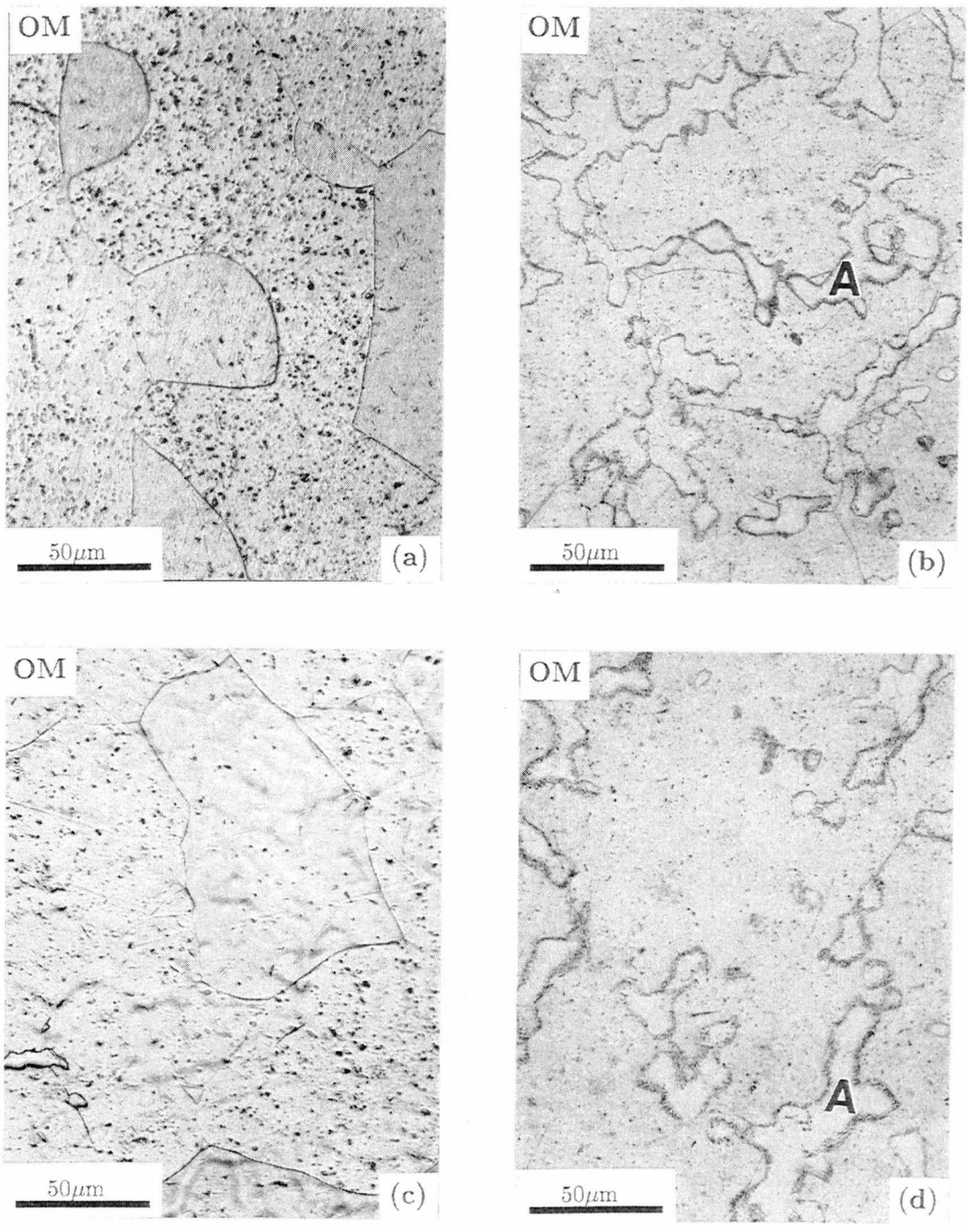



Figure 4.31: Microstructures of the Nb-15Al-10Ti alloy, heat-treated at 873 K (600°C). (a) holding for 10 hours and as-heat-treated. (b) holding for 10 hours and tested. (c) holding for 100 hours and as-heat-treated. (d) holding for 100 hours and tested.

the as-cast condition (Figure 4.24). In (b) and (d) at A, the white areas, the Nb content is higher than the matrix, so these areas are assumed to be the $\delta$ phase. At the edge of the $\delta$ phase are Widmanstätten side-plates. The $\delta$ phase formed during testing at 1173 K (900°C), not during aging at 873 K (600°C). In the tested samples, the Nb-rich particles appeared to be smaller than in the as-heat-treated samples.

Micrographs of 25Ti alloy, heat-treated at 873 K (600°C), are shown in Figure 4.32. (a) and (b) are for 10 hours holding time, while (c) and (d) are for 100 hours holding time. (a) and (c) are as-heat-treated alloy, while (b) and (d) are tested. A cored structure can still be found in the 10 hours holding sample, but not for the 100 hours sample. Widmanstätten plates formed during testing at 1173 K (900°C) for about 10 minutes. Nb-rich particles were formed in B2 matrix.

Micrographs of 40Ti alloy, heat-treated at 873 K (600°C), are shown in Figure 4.33. (a) and (b) are for 10 hours holding time, while (c) and (d) are for 100 hours holding time. (a) and (c) are as-heat-treated alloy, while (b) and (d) are tested. More Nb-rich particles were found in all samples compared to the as-cast condition (Figure 4.27). The microstructures of the 40Ti alloy heat treated at 873 K (600°C) did not fit the pattern of the other specimens. The microstructure of the specimen aged 10 hours (Figure 4.33(a)) shows dark regions which at higher magnification were revealed to be a network of fine lines, not present in the unetched condition. Recall that the 'as-cast' condition for this alloy was as-cast

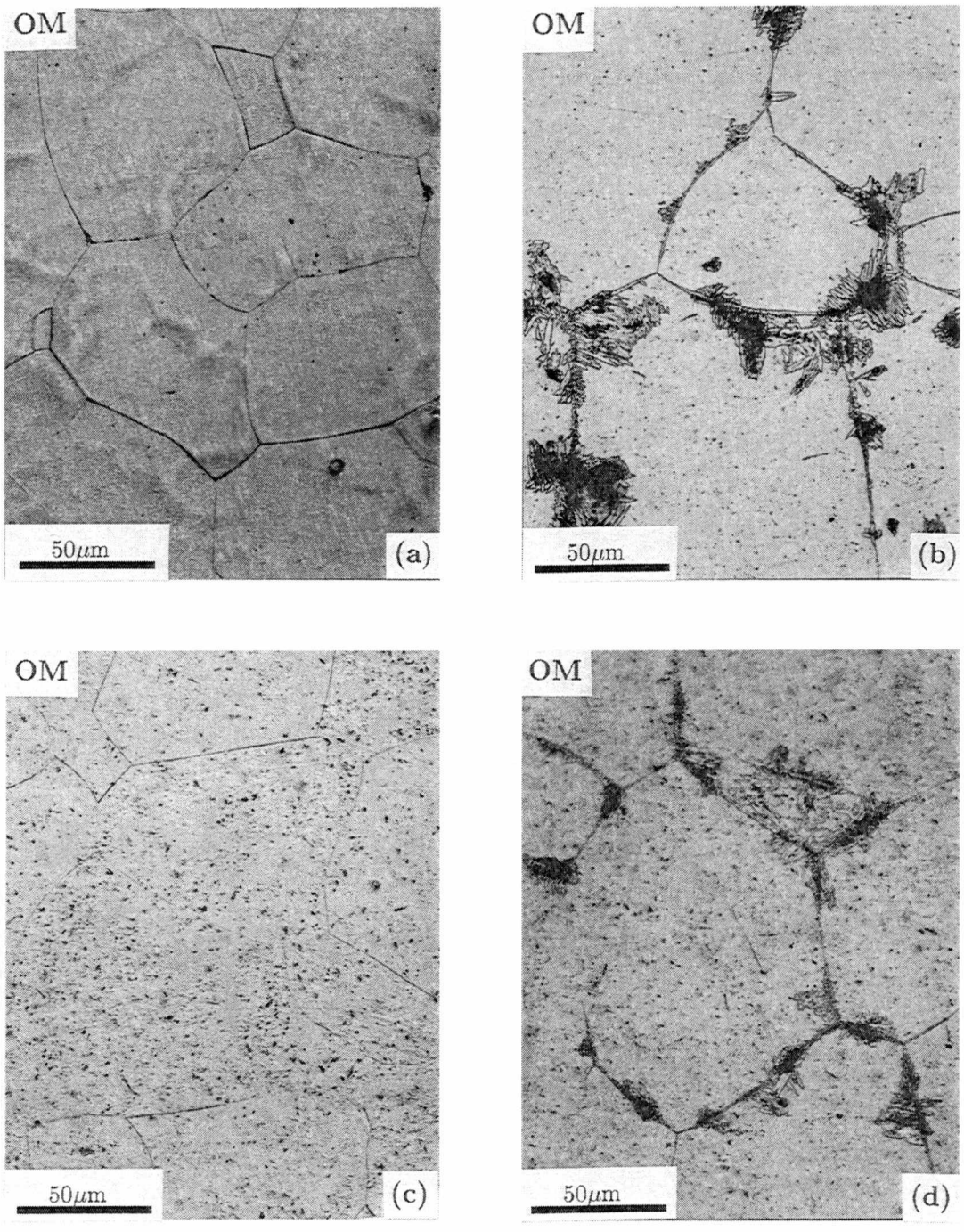



Figure 4.32: Microstructures of the Nb-15Al-25Ti alloy, heat-treated at 873 K (600°C). (a) holding for 10 hours and as-heat-treated. (b) holding for 10 hours and tested. (c) holding for 100 hours and as-heat-treated. (d) holding for 100 hours and tested.

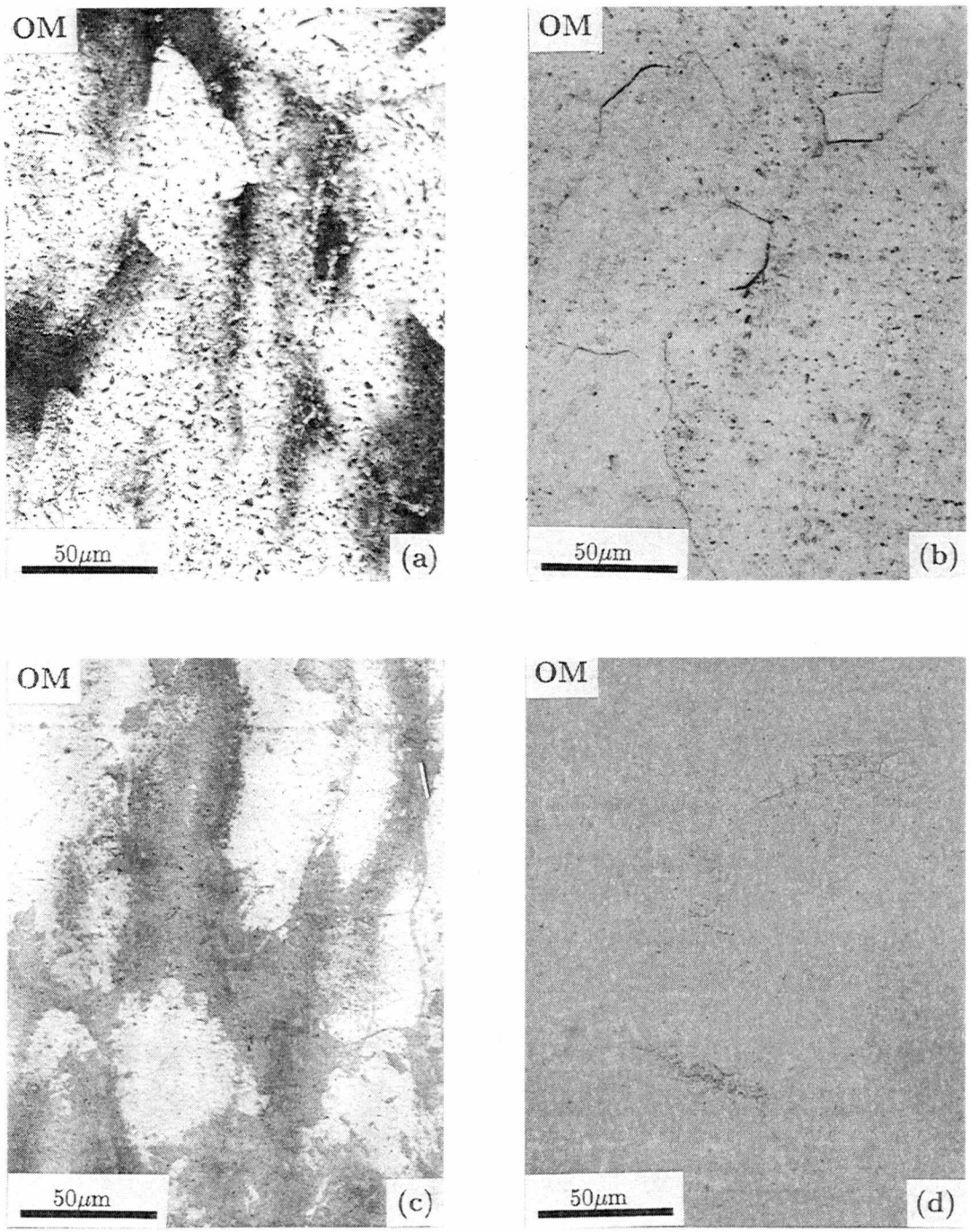



Figure 4.33: Microstructures of the Nb-15Al-40Ti alloy, heat-treated at 873 K (600°C). (a) holding for 10 hours and as-heat-treated. (b) holding for 10 hours and tested. (c) holding for 100 hours and as-heat-treated. (d) holding for 100 hours and tested.

then hot rolled, in which the microstructure was single phase B2 (Figure 4.27). It may be that the fine line network is due to etching of subgrain boundaries formed during the low temperature aging. The microstructure of the specimen aged 100 hours is shown in Figure 4.33(c). No line network etched out, but the structure is ill defined, which again may be due to recovery in the as-cast and hot worked material. After testing, the specimens appeared single phase B2 (Figure 4.33(b) and (d)).

Micrographs of 10Ti alloy, heat-treated at 1173 K (900°C), are shown in Figure 4.34. (a) is holding for 10 hours and is as-heat-treated, while (b) is holding for 10 hours and tested. (c) is for 100 hours holding time and tested. Both Nb-rich particles and intergranular Widmanstätten plates were found in all the samples. The Widmanstätten plates of as-heat-treated sample are finer than those of the tested sample. The amount of Widmanstätten plates in the tested sample heat-treated for 10 hours is less than in the tested sample heat-treated for 100 hours. Unfortunately, there were no samples for heat treatment at 1173 K (900°C) for 100 hours for the 10Ti, 25Ti and 40Ti alloys.

Micrographs of 25Ti alloy, heat-treated at 1173 K (900°C), are shown in Figure 4.35. (a) is holding for 10 hours and is as-heat-treated, (b) is holding for 10 hours and tested, and (c) is for 100 hours holding time and tested. Nb-rich particles were found for 10 hours holding time both as-heat-treated and tested. Widmanstätten plates were found in all samples. The dark areas consist of finer

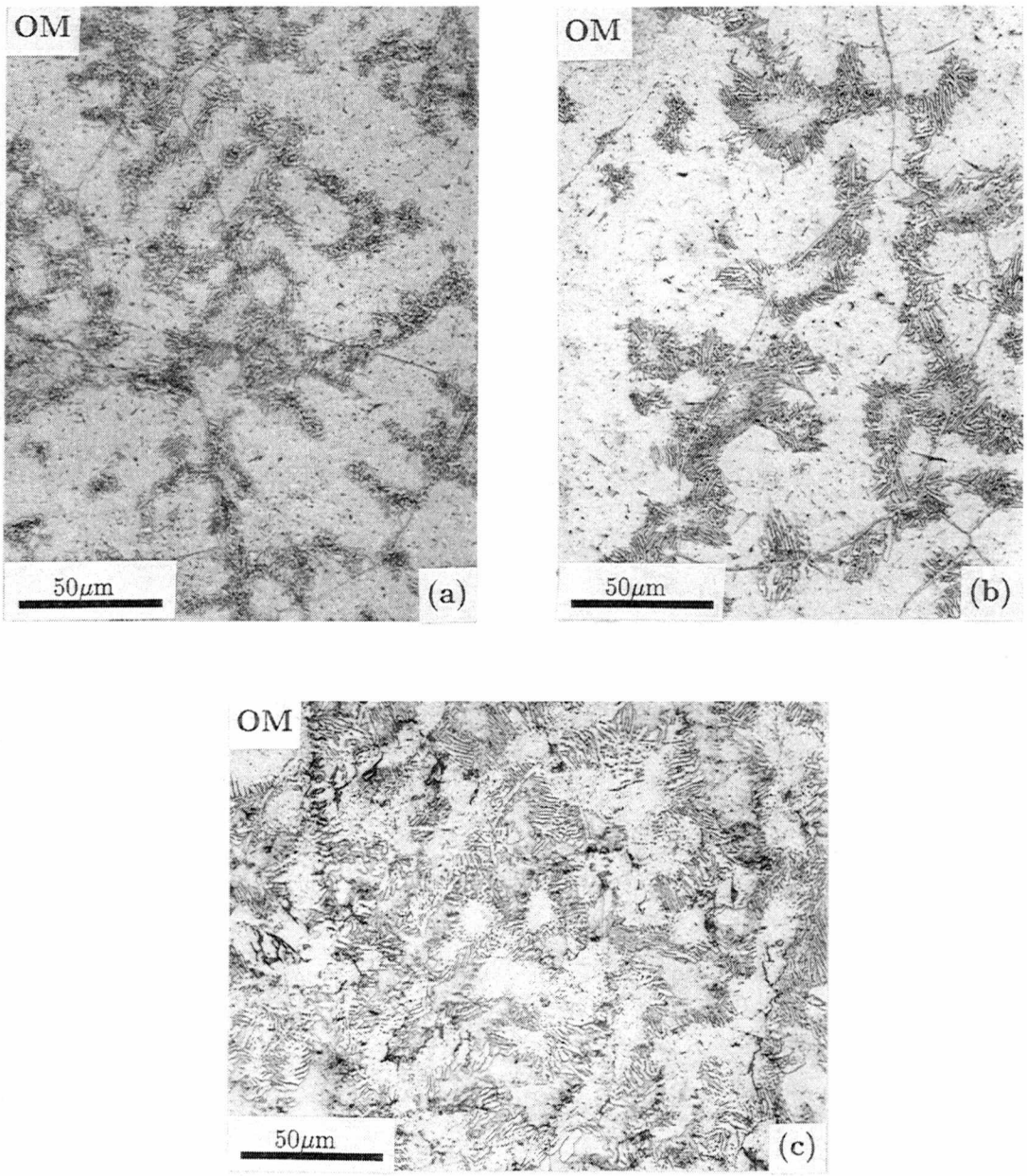



Figure 4.34: Microstructures of the Nb-15Al-10Ti alloy, heat-treated at 1173 K (900°C). (a) holding for 10 hours and as-heat-treated. (b) holding for 10 hours and tested. (c) holding for 100 hours and tested.

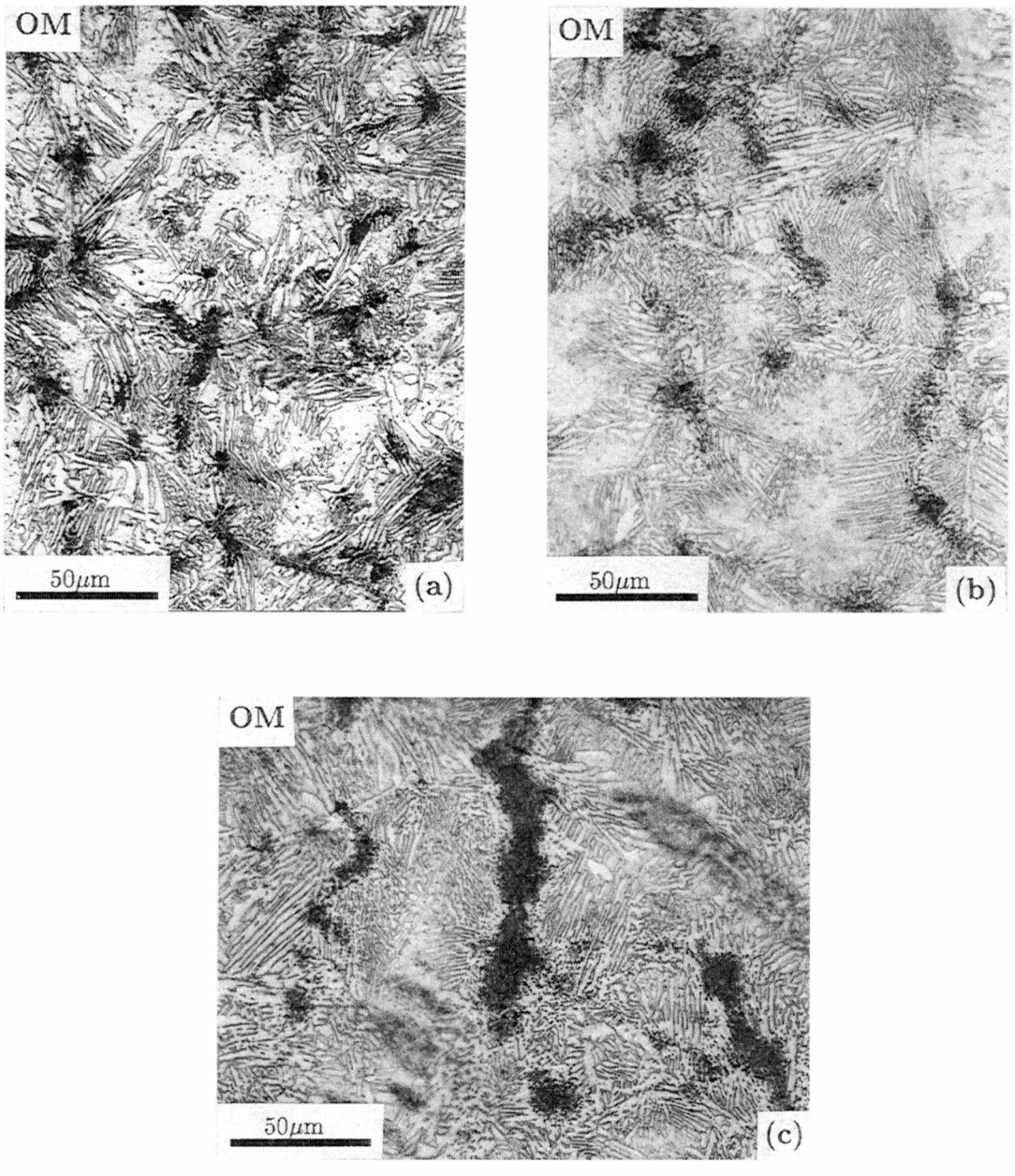



Figure 4.35: Microstructures of the Nb-15Al-25Ti alloy, heat-treated at 1173 K (900°C). (a) holding for 10 hours and as-heat-treated. (b) holding for 10 hours and tested. (c) holding for 100 hours and tested.

plates.

Micrographs of 40Ti alloy, heat-treated at 1173 K (900°C), are shown in Figure 4.36. (a) is holding for 10 hours and in as-heat-treated, while (b) is holding for 10 hours and tested. (c) is for 100 hours holding time and tested. Nb-rich particles were found in all samples. A fine needle-like structure was found in both tested samples.

A micrograph of 10Ti alloy, heat-treated at 1373 K (1100°C) for 10 hours and tested, is shown in Figure 4.37. Fine intergranular Widmanstätten plates are exhibited. Micrograph of 25Ti alloy, heat-treated at 1373 K (1100°C) for 10 hours and tested, is shown in Figure 4.38. Coarse Widmanstätten plates are exhibited. Micrograph of 40Ti alloy, heat-treated at 1373 K (1100°C) for 10 hours and tested. is shown in Figure 4.39. Nb-rich particles are exhibited.

In general, for the 10Ti and 25Ti alloys the amount of Widmanstätten plates increased with increasing heat treatment temperature and longer holding time. The morphology of intergranular Widmanstätten plates of 10Ti alloy is finer than that of 25Ti alloy. The grain size of the as-cast and heat-treated alloys is almost the same.

The microstructural characteristics of the as-cast and heat-treated alloys are summarized as follows: For the 10Ti alloy, Figure 4.24, 4.31, 4.34 and 4.37, the grain size is almost the same regardless of whether it is in the as-cast or heat-treated condition. When heat-treated at 873 K (600°C) or higher, the cored structure

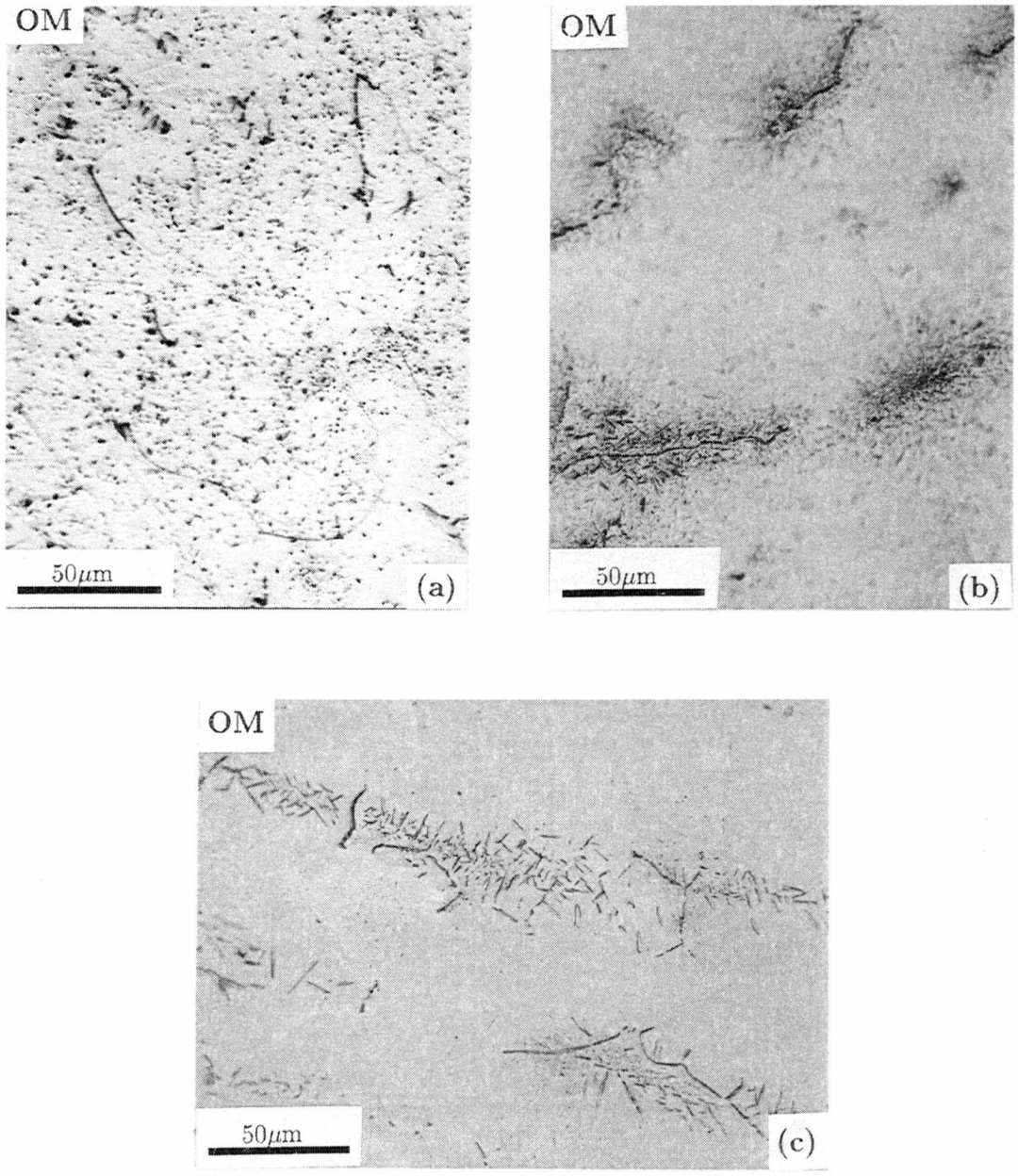



Figure 4.36: Microstructures of the Nb-15Al-40Ti alloy, heat-treated at 1173 K (900°C). (a) holding for 10 hours and as-heat-treated. (b) holding for 10 hours and tested. (c) holding for 100 hours and tested.

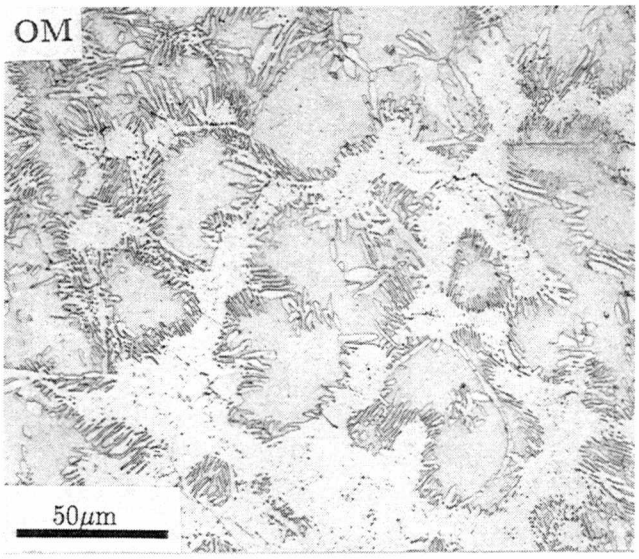



Figure 4.37: Microstructure of the tested Nb-15Al-10Ti alloy, heat-treated at 1373 K (1100°C) for 10 hours.

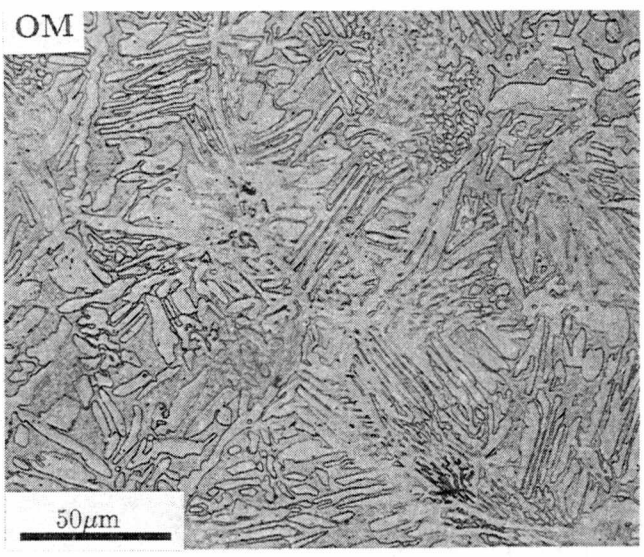



Figure 4.38: Microstructure of the tested Nb-15Al-25Ti alloy, heat-treated at 1373 K (1100°C) for 10 hours.

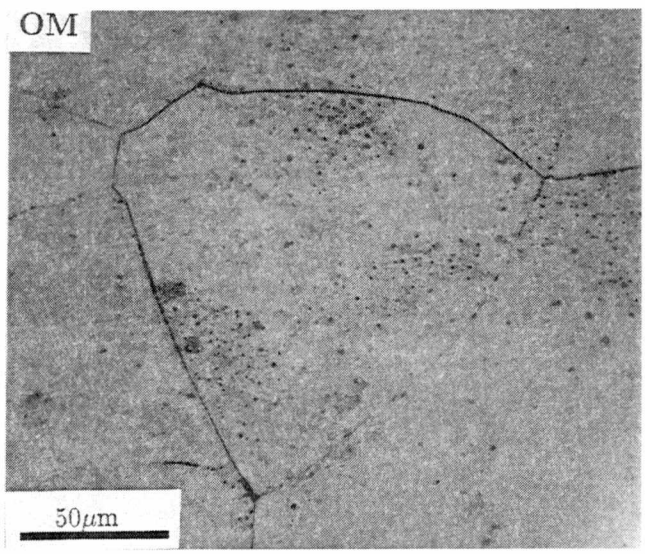



Figure 4.39: Microstructure of the tested Nb-15Al-40Ti alloy, heat-treated at 1373 K (1100°C) for 10 hours.

disappears, but the Nb-rich particles are clearly exhibited in all the samples. The $\delta$ phase formed during testing at 1173 K (900°C), but not during aging at 873 K (600°C). The Widmanstätten plates formed during testing at 1173 K (900°C) or heat treating at 1173 or 1373 K (900 or 1100°C).

For the 25Ti alloy, Figure 4.26, 4.32, 4.35 and 4.38, the cored structure still exists for heat treatment at 873 K (600°C) for 10 hours as in as-cast condition. Others do not show the cored structure. The grain size is almost the same for all the samples. The Widmanstätten plates formed during testing at 1173 K (900°C) along the grain boundaries, but not during aging at 873 K (600°C). The plates also formed during heat treatment at 1173 or 1373 K (900 or 1100°C).

For 40Ti alloy, the grain size is almost the same for all the samples. Other features appeared to be the same as for the as-cast condition, except for the samples heat-treated at 873 K (600°C) for both holding 10 and 100 hours which showed a fine line network.

Besides optical micrographs, typical SEM images are presented. Figure 4.40 is a SEM BSE micrograph of as-cast and tested 10Ti alloy. Figure 4.41 is a SEM micrograph of tested 40Ti alloy, heat-treated at 1173 K (900°C) for 100 hours. Both of the micrographs show cracks in the brittle $\delta$ phase. Typical EDS spectra obtained from a, in the grain boundary phase, and b, inside the grain, in Figure 4.41 are shown in Figure 4.42. The Nb to Ti ratio for a is 1.33 and for b is 1.24 which proves that the Nb content is higher along the grain boundary phase than inside

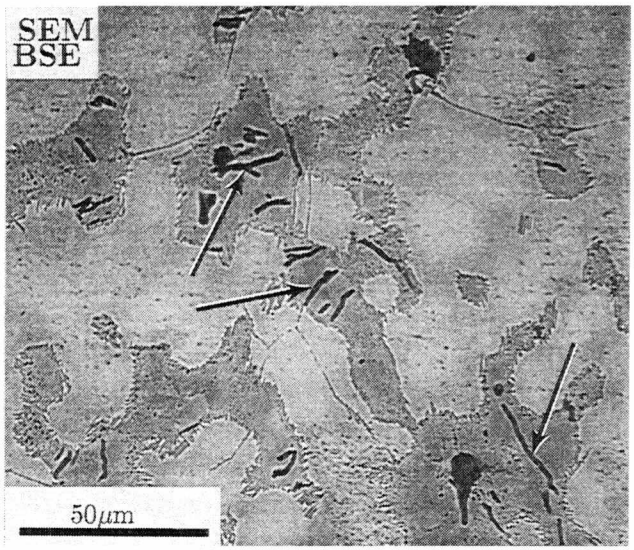



Figure 4.40: Microstructure of the as-cast Nb-15Al-10Ti alloy, tested at 900°C and strain rate of $10^{-4}$ $s^{-1}$, showing cracks (arrows) in $\delta$ phase.

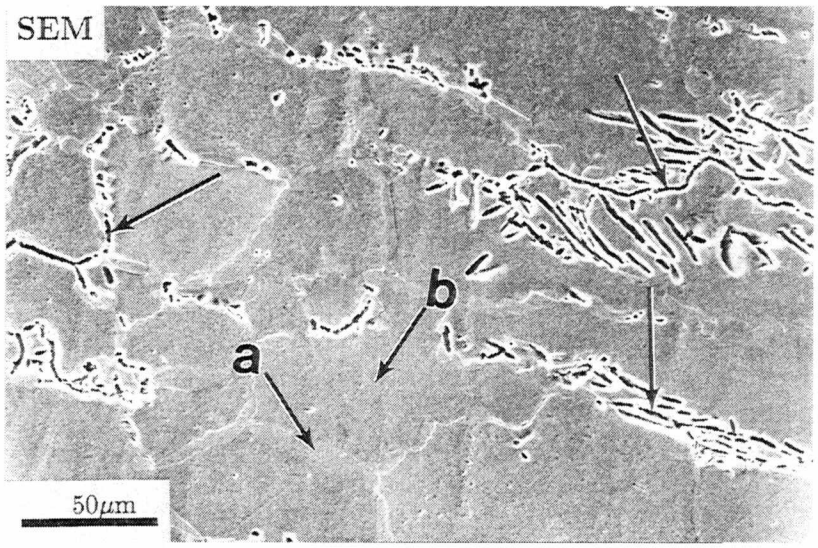



Figure 4.41: Microstructure of the tested Nb-15Al-40Ti alloy, heat-treated at 900°C for 100 hours, showing $\delta$ phase along the grain boundries and cracks (arrows) in $\delta$ phase.

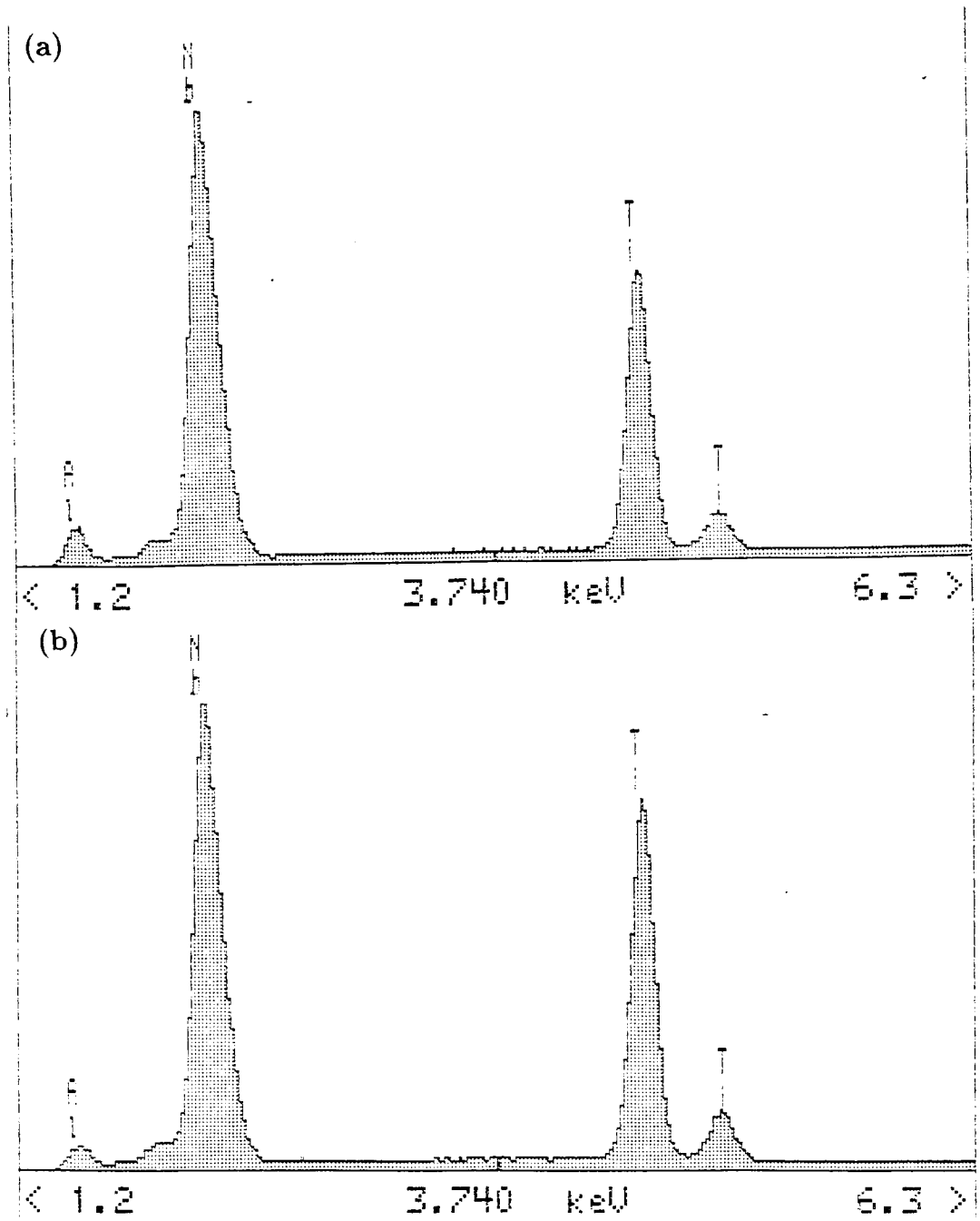



Figure 4.42: Typical EDS obtained from the Figure 4.41 (a) is a spectrum from $\delta$ phase along the grain boundaries. (b) is a spectrum from inside the grain. The ratio of Nb to Ti is 1.33 and 1.24 for (a) and (b), respectively.

the grain. It is assumed that this phase is $\delta$.

Typical structures of 25Ti alloy are shown in Figure 4.43. In the figure, (a) is as-heat-treated material, (b) is tested material. The morphology and the amount of the Nb-rich side-plates are almost the same. Figure 4.44 is a SEM micrograph of the TEM sample, tested 10Ti alloy heat-treated at 1273 K (900°C) for 10 hours, and shows the side-plates better. Holes are formed along the $\delta$ phase side-plates during thinning, which means the interface between the $\delta$ phase and B2 matrix is easy to etch.

In order to understand better the microstructure, TEM observations are necessary and important. Figure 4.45 is as-cast and tested 10Ti alloy which shows dislocation subgrain structure and its corresponding convergent beam electron diffraction (CBED) pattern showing 3mm symmetry of B2 structure taken from $<111>_{B2}$ zone axis. In general, the B2 structure has two significant features: one is superlattice spots in SAD taken from $<100>_{B2}$ or $<110>_{B2}$, the other is anti-phase domain boundaries (APB) in the dark-field image taken from superlattice spot. For example, Figures 4.46, 4.47, 4.48, 4.49, 4.50, 4.51, 4.52, 4.53, 4.54, 4.55, 4.56 and 4.57 present superlattice spots in SAD, and Figures 4.46, 4.52, 4.56 and 4.58 show anti-phase domain boundaries. The domain size for the 40Ti alloy is about 0.1 to 0.3 $\mu$m, and the size for 10Ti alloy is about 0.05 to 0.1 $\mu$m.

Figure 4.45 is the bright-field image of the as-cast and tested 10Ti alloy showing subgrain structure which is the evidence of dynamic recrystallization, a yield drop

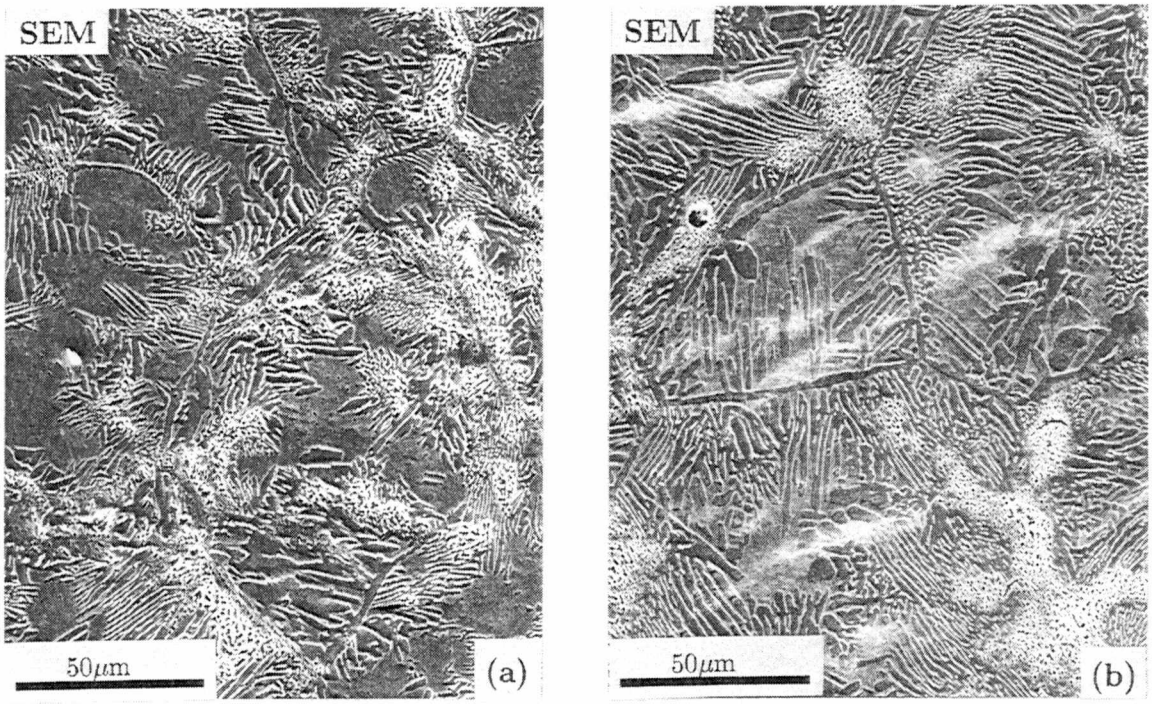



Figure 4.43: Microstructure of the tested Nb-15Al-25Ti alloys, heat-treated at 900°C for 10 hours. (a) as-heat-treated material. (b) tested material. Note the morphology and the volume fraction of $\delta$ phase are almost the same.

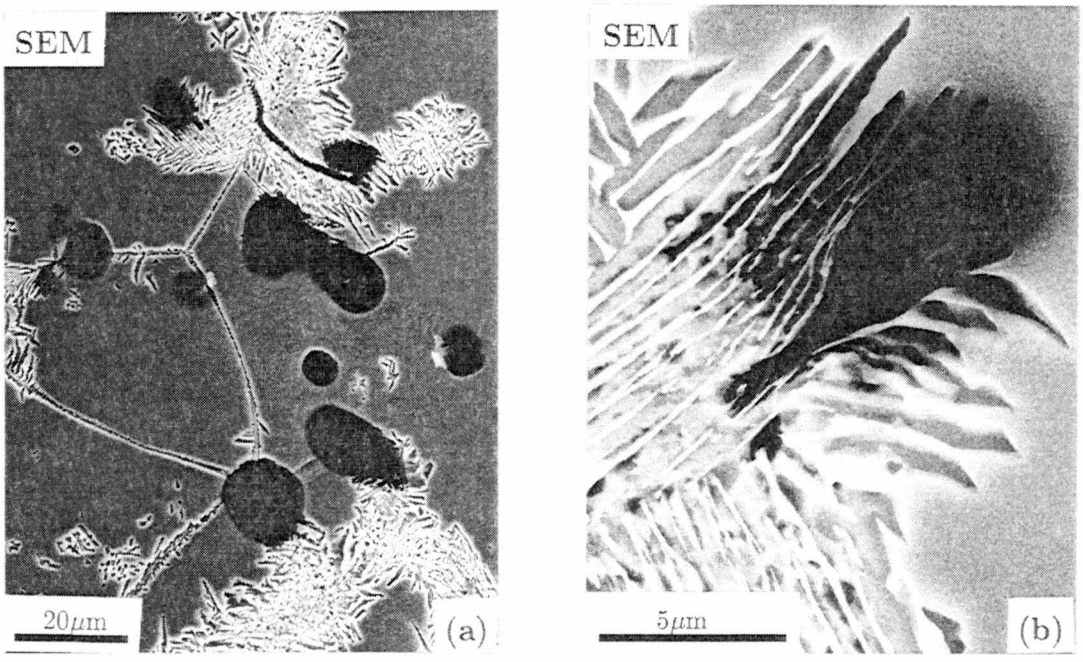



Figure 4.44: SEM images taken from TEM sample of the tested Nb-15Al-10Ti alloy, heat-treated at 900°C for 10 hours. (a) the holes are along or in the $\delta$ phase. (b) close-up the hole shows side-plates. The etching solution was 10 vol.% $H_2SO_4$ in methanol.

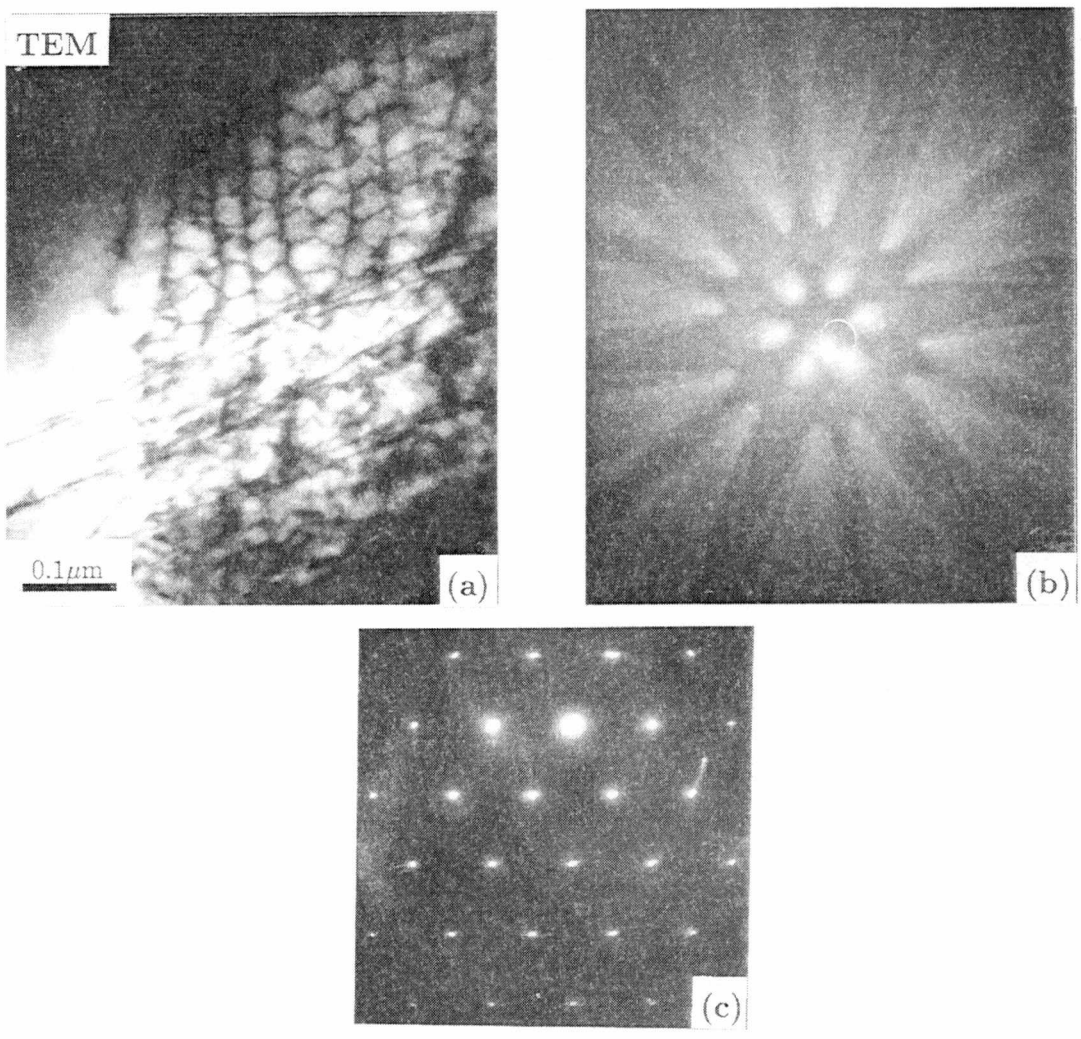



Figure 4.45: Microstructure of as-cast and tested Nb-15Al-10Ti alloy. (a) bright-field image showing subgrain structure. (b) corresponding CBED taken from $<111>_{B2}$ zone axis. (c) corresponding SAD taken from $<111>_{B2}$ zone axis.

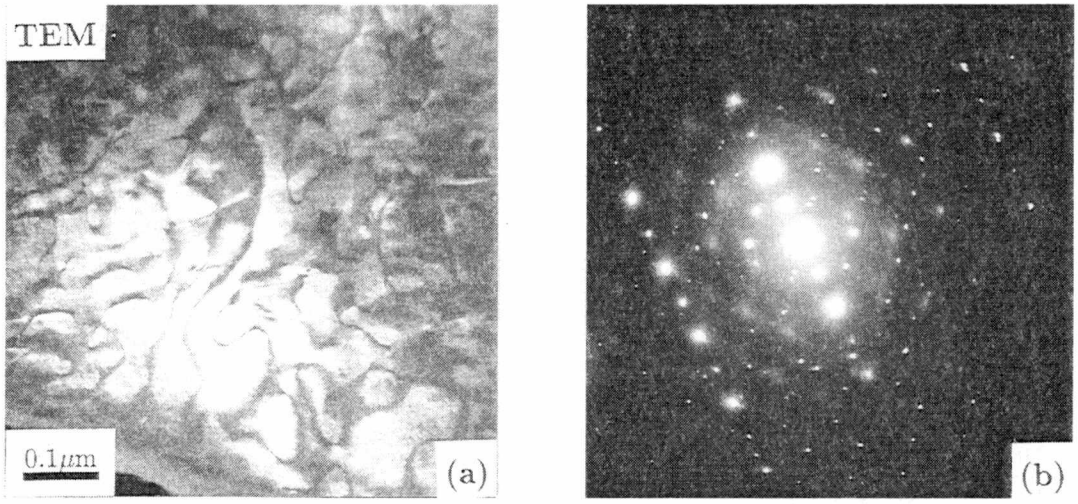



Figure 4.46: Microstructure of the tested Nb-15Al-10Ti alloy, heat-treated at 600°C for 10 hours. (a) dark-field image showing anti-phase boundaries. (b) corresponding SAD taken from $<110>_{B2}$ zone axis and streaks which may be caused by $\omega$ phase.

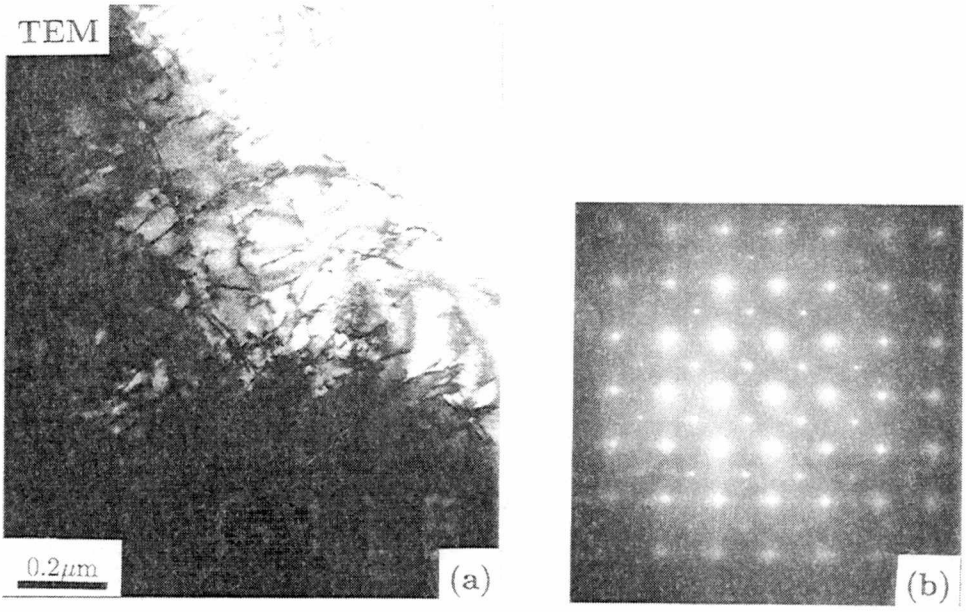



Figure 4.47: Microstructure of the tested Nb-15Al-10Ti alloy, heat-treated at 600°C for 100 hours. (a) bright-field image showing dislocation dipoles. (b) corresponding SAD taken from $<100>_{B2}$ zone axis showing superlattice spots.

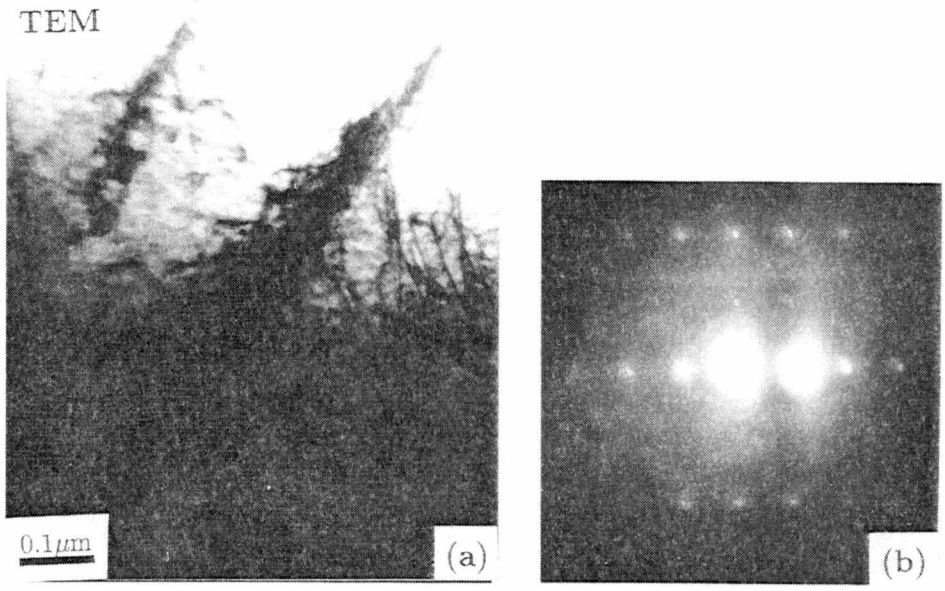



Figure 4.48: Microstructure of the as-cast and tested Nb-15Al-25Ti alloys. (a) bright-field image showing periodic parallel tangled dislocations. (b) corresponding SAD taken from $<110>_{B2}$ zone axis.

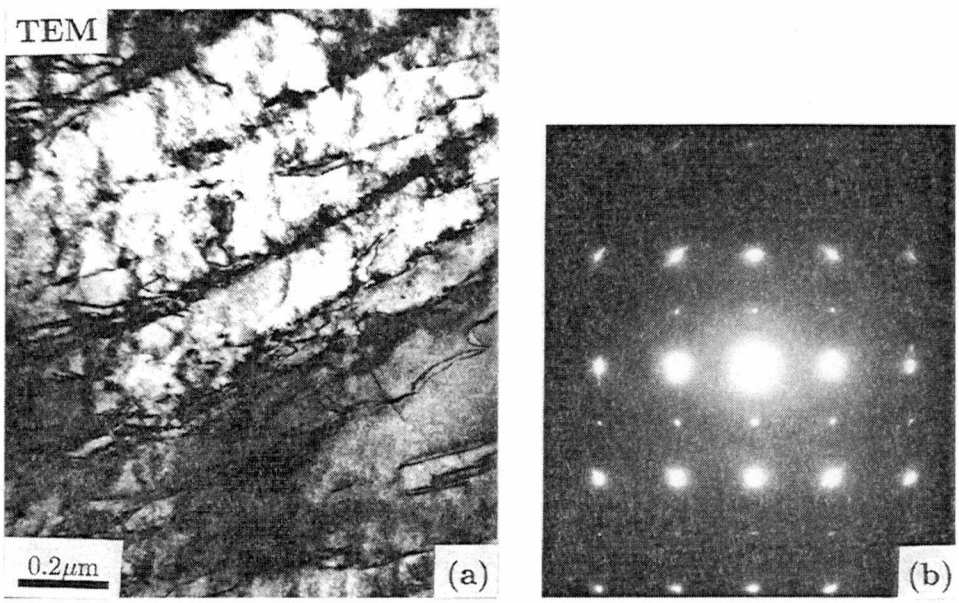



Figure 4.49: Microstructure of the as-cast and tested Nb-15Al-25Ti alloys. (a) bright-field image showing dislocation bands. (b) corresponding SAD taken from $<110>_{B2}$ zone axis.

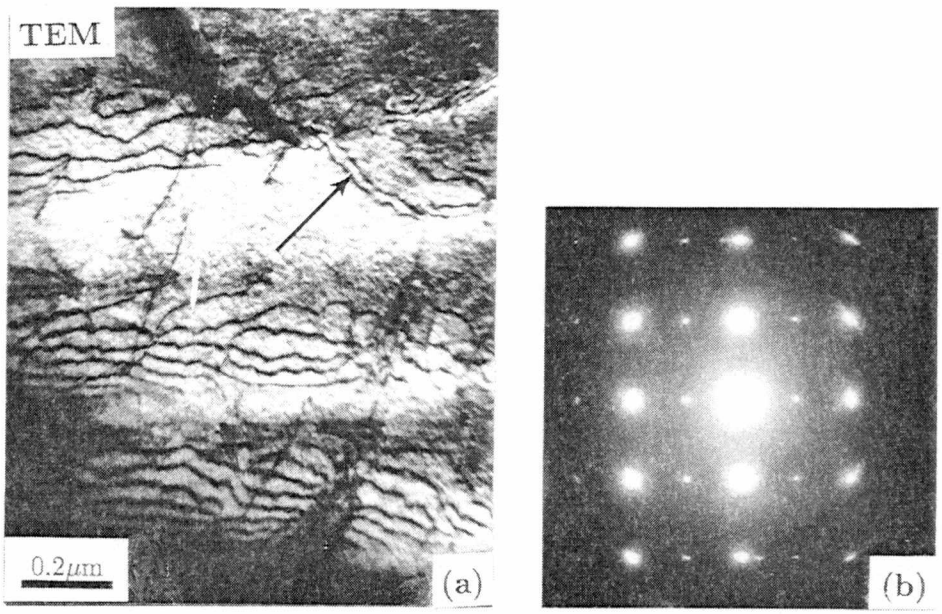



Figure 4.50: Microstructure of the as-cast and tested Nb-15Al-25Ti alloys. (a) bright-field image showing the periodic dislocation bands and dipoles. (b) corresponding SAD taken from $<110>_{B2}$ zone axis.

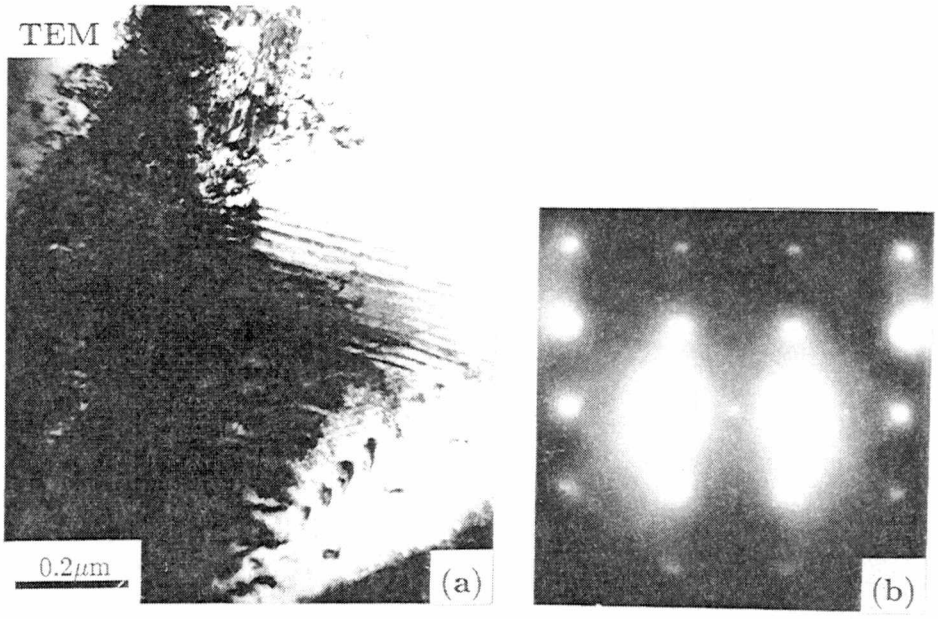



Figure 4.51: Microstructure of the tested Nb-15Al-40Ti alloy, heat-treated at 600°C for 10 hours. (a) bright-field image showing periodic dislocations line-up. (b) corresponding SAD taken from $<110>_{B2}$ zone axis.

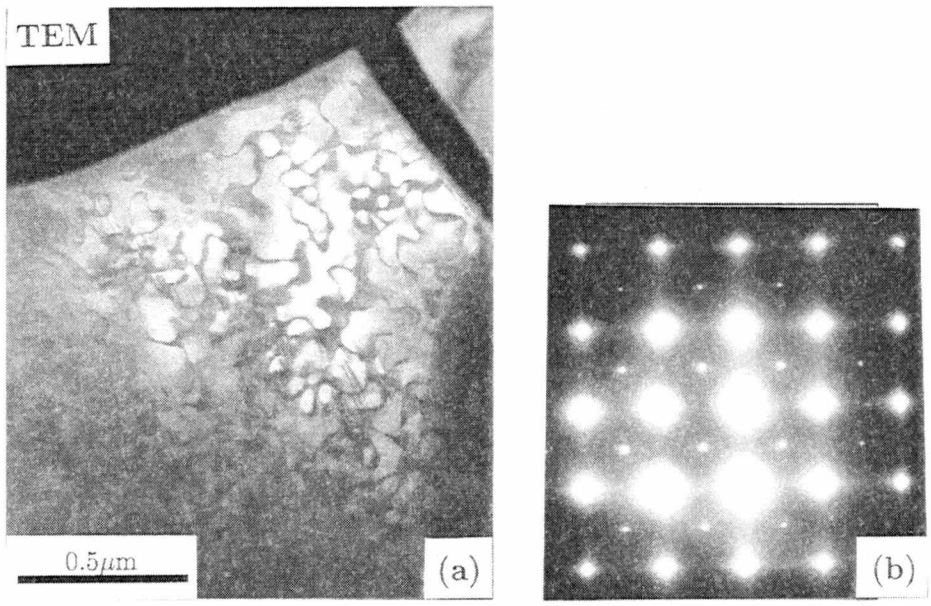



Figure 4.52: Microstructure of the tested Nb-15Al-40Ti alloy, heat-treated at 600°C for 100 hours, (a) dark-field image showing anti-phase boundaries. (b) corresponding SAD taken from $<100>_{B2}$ zone axis.

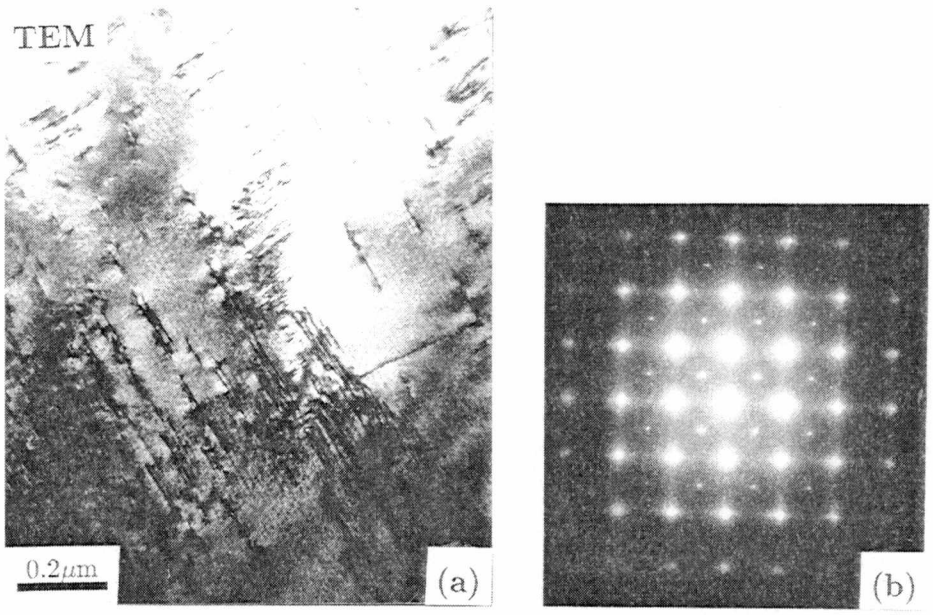



Figure 4.53: Microstructure of the tested Nb-15Al-40Ti alloy, heat-treated at 1100°C for 10 hours. (a) bright-field image showing dislocation dipoles in B2 matrix. (b) corresponding SAD taken from $<100>_{B2}$ zone axis.

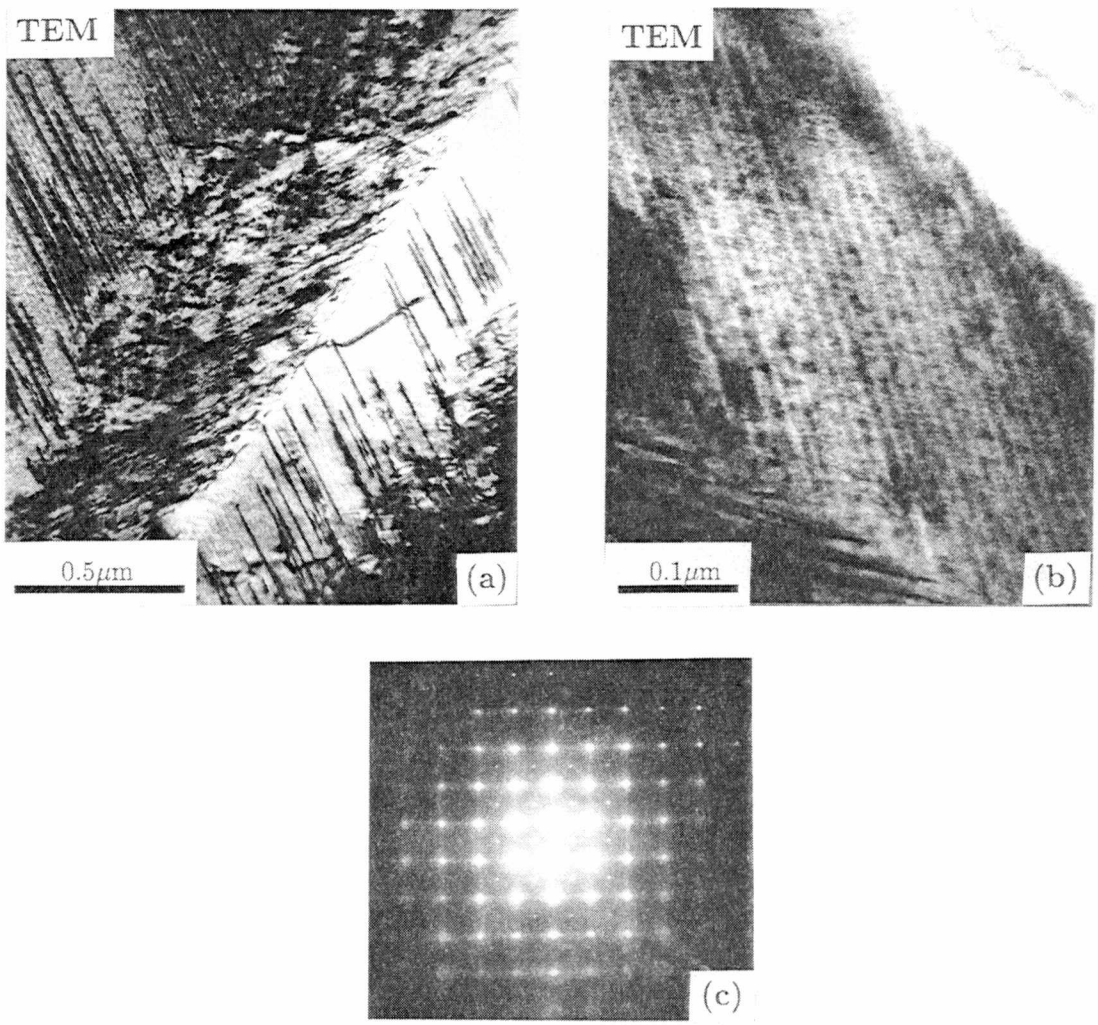



Figure 4.54: Microstructure of the tested Nb-15Al-40Ti alloy, heat-treated at 1100°C for 10 hours. (a) bright-field image showing parallel dislocations. (b) close-up of the B2 matrix showing parallel strip structure. (c) corresponding SAD taken from $<100>_{B2}$ zone axis.

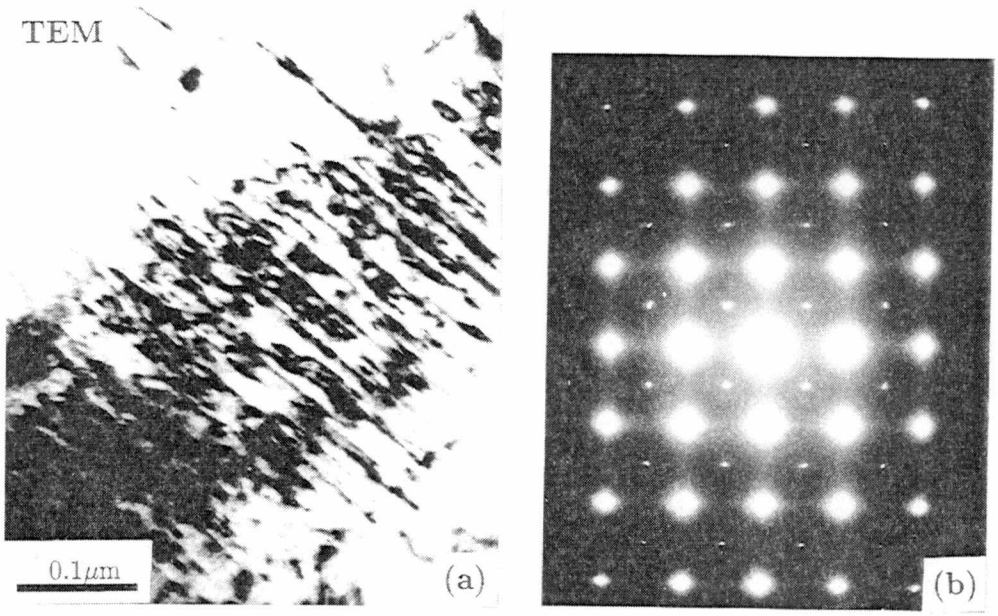



Figure 4.55: Microstructure of the tested Nb-15Al-40Ti alloy, heat-treated at 1100°C for 10 hours. (a) bright-field image showing dislocation dipoles in the slip band. (b) corresponding SAD taken from $<100>_{B2}$ zone axis.

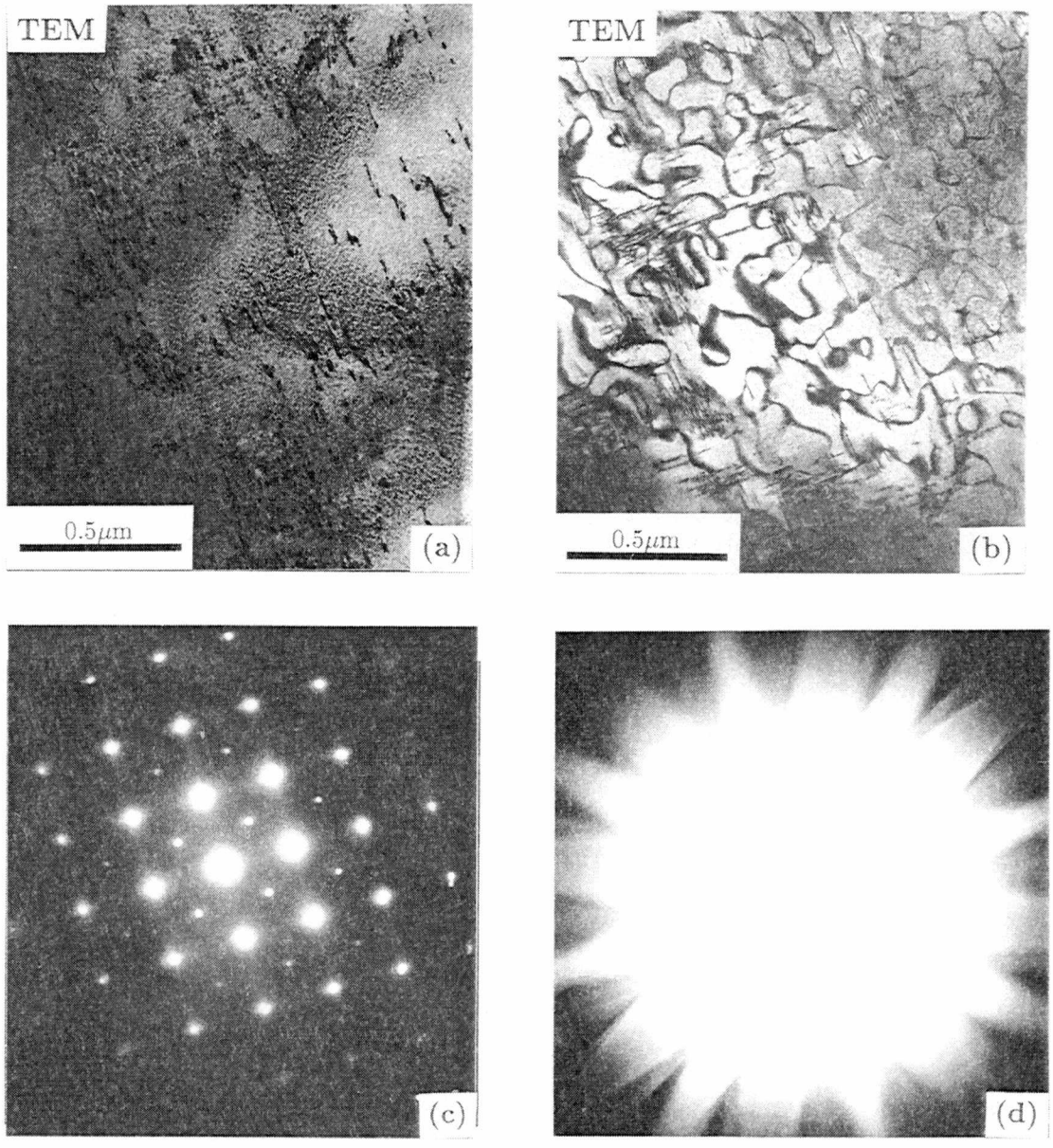



Figure 4.56: Microstructure of the tested Nb-15Al-40Ti alloy, heat-treated at 1100°C for 10 hours. (a) bright-fielf image. (b) corresponding dark-field image showing anti-phase boundaries. (c) corresponding SAD taken from $<100>_{B2}$ zone axis. (d) corresponding CBED taken from $<100>_{B2}$ zone axis.

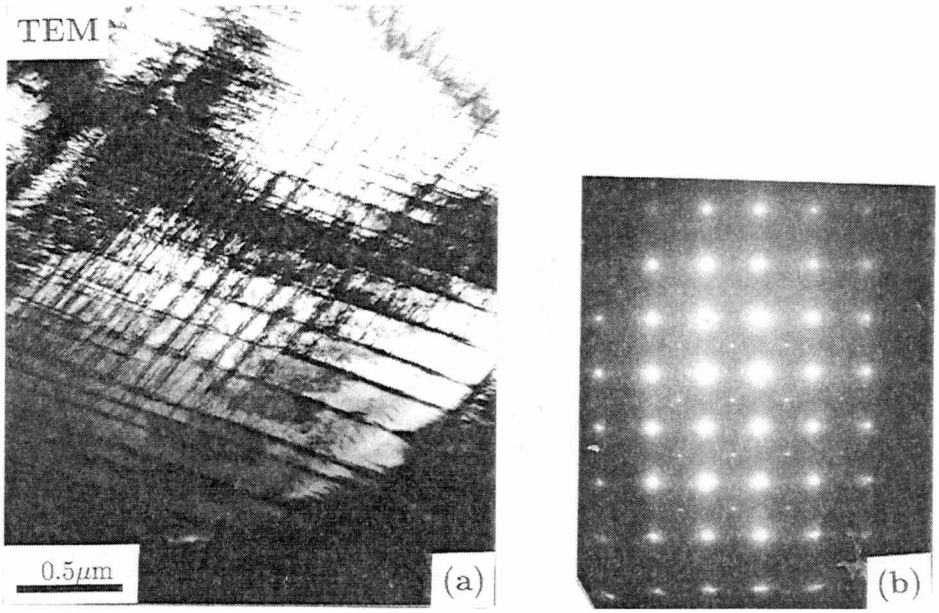



Figure 4.57: Microstructure of the tested Nb-15Al-40Ti alloy, heat-treated at 1100°C for 10 hours. (a) bright-field image showing dislocation intersecting bands. (b) corresponding SAD taken from $<100>_{B2}$ zone axis.

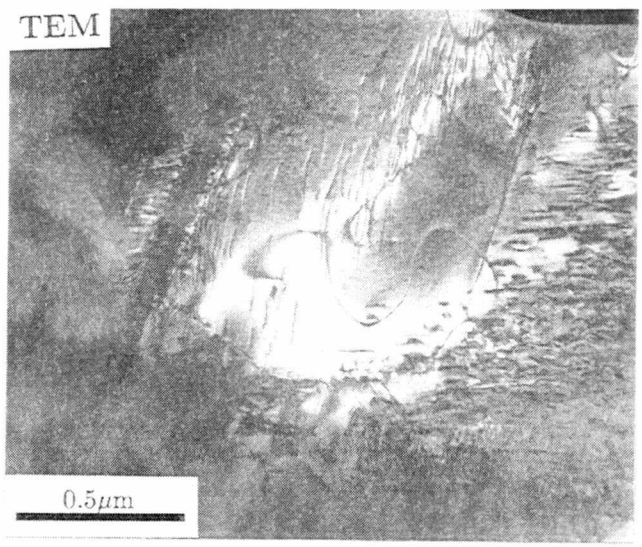



Figure 4.58: Dark-field image of the as-cast and tested Nb-15Al-40Ti alloy showing anti-phase boundaries and dislocations taken from $<110>_{B2}$ zone axis. Note dislocations pass through the anti-phase boundaries.

mechanism.

Figure 4.46 is the dark-field image of the tested 10Ti alloy, heat-treated at 873 K (600°) for 10 hours, showing APB. Its corresponding SAD shows streaks which may be caused by $\omega$ phase [77], too fine to resolve.

Figure 4.54 is the microstructure of the tested 40Ti alloy, heat-treated at 1373 K (1100°C) for 10 hours. Parallel dislocations are shown in (a). A high magnification image of the matrix shows a parallel strip structure, shown in (b), which exhibits the B2 structure, shown in (c), as well as streaks in SAD.

Figure 4.55 is the bright-field image of the tested 10Ti alloy, heat-treated at 1373 K (1100°C) for 10 hours, showing a group of dislocation dipoles in the slip band taken from $<100>_{B2}$ zone axis.

Figure 4.57, the tested 40Ti alloy, heat-treated at 1373 K (1100°C) for 10 hours, and Figure 4.59, the tested 10Ti alloy, heat-treated at 1173 K (900°C) for 100 hours, show intersecting dislocation bands.

The A15 ($\delta$) phase is commonly found in 10Ti and 25Ti aged alloys; an example is shown in Figure 4.60. Its corresponding CBED, showing 2mm symmetry, and its SAD are shown in figure (b) and (c), respectively, both taken from $<100>_{A15}$ zone axis. From the SAD pattern, the A15 phase lattice parameter was calculated and agrees with Lundin's and Zdziobek's results [40, 61]. In addition to the A15 phase, the $o$ phase can also be found in 10Ti and 25Ti aged alloys, e.g., Figure 4.61 and 4.62. The corresponding CBEDs are shown in Figure 4.61(b) and 4.62(b) taken

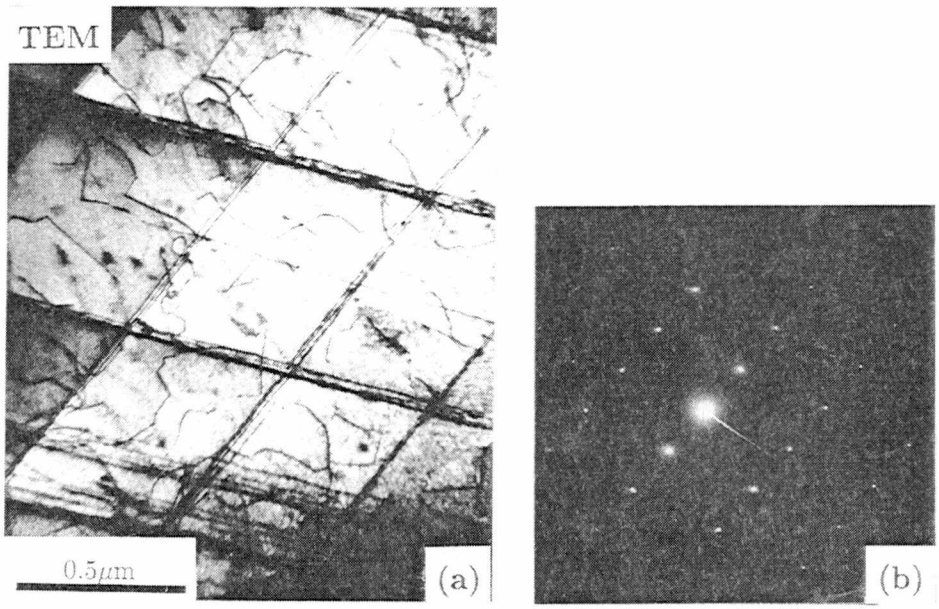



Figure 4.59: Microstructure of the tested Nb-15Al-10Ti alloy, heat-treated at 900°C for 100 hours. (a) bright-field image showing dislocation intersecting bands and single dislocations distribute in the matrix. (b) corresponding SAD taken from $<\bar{1}13>_{B2}$ zone axis.

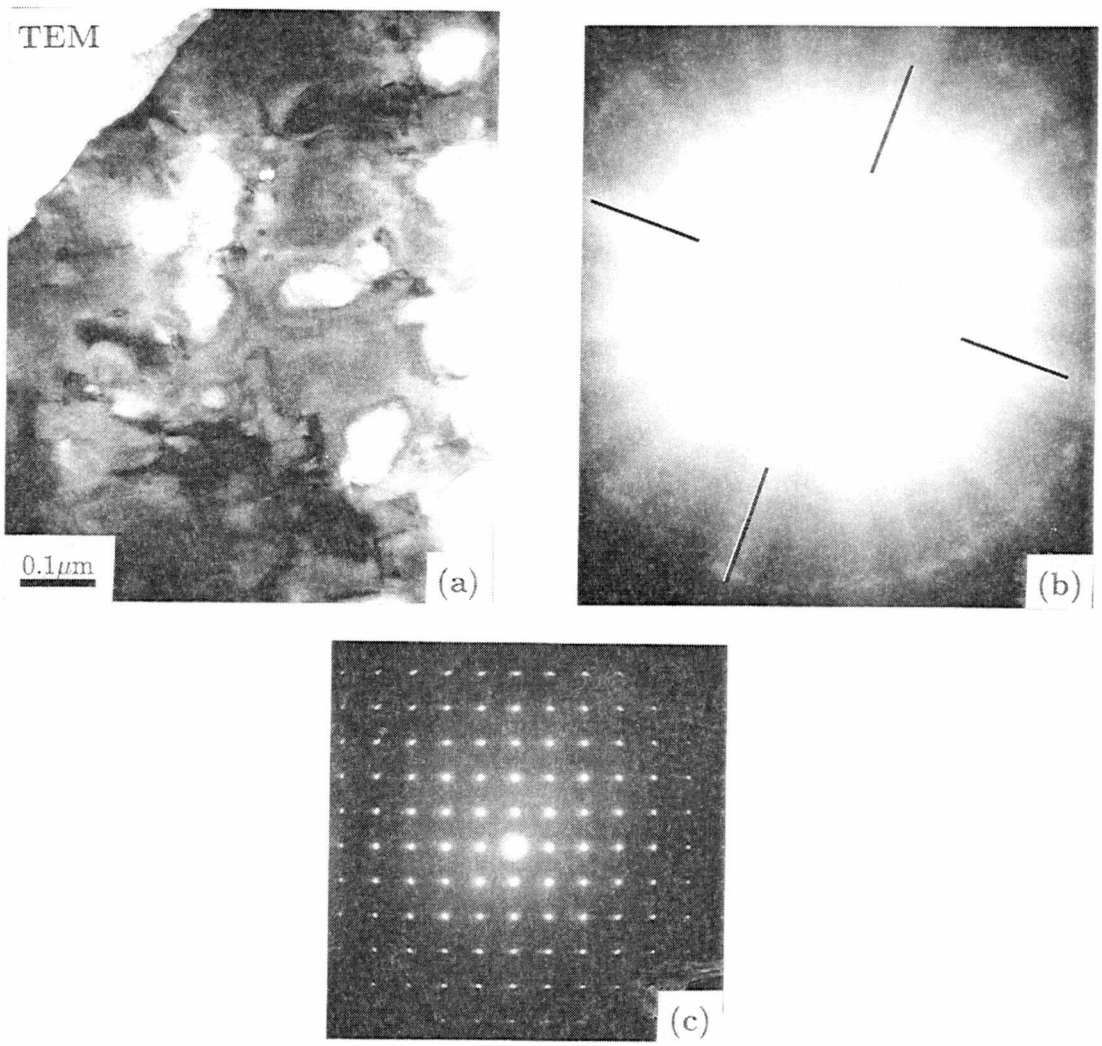



Figure 4.60: Microstructure of the tested Nb-15Al-10Ti alloy, heat-treated at 600°C for 100 hours. (a) bright-field image showing $\delta$ phase. (b) corresponding CBED whole patterns with $<100>_{A15}$ zone axis showing 2mm symmetry. (c) corresponding SAD taken from $<100>_{A15}$ zone axis.

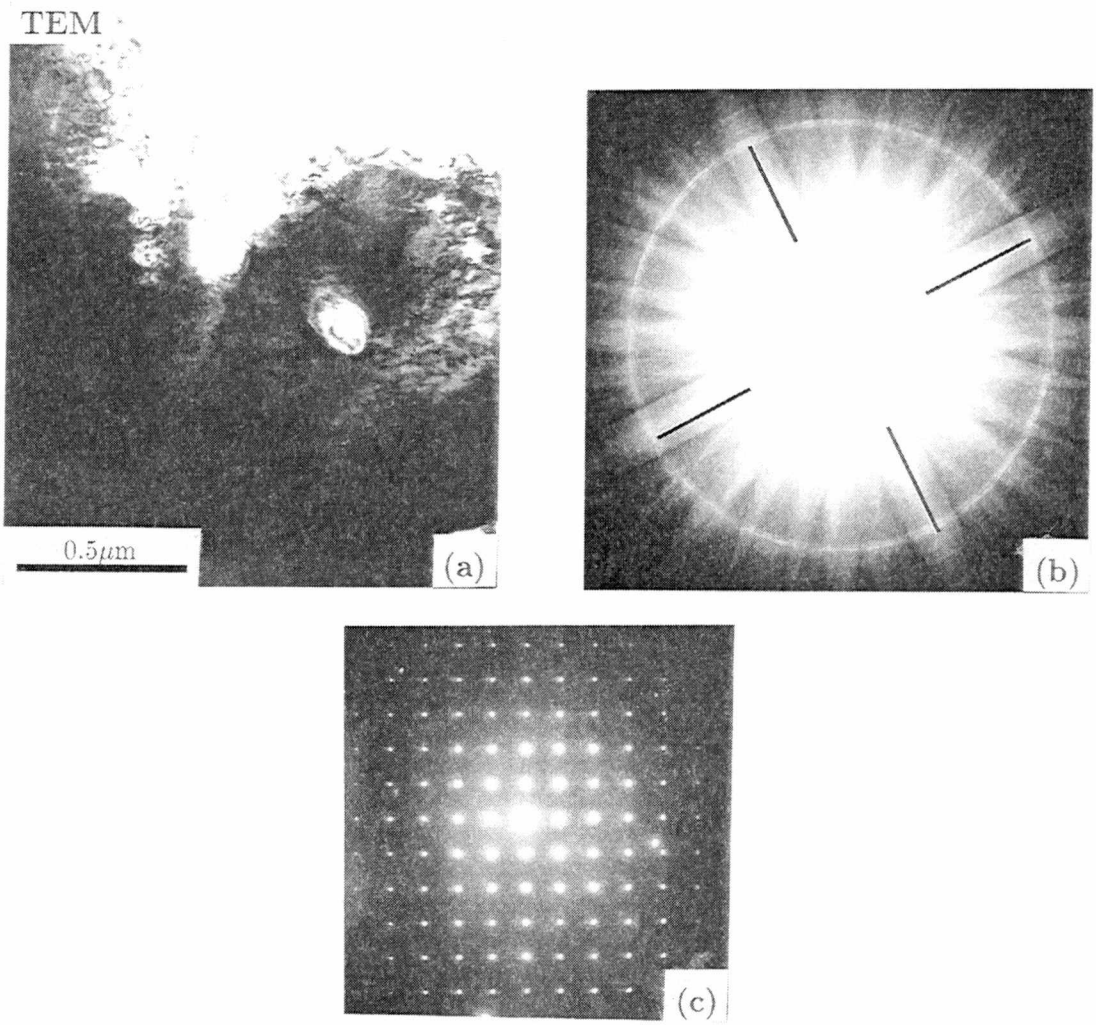



Figure 4.61: Microstructure of the tested Nb-15Al-25Ti alloys, heat-treated at 1100°C for 10 hours. (a) bright-field image showing $o$ phase in the B2 matrix. (b) corresponding CBED of $o$ phase taken from $<100>_o$ zone axis. (c) corresponding SAD of $o$ phase taken from $<100>_o$ zone axis.

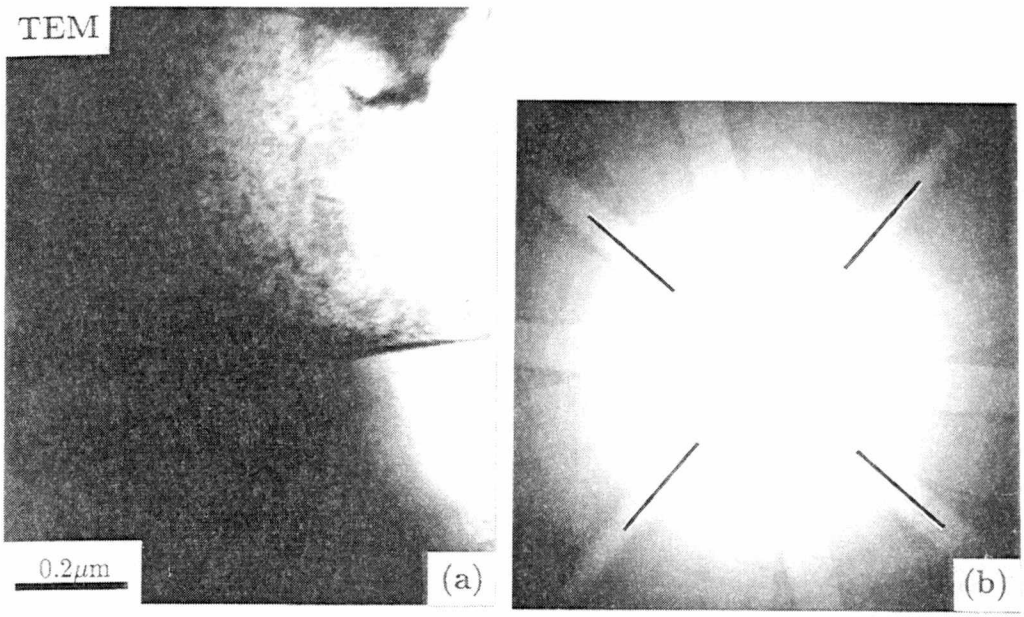



Figure 4.62: Microstructure of the tested Nb-15Al-40Ti alloy, heat-treated at 900°C for 10 hours. (a) bright-field image showing $o$ phase. (b) corresponding CBED taken from $<001>_o$ zone axis.

from $<100>_o$ and $<001>_o$, respectively, which agree with Banerjee's and Hsiung's results [62, 83].

## 4.10 Dislocation Morphology

The dislocation morphology of the alloys can be divided into six types: First type, dislocation dipoles, e.g., Figure 4.47, 4.49, 4.50, 4.53, 4.54 and 4.55; Second type, periodic parallel and tangled dislocations in the slip bands, e.g., Figure 4.48, 4.49, 4.51 and 4.63; Third type, intersecting dislocation bands, e.g., Figure 4.57 and 4.59; Fourth type, dislocation subgrain structure, e.g., Figure 4.45; Fifth type, long dislocations in matrix, e.g., Figure 4.50 and 4.64; Sixth type, single dislocations in matrix, e.g., Figure 4.53 and 4.59. Both anti-phase domain boundaries and dislocations can be seen in Figure 4.58 and dislocations cross the domain boundaries. Shyue *et al.* [20] also showed the first, second, fifth and sixth types of dislocation morphology.

Dislocation dipoles were found in every tested alloy, as-cast and heat-treated. The fifth and sixth types of dislocations were also found in each tested alloy. But the second type, periodic parallel and tangled dislocations, were only found in as-cast alloys or those heat-treated at 873 K (600°C), and their corresponding compression strengths were lower than alloys containing the third type, dislocations in slip bands which are intersected, found in alloys tested at 1173 and 1373 K (900 and 1100°C). As for the yield drop behavior, group (iii) behavior of stress-strain

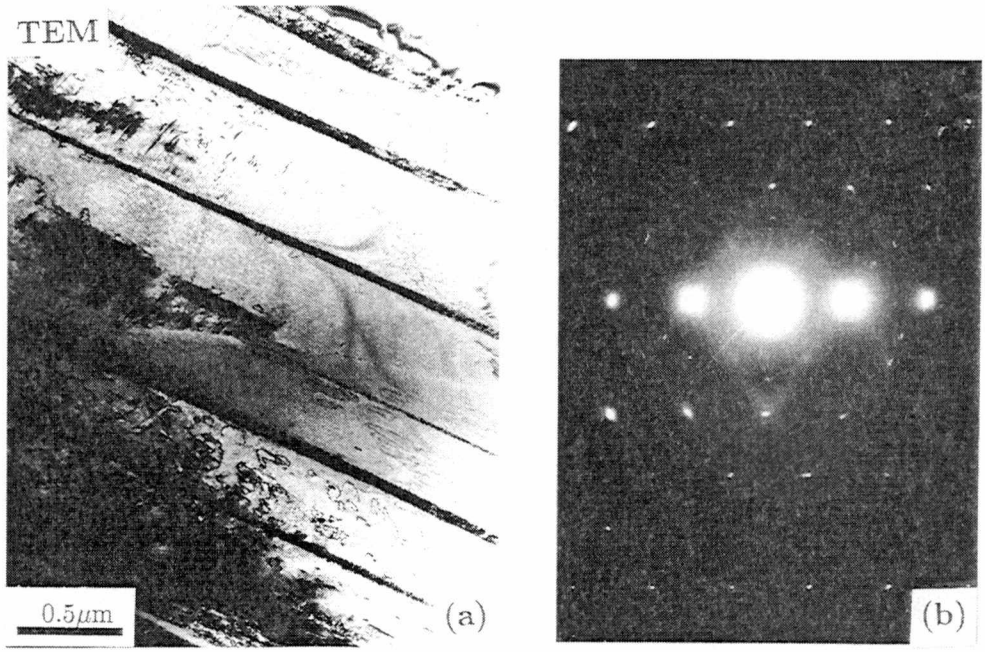



Figure 4.63: Microstructure of the tested Nb-15Al-40Ti alloy, heat-treated at 1100°C for 10 hours. (a) bright-field image showing dislocations in the slip bands. (b) corresponding SAD taken from $<110>_{B2}$ zone axis.

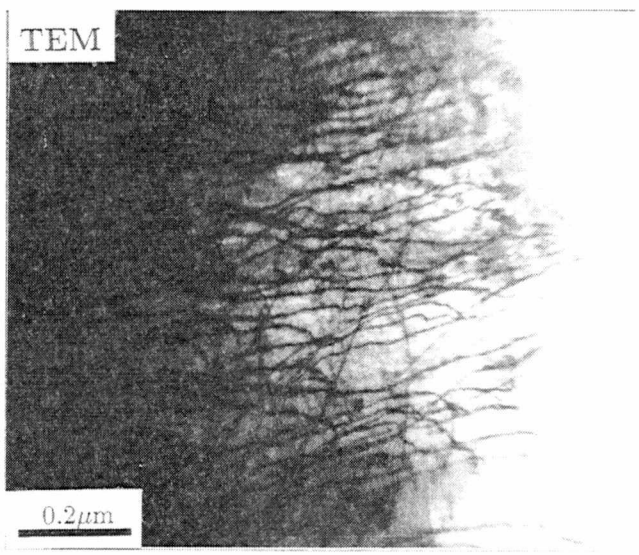



Figure 4.64: Bright-field image of the tested Nb-15Al-10Ti alloy, heat-treated at 900°C for 100 hours, showing long dislocations tangled structure taken from $<111>_{B2}$ zone axis.

curves, its mechanism is dynamic recrystallization, see section 4.3. One evidence of dynamic recrystallization is the subgrain structure, shown in Figure 4.45, formed during testing. The subgrain structure is also exhibited in 40Ti alloy.

# CHAPTER V

# DISCUSSION OF RESULTS

## 5.1 Microstructure and Mechanical Properties of As-Cast Alloys

### 5.1.1 Microstructure of As-Cast Alloys

Table 5.1 summarizes the microstructure of the as-cast alloys. In all cases, transmission electron microscopy revealed that the matrix had the B2 structure, although streaking between spots, especially evident in the <100> patterns, was frequently found. Its origin was not established. The grain boundary phase and the Widmanstätten phase were relatively rich in Nb, and both were assumed to be the $\delta$ phase. Difficulty in preparing transmission electron microscopy samples with regions sufficiently thin to be examined precluded confirming clearly that this was the $\delta$ phase. However, it was identified in some of the samples. The 'Nb-rich particles' which speckled the optical micrographs were present in most samples, but were not identified. They did not appear to change significantly during testing or heat treatment. These particles probably do not affect the strength as their amount is very low and remains about the same, or changes do not correlate with strength changes.

The 10Ti and 25Ti alloys of Group II showed prominent coring, whereas none

Table 5.1: Summary of Microstructures of As-Cast Alloys and of alloys after testing at 900°C at a strain rate of $10^{-4}$ $s^{-1}$. The structure after testing is shown in brackets. The time to heat to 900°C and make the test was about 15 minutes.

| | |
|---|---|
| Group I | |
| 10Ti | B2 matrix, grain boundary $\delta$, Widmanstätten side-plates of $\delta$, no coring |
| | [Same as as-cast, but slight additional growth of $\delta$ side-plates] |
| 25Ti | Single phase B2, no coring |
| | [Same as as-cast] |
| 40Ti | Single phase B2, no coring |
| | [Same as as-cast] |
| Group II | |
| 10Ti | Single phase B2, cored |
| | [B2 matrix, Widmanstätten side-plates of $\delta$, no coring] |
| 25Ti | Single phase B2, cored |
| | [B2 matrix, Widmanstätten side-plates of $\delta$, no coring] |
| 40Ti | Single phase B2, no coring |
| | [Same as as-cast] |

of the alloys of Group I showed coring. The two groups were prepared by different methods (see Section 3.1), and apparently those of Group I cooled sufficiently slowly during solidification to eliminate coring.

The grain size of Group I alloys was approximately 300 $\mu$m and that of Group II alloys was approximately 100 $\mu$m.

### 5.1.2 Microstructure of As-Cast Alloys after Testing at 900°C

The microstructures of the alloys after testing at 1173 K (900°C) at a strain rate of $10^{-4}$ $s^{-1}$ are also listed in brackets in Table 5.1. At this test temperature and strain rate, about 15 minutes was required to heat the sample to the test temperature and complete the test. There was evidence that a small amount of additional Widmanstätten $\delta$ formed during testing. There was no obvious change in the grain size of any alloys in either group. The main alteration in the microstructures was the removal of coring present in the as-cast structure.

### 5.1.3 Yield Strength of As-Cast Material at 900°C

The yield strength at 1173 K (900°C) of the as-cast material for both alloy groups is shown in Figure 5.1. For both groups, the strength decreases with increasing Ti content, that is, increases with increasing Nb content. The as-cast structure of the alloys was single phase B2, with the exception of the 10Ti alloy of Group I, which contained some $\delta$. However, after testing the 10Ti and 25Ti alloys of Group II showed some $\delta$ which formed during testing. The presence of $\delta$ in the as-cast

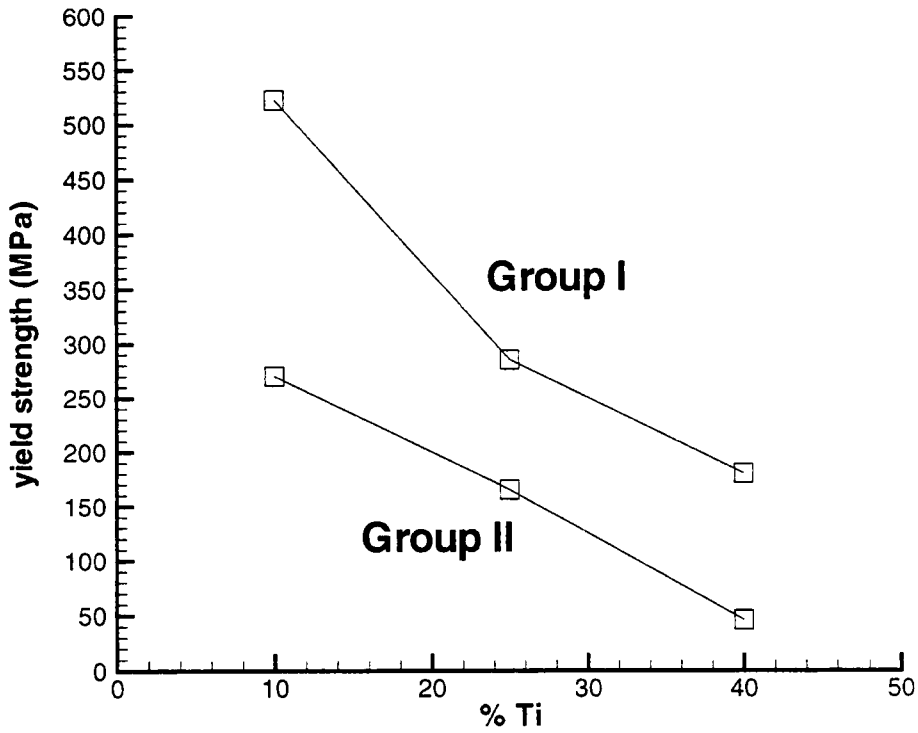



Figure 5.1: Compressive yield strength versus Ti content for as-cast samples tested at 900°C at a strain rate of $10^{-4}$ $s^{-1}$.

condition could contribute to a higher strength, and its formation during testing could increases the strength. There probably is also significant solid solution strengthening of B2 phase from the Nb.

The origin of the differences in the strength of the two Groups is puzzling. Group I alloy had the coarser grains, yet the higher strength. The chemical analysis of Group II alloys indicates quite high purity (Table 3.1). However, no chemical analysis was available for Group I alloys, so it is not known whether the difference in strength is due to purity differences.

All of the as-cast alloys tested at 1173 K (900°C) at a strain rate of $10^{-4}$ $s^{-1}$ showed the yield drop effect. This effect occurred in alloys which remained single phase B2 during testing and in those which had $\delta$ present prior to testing and in which $\delta$ formed during testing. Thus the yield drop cannot be due to the formation of $\delta$ during testing.

## 5.2 Microstructure and Mechanical Properties of Heat Treated Alloys

### 5.2.1 Microstructure of Heat Treated Alloys

The microstructures of the heat treated alloys are summarized in Table 5.2. For comparison, those of the as-cast structure is listed. For the 10Ti alloy, 10 hours at 873 K (600°C) removed the coring. After aging 100 hours, $\delta$ appeared. Aging at 1173 K (900°C) and 1373 K (1100°C) removed coring and produced Widmanstätten $\delta$.

Table 5.2: Microstructure of heat treated and tested alloys. The structure after testing at 900°C at a strain rate of $10^{-4}$ $s^{-1}$ is shown in brackets.

| | |
|---|---|
| **10Ti Alloy** | |
| As-cast | Single phase B2, cored |
| | [B2 matrix, Widmanstätten $\delta$, no coring] |
| 600°C, 10 h | Single phase B2, no coring |
| | [B2 matrix, Widmanstätten $\delta$] |
| 600°C, 100 h | Single phase B2, no coring |
| | [B2 matrix, Widmanstätten $\delta$] |
| 900°C, 10 h | B2 matrix, Widmanstätten $\delta$, no coring |
| | [Same as heat treated] |
| 900°C, 100 h | No sample available; probably same as tested sample |
| | [B2 matrix, Widmanstätten $\delta$, no coring] |
| 1100°C, 10 h | No sample available; probably same as tested sample |
| | [B2 matrix, Widmanstätten $\delta$, no coring] |
| **25Ti Alloy** | |
| As-cast | Single phase B2, cored |
| | [B2 matrix, grain boundary $\delta$] |
| 600°C, 10 h | Single phase B2, cored |
| | [B2 matrix, Widmanstätten $\delta$, no coring] |
| 600°C, 100 h | Single phase B2, no coring |
| | [B2 matrix, Widmanstätten $\delta$] |
| 900°C, 10 h | Almost all Widmanstätten $\delta$ |
| | [Same as heat treated] |
| 900°C, 100 h | No sample available; probably same as tested sample |
| | [Almost all Widmanstätten $\delta$ |
| 1100°C, 10 h | Sample not available; probably same as tested sample |
| | [All coarse Widmanstätten $\delta$ |
| **40Ti Alloy** | |
| As-cast | Single phase B2, no coring |
| | [Same as as-cast] |
| 600°C, 10 h | Single phase B2 |
| | [Single phase B2] |
| 600°C, 100 h | Single phase B2 |
| | [Single phase B2] |
| 900°C, 10 h | Single phase B2 |
| | [Single phase B2] |
| 900°C, 100 h | Sample not available; probably same as tested sample |
| | [B2 matrix, grain goundary $\delta$] |
| 1100°C, 10 h | Not examined, probably single phase B2 |
| | [Single phase B2] |

The coring in the 25Ti alloy is not removed upon aging for 10 hours at 873 K (600°C), but it is removed after 100 hours. Aging at 873 K (600°C) for 100 hours and at 1173 and 1373 K (900 and 1100°C) for 10 hours produced all Widmanstätten $\delta$ in the microstructure.

The heat treatments for the 40Ti alloy produced the same structure as the as-cast condition, single phase B2. Note that this composition is in the single phase region at 1473 K (1200°C) (Figure 2.4).

### 5.2.2 Microstructure of Heat Treated Alloys after Testing at 900°C

The microstructures of the alloys after testing at 1173 K (900°C) at a strain rate of $10^{-4}$ $s^{-1}$, which required 15 minutes at 1173 K (900°C), are listed in Table 5.2 in brackets. The microstructures of the 10Ti alloy are the same as before testing except in the sample heat treated for 100 hours at 873 K (600°C), where some $\delta$ formed during testing. That is, an additional 15 minutes at 1173 K (900°C) (during testing) produced the $\delta$ phase.

The 25Ti alloy contained only B2 after aging at 873 K (600°C), but after testing at 1173 K (900°C) Widmanstätten $\delta$ was present. The samples aged at 1173 and 1373 K (900 and 1100°C) all contained Widmanstätten $\delta$ after heat treatment, and had the same structure after testing. The 40Ti alloy showed no significant change in the microstructure after testing for all aging temperatures (all B2).

### 5.2.3 Effect of Heat Treatment on Yield Strength

The yield strength data for the Group II alloys are shown in Figure 4.22 as a function of aging temperature. The yield strengths of the three alloys after aging at 873 K (600°C) for 10 and 100 hours are essentially the same as those for the as-cast condition. Table 5.2 shows that for aging at 873 K (600°C), there is no change in the microstructure for the 40Ti alloy. The 25Ti alloy shows additional Widmanstätten $\delta$, but the amount was similar to that of the as-cast condition. For the 10Ti alloy, there was no change in the structure after aging, although a small amount of $\delta$ formed in the 100 hours specimen during testing at 1173 K (900°C). Figure 4.22 shows a marked increase in strength with more Nb (less Ti), and it appears that this is responsible for the strength increase, since the structures do not change appreciably.

Aging had only a slight effect on the yield strength of the 40Ti alloy, at all aging temperatures (Figure 4.22). Table 5.2 shows that the microstructure in all cases was the same as that for the as-cast condition (B2).

Aging at 1173 and 1373 K (900 and 1100°C) increased the strength for the 25Ti alloy. At 1173 K (900°C), the 100 hour sample was appreciably stronger than the 10 hour sample (Figure 4.22). The approximate amount of the $\delta$ phase in the microstructure before testing is shown as bracketed numbers in Figure 4.22. The main microstructural change due to aging is the appearance of the appreciable amounts of $\delta$, and this is assumed to be the cause of the higher strength. For the

10Ti alloy, Figure 4.22 shows that aging for 100 hours at 1173 K (900°C) increased the strength significantly over that for aging 10 hours. The longer aging time did produce more $\delta$, and this is taken as the cause of the higher strength.

The highest strength is for the 10Ti alloy aged for 100 hours at 1373 K (1100°C) and 100 hours at 1173 K (900°C) (Figure 4.22), and the microstructures show more $\delta$ than for the as-cast condition or after aging at 873 k (600°C). However, the amount of $\delta$ for the higher strength conditions is not greatly different than that of the sample aged for 10 hours at 1173 K (900°C). Generally, though, for the 10 and 25Ti alloys, the increase in strength with aging temperature and aging time seems to be associated with increasing amounts of $\delta$. However, note that the 25Ti alloy samples aged for 100 hours at 1173 K (900°C) and 1373 K (1100°C) for 100 hours had almost all $\delta$, yet their strength is less than that of the 10Ti alloy which contained only 30 to 40 % $\delta$. It is assumed that the high amount of the high Nb-content (75% Nb) B2 matrix is what makes the 10Ti alloy stronger.

## 5.3 Summary

Compression tests have been conducted on Nb-Al-Ti alloys containing 15 at. % Al and 10, 25 and 40 at. % Ti, in the as-cast condition and after heat treatment. Tests were conducted at 298, 673, 873 and 1173 K (25, 400, 600 and 900°C) at strain rates of $5x10^{-2}$, $10^{-4}$ and $10^{-5}$ $s^{-1}$ for the alloys in the as-cast condition. The microstructure was characterized by optical, scanning electron and transmission

electron microscopy. For a given strain rate and test temperature, for the as-cast condition the 0.2% compressive strength increased with decreasing Ti content (increasing Nb content). The as-cast 25 and 40 % Ti alloys were single phase with the ordered B2 structure. The 10 % Ti alloy had Widmanstätten $\delta$ side plates in a B2 matrix. The strength increase is due to solid solution strengthening of the B2 phase and the presence of $\delta$. The $\delta$ phase showed cracks in both the as-cast condition and after testing.

For each alloy and all test temperatures, the compressive strength increased with strain rate and with decreasing test temperature. The stress-strain curves showed serrated yielding at the lower strain rates and test temperatures of 673 and 873 K (400 and 600°C), its origin was not established. A drop in stress-strain curves occurred when tested at 1173 K (900°C), and transmission electron microscopy indicated that this was due to dynamic recovery.

The as-cast material was aged at 873, 1173 and 1373 K (600, 900 and 1100°C) for 10 and 100 hours prior too testing at 1173 K (900°C) at a strain rate of $10^{-4}$ $s^{-1}$. For all heat treatments, the strength of the 40Ti alloy remained the same as for the as-cast condition. The strength of the 10Ti and 25Ti alloys increased considerably after aging 100 hours at 1173 K (900°C) and 10 hours at 1373 K (1100°C). For a given alloy, the strength increased due to the formation of the $\delta$ phase. The 10Ti alloy had a considerably higher yield strength than the 25Ti alloy, and it had a strength considerably higher than the 40Ti alloy. The increase

in strength with increasing Nb content is due to solid solution strengthening of the ordered B2 phase.

# CHAPTER VI

# CONCLUSIONS AND RECOMMENDATIONS

## 6.1 Conclusions

As-cast Nb-Al-Ti alloys containing 15 at.% Al and 10, 25 and 40 at.% Ti were tested in compression at 298, 673, 873 and 1173 K (25, 400, 600 and 900°C) at strain rates from $10^{-5}$ to $5x10^{-2}$ $s^{-1}$, to a strain of 5 %. The yield strength decreased with increasing temperature for each alloy at all strain rates, and increased with increasing strain rates. The stress-strain curves showed serrated yielding at test temperatures of 673 and 873 K (400 and 600°C) and the lower strain rates. The cause of this was not determined. All alloys showed a yield point drop when tested at 1173 K (900°C), and transmission electron microscopy indicated this was due to recovery occurring during testing. The Ti content (and hence the Nb content) had a marked effect of strength. At a given strain rate and test temperature, the strength increased considerably with increasing Nb content (decreased with increasing Ti content). This was attributed to solid solution strengthening of the ordered B2 structure, and in the 10% Ti (75% Nb) alloy, to the presence of some $\delta$ phase.

Aging treatments were carried out after which compression testing was con-

ducted at 1173 K (900°c) at a strain rate of $10^{-4}$ $s^{-1}$. Aging the 40% Ti alloy for 10 and 100 hours at 873, 1173 and 1373 K (600, 900 and 1100°C) did not change the strength significantly. Aging the 10 and 25% Ti alloy for 10 hours at 1173 K (900°C) did not significantly change the strength, but aging for 100 hours increased it about 20%. Aging for 10 hours at 1373 K (1100°C) increased the strength 30 to 40% above that of the as-cast level. For a given alloy, the increase in strength correlates with increasing amounts of $\delta$ formed during aging. As was found for the as-cast condition, there is a marked increase in strength with less Ti (more Nb) content and this is believed due to solid strengthening of the B2 matrix.

## 6.2 Recommendations

The primary recommendation is that a more detailed study of the dislocation characteristics be conducted. It would be especially useful to examine the dislocation generation in the as-cast condition by in-situ observations during straining. The formation of dislocations as plastic deformation initiates might be more useful in explaining the strength than observations after a few percent strain.

The fine dark particles present were not identified, and they should be examined to see if they are, for example, oxides or carbides.

It is also recommended that a chemical analysis be obtained of group I alloys. This is needed to determine if the chemistry differences of the two group of alloys is responsible for the considerable difference in strength of the two group of alloys

in the as-cast condition.

Heats should be prepared of sufficient size of the three alloys to allow tensile testing. This is important to establish a measure of the ductility.

A study should be made of the effect of additional elements to the Nb-Al-Ti base compositions on the strength. Since the strength is increased by the presence of the $\delta$ phase, but it is brittle, a search for additions which will alter the morphology of the $\delta$ to minimize cracking, e.g., form $\delta$ as a fine precipitate or spheroidized particles, should be initiated.

# BIBLIOGRAPHY

# BIBLIOGRAPHY


[1] J. M. Larsen, K. A. Williams, S. J. Balsone, and M. A. Stucke. Titanium aluminides for aerospace applications. In S. H. Whang, C. T. Liu, D. P. Pope, and J. O. Stiegler, editors, *High Temperature Aluminides and Intermetallics*, pages 521–556. Warrendale, PA, TMS, 1990.

[2] A. H. Rosenstein. Overview of research on aerospace metallic structural materials. *Materials Science and Engineering A*, A143:31–41, 1991.

[3] P. J. Bania. An advanced alloy for elevated temperatures. *Journal of Metals*, 40(3):20–22, 1988.

[4] J. H. Westbrook. *Intermetallic Compounds.* New York: John Wiley & Sons, Inc., 1967.

[5] E. P. George, M. Yamaguchi, K. S. Kumar, and C. T. Liu. Ordered intermetallics. *Annu. Rev. Mater. Sci.*, 24:409–451, 1994.

[6] I. M. Brzeski and I. E. Hack. Strain aging embrittlement of the ordered intermetallic compound NiAl. *Materials Science and Engineering A*, A170:11–18, 1993.

[7] M. Aindow, J. Shyue, T. A. Gaspar, and H. L. Fraser. Concerning the dissociation of growth-in dislocations in the melt spun ribbons of the intermetallic compound $Nb_3Al$. *Philosophical Magazine Letters*, 64(2):59–65, 1991.

[8] S. J. Balsone. The effect of elevated temperature exposure on the tensile and creep properties of Ti-24Al-11Nb. In T. Grobstein and J. Doychak, editors, *Oxidation of High Temperature Intermetallics*, pages 219–234. Warrendale, PA, TMS Publication, 1989.

[9] F. Ebrahimi and B. J. G. DeArago. High temperature deformation of a Nb-Ti-Al alloy with $\sigma + \gamma$ microstructure. *Mat. Res. Soc. Symp. Proc.*, 364:1247–1252, 1995.

[10] J. K. Tien, G. E. Vignoul, and M. W. Kopp. Materials for elevated-temperature applications. *Materials Science and Engineering A*, A143:43–49, 1991.

[11] E. A. Loria. Development of ductile Nb-Ti-Al alloys: Perspective and selected successes. In K. Natesan, P. Ganesan, and G. Lai, editors, *Heat-Resistant Materials II*, pages 613–619, Gatlinburg, Tennessee, 1995.

[12] R. M. Imayev, O. A. Kaibyshev, and G. A. Salishchev. Mechanical behavior of the fine grained TiAl intermetallic compound—I. superplasticity. *Acta Metall. Mater.*, 40(3):581–87, 1992.

[13] R. M. Imayev, O. A. Kaibyshev, and G. A. Shlishchev. Mechanical behavior of the fine grained TiAl intermetallic compound—II. ductile-brittle transition. *Acta metall. mater.*, 40(3):589–595, 1992.

[14] F. Popille, L. P. Kubin, J. Douin, and S. Naka. Portevin-Le Châtelier instabilities and stoichiometric effects in B2 titanium aluminides. *Scripta Materialia*, 34(6):977–984, 1996.

[15] D. E. Albert and G. T. gray III. Mechanical and microstructural response of Ti-24Al-11Nb as a function of temperature and strain rate. *Acta mater.*, 45(1):343–356, 1997.

[16] H. T. Kestner-Weykamp, C. H. Ward, T. F. Broderick, and M. J. Kaufman. Microstructures and phase relationships in the $Ti_3Al$ + Nb system. *Scripta METALLURGICA*, 23:1697–1702, 1989.

[17] E. S. K. Menon, P. R. Subramanian, and D. M. Dimiduk. Phase transformations in Nb-Al-Ti alloys. *Metallurgical and Materials Transactions A*, 27A:1647–1659, 1996.

[18] D. H. Hou and H. L. Fraser. The ordering scheme in complex intermetallic compounds. In W. O. Soboyejo, T. S. Srivatsan, and H. L. Fraser, editors, *Deformation and Fracture of Ordered Intermetallic Materials III*, pages 613–622, Cincinnati, Ohio, 1996.

[19] D. Banerjee, T. K. Nandi, and A. K. Gogia. Site occupation in the ordered beta phase of ternary Ti-Al-Nb alloys. *Scripta Metallurgica*, 21:597–600. 1987.

[20] J. Shyue, D. H. Hou, S. C. Johnson, and H. L. Fraser. Phase stability, deformation mechanisms, and mechanical properties of Nb-Al-Ti alloys. In R. Darolia, J. J. Lewandowski, C. T. Liu, P. L. Martin, D. B. Miracle, and M. V. Nathal, editors, *Structural Intermetallics*, pages 631–635, Seven Springs Mountain Resort, Champion, Pennsylvania, 1993.

[21] E. S. K. Menon, P. R. Subramanian, and D. M. Dimiduk. Phase equilibria in niobium rich Nb-Al-Ti alloys. *Scripta Metallurgical et Materialia*, 27:265–270, 1992.

[22] J. H. Perepezko, Y. A. Chang, L. E. Seitzman, J. C. Lin, N. R. Bonda, T. J. Jewett, and J. C. Mishurda. High temperature phase stability in the Ti-Al-Nb system. In S. H. Whang, C. T. Liu, D. P. Pope, and J. O. Stiegler, editors,

*High Temperature Aluminides and Intermetallics*, pages 19–47. Warrendale, PA, TMS Publication, 1990.

[23] C. Suryanarayana and D. S. Lee. Phase relations in Ti-Al-Nb alloys at 1200°C. *Scripta Metallurgica et Materialia*, 26:919–924, 1992.

[24] M. A. Morris, M. Leboeuf, and E. Batawi. Effect of thermomechanical treatments on phase distribution and microstructure evolution of a Ti-48Al-2Mn-2Nb alloy. *Scripta Metallurgica et Materialia*, 32(1):71–76, 1995.

[25] K. S. Chan and Y. W. Kim. Influence of microstructure on crack-tip micromechanics and fracture behavior of a two-phase TiAl alloy. *Metallurgical Transactions A*, 23A:1663–1677, 1992.

[26] X. D. Zhang, T. A. Dean, and M. H. Loretto. Phase transformation and structural morphologies of Ti-50Al-2Nb-2Mn during the heat treatment. *Acta metall. mater.*, 42(6):2035–2042, 1994.

[27] Y. G. Li and M. H. Loretto. Microstructure evolution of Ti-48Al-xNb $\gamma$ intermetallics. *Acta metall. mater.*, 42(6):2009–2017, 1994.

[28] S. Naka, M. Marty M. Thomas, G. Lapasset, and T. Khan. Complex B2 aluminides of refractory metals: An attempt to explore novel alloy systems. In R. Darolia, J. J. Lewandowski, C. T. Liu, P. L. Martin, D. B. Miracle, and M. V. Nathal, editors, *Structural Intermetallics*, pages 647–656. Seven Springs Mountain Resort, Champion, Pennsylvania, 1993.

[29] S. Naka and T. Kham. Designing novel multiconstituent intermetallics: Contribution of modern alloy theory in developing engineered materials. *Journal of Phase Equilibria*, 18(6):635–649, 1997.

[30] L. A. Bendersky and W. J. Boettinger. Investigation of B2 and related phases in the Ti-Al-Nb ternary system. In C. T. Liu, A. I. Taub, N. S. Stoloff, and C. C. Koch, editors, *High-Temperature Ordered Intermetallic Alloys III*, volume 133, pages 45–50, Pittsburgh, PA, 1989. Materials Research Society.

[31] M. R. Jackson and K. D. Jones. Mechanical behavior of Nb-Ti base alloys. In K. C. Liddell, D. R. Sadoway, and R. G. Beautista, editors, *Refractory Metals: Extraction, Processing and Applications*, pages 311–320. The Minerals, Metals & Materials Society, 1990.

[32] D. L. Douglass and F. W. Kunz. *Columbium Metallurgy*. New York: Interscience, 1961.

[33] P. Kofstad. *High Temperature Oxidation of Metals*. New York: Wiley, 1966.

[34] E. Fromm and H. Jehn. Reactions of niobium and tantalum with gases at high temperatures and low pressures. *Vacuum*, 19:191–197, 1969.

[35] P. Elliott. Columbium-oxygen system. *Trans. Am. Soc. Metals*, 52:990–1014, 1959.

[36] J. L. Murray. *Phase Diagrams of Binary Alloys*. Mateials Park, OH, ASM International, 1987.

[37] U. R. Kattner, J. C. Lin, and Y. A. Chang. Thermodynamic assessment and calculation of the Ti-Al system. *Metallurgical Transactions A*, 23A:2081–2090, 1992.

[38] H. Okamoto. Al-Ti (Aluminum-Titanium). *Journal of Phase Equilibria*, 14:120–121, 1993.

[39] L. L. Jorda, R. Flukiger, and J. Muller. A new metallurgical investigation of the Niobium-Aluminium system. *Journal of Less-common Metals*, 75:227–239, 1980.

[40] C. E. Lundin and A. S. Yamamoto. The equilibrium phase diagram, niobium (columbium)-aluminum. *Transactions of the Metallurgical Society of AIME*, 236:863–872, 1966.

[41] L. Kokot, R. Horyn, and N. Iliew. The niobium-aluminium binary system phase equilibria at 1100°C and superconductivity of alloys. *Journal of Less-common Metals*, 44:215–219, 1976.

[42] K. Schulze, B. Rickes, and G. Petzow. Reactions of Nb-Al powder mixtures during sintering. *Journal of Less-common Metals*, 100:429–441, 1984.

[43] K. Pampus, K. Dyrbye, and B. Torp. Metastable phase formation by ion mixing of Nb-Al multilayers. *Journal of Mater. Res.*, 4(6):1385–1392, 1989.

[44] R. Bormann, F. Gartner, and K. Zoltzer. Application of the CALPHAD method for the prediction of amorphous phase formation. *Journal of Less-common Metals*, 145:19–29, 1988.

[45] T. B. Massalski. *Binary Alloy Phase Diagrams, 2nd Edition, Vol. 1*. Mateials Park, OH, ASM International, 1990.

[46] K. Schullze, G. Muller, and G. Petzow. Investigations on the metastable system Nb-Al. *Z. Metallkd.*, 79:763–766, 1988.

[47] K. Schullze, G. Muller, and G. Petzow. Preparation of ductile Nb-Al powders for the fabrication of $Nb_3Al$ superconductors. II. *Journal of Less-common Metals*, 158:71–79, 1990.

[48] L. Kammerdiner and H. L. Luo. Superconductivity in Nb-rich Nb-Al alloys. *Journal of Appl. Phys.*, 43:4728–4731, 1972.

[49] E. Hellstern, L. Schultz, R. Bormann, and D. Lee. Phase formation in mechanically alloyed Nb-Al powders. *Appl. Phys. Lett.*, 53(15):1399–1401, 1988.

[50] R. Bormann, D. Y. Yu, R. H. Hammond, A. Marshall, and T. H. Geballe. Phase transformation in metastable Nb-alloys. In Steeb and H. Warlimont, editors, *Rapidly Quenched Metals*, pages 879–882, Wurzgurg, Germany, 1985. Elservier Science Pubilishers B. V.

[51] J. R. Gavaler, A. J. Braginski, F. Greggi, and K. schulze. Formation of the A15 phase in the thin-film Nb-Al diffusion couples. *Journal of Appl. Phys.*, 61:659–669, 1987.

[52] E. A. Wood, V. B. Compton, B. T. Matthias, and E. Corenzwit. Beta-Wolfram structure of compounds between transition elements and aluminum, gallium and antimony. *Acta Cryst.*, 11:604–606, 1958.

[53] S. Steeb and R. Kelppler. Diffusion suntersuchungen in den System Mo-Nb, Mo-Al und Nb-Al mittels Mikrosonle. *Z. Naturforsch,*, 24A:1601–1606, 1969.

[54] K. Raetz and E. Saur. Untersuchungen zur Supraleitung im System Niob-Aluminium. *Z. Phys.*, 169:315–322, 1962.

[55] D. G. Konitzer, I. P. Jones, and H. L. Fraser. Site occupancy in solid solutions of Nb in the intermetallic compounds TiAl and $Ti_3Al$. *Scripta METALLURGICA*, 20:265–268, 1986.

[56] M. A. Morris and D. G. Morris. Strain localization, slip-band formation and twinning associated with deformation of a Ti-24at.%Al-11at.%Nb alloy. *Phil. Mag. A*, 63:1175–1194, 1991.

[57] A. K. Gogia, D. Banerjee, and T. K. Nandy. Structure, tensile deformation, and fracture of a $Ti_3Al$-Nb alloy. *Metallurgical Transactions A*, 21A:609–625, 1990.

[58] D. T. Hoelzer and F. Ebrahimi. An investigation of phase stability in the ternary niobium-titanium-aluminum system. In J. J. Stephens and I. Ahmad, editors, *High-Temperature Niobium Alloys*, pages 105–119. Warrendale, PA, TMS Publication, 1991.

[59] K. Kaltenbach, S. Gama, D. D. Pinatti, K. Schulze, and E. M. Henig. A contribution to the ternary system Al-Nb-Ti. *Z. Metallkde*, 80:535–541, 1989.

[60] U. R. Kattner and W. J. Boettinger. Thermodynamic calculation of the ternary Ti-Al-Nb system. *Materials Science and Engineering A*, A152:9–17, 1992.

[61] A. Zdziobek, M. Durand-Charre, J. Driole, and F. Durand. Experimental investigation of high temperature phase equilibria in the Nb-Al-Ti system. *Z. Metallkde*, 86:334–340, 1995.

[62] D. Banerjee, A. K. Gogia, T. K. Nandi, and V. A. Joshi. A new ordered orthorhombic phase in a $Ti_3Al$-Nb alloy. *Acta metall.*, 36(4):871–882, 1988.

[63] R. G. Rowe. $Ti_3AlNb$-based alloys outperform conventional titanium aluminides. *Advanced Materials and Processes*, 141(3):33–35, 1992.

[64] L. M. Hsiung and H. N. G. Wadley. Stability of the ordered orthorhombic phase in Ti-24Al-Nb. *Scripta Metallurgica et Materialia*, 27:605–610, 1992.

[65] K. Muraleedharan, A. K. Gogia, T. K. Nandy, D. Banerjee, and S. Lele. Transformations in a Ti-24Al-15Nb alloy: Part I. phase equilibria and microstructure. part II. a composition invariant $\beta_0 \rightarrow o$ transformation. *Metallurgical Transactions A*, 23A:401–431, 1992.

[66] L. A. Bendersky, W. J. Boettinger, and A. Roytburd. Coherent precipites in the b.c.c.orthorhombic two-phase field of the Ti-Al-Nb system. *Acta Metallurgica et Materialia*, 39(8):1959–1969, 1991.

[67] L. A. Bendersky, W. J. Boettinger, B. P. Burton, and F. S. Biancaniello. The formation of ordered $\omega$-related phases in alloys of composition $Ti_4Al_3Nb$. *Acta Metallurgica et Materialia*, 38(6):931–943, 1990.

[68] L. A. Bendersky, W. J. Boettinger, and F. S. Biancaniello. Intermetallic Ti-Al-Nb alloys based on strengthening of the orthorombic phase by $\omega$-type phases. *Materials Science and Engineering A*, A152:41–47, 1992.

[69] H. J. Levinstein, E. S. Greiner, and H. Mason. Observation of dislocations in $V_3Si$ single crystals. *Journal of Appl. Phys.*, 37:164–166, 1966.

[70] S. Mahajan, J. H. Wernick, G. Y. Chin, Nakahara, and T. H. Geballe. Plastic deformation of $V_3Si$ single crystals at elevated temperatures. *Appl. Phys. Lett.*, 33:972–974, 1978.

[71] L. F. Vereshchagin, Y. S. Konyayev, E. M. Berzon, M. V. Veller, and A. V. Gulyutin. Influence of hydroextrusion on the composition of the compound $Nb_3Sn$. *Fiz. metal. metalloved*, 32:198–199, 1971.

[72] U. Essmann, H. Haag, and G. Zerweck. Dislocations in $V_3Si$. *Communications on Physics*, 2:127–130, 1977.

[73] R. N. Wright and K. A. Bok. A15 compound defromation and secondary slip in $V_3Si$. *Metallurgical Transactions A*, 19A:1125–1127, 1988.

[74] G. W. Groves and A. Kelly. Independent slip systems in crystals. *The Philosophical Magazine*, 8:877–887, 1963.

[75] J. D. Cotton and M. J. Kaufman. A simplified method for determining the number of independent slip systems in crystals. *Scripta METALLURGICA et MATERIALIA*, 25:2395–2398, 1991.

[76] S. S. Yang, D. H. Hou, J. Shyue, R. Wheeler, and H. L. Fraser. Pseudo-twinning in a deformed Nb-15Al-25Ti B2 alloy. *Mat. Res. Soc. Symp. Proc.*, 364:1359–1364, 1995.

[77] R. Strychor, J. C. Williams, and W. A. Soffa. Phase transformations and modulated microstructures in Ti-Al-Nb alloys. *Metallurgical Transactions A*, 19A:225–234, 1988.

[78] J. Shyue, D. H. Hou, M. Aindow, and H. Fraser. Deformation mechanisms in intermetallic compounds based on $Nb_3Al$. *Materials Science and Engineering*, A170:1–10, 1993.

[79] W. A. Rachinger and A. H. Cottrell. Slip in crystals of the caesium chloride type. *Acta Metallurgica*, 4:109–113, 1956.

[80] E. P. Lautenschlager, T. Hughes, and J. O. Brittain. Slip in hard-sphere CsCl models. *Acta Metallurgica*, 15:1347–1357, 1967.

[81] M. G. Mendiratta and C. C. Law. Dislocation energies and mobilities in B2-ordered Fe-Al alloys. *J. Mat. Sci.*, 22:607–611, 1987.

[82] J. A. Peters and C. Bassi. Isothermal transformations in a $\beta$-stabilised $Ti_3Al$ intermetallic. *Scripta METALLURGICA et MATERIALIA*, 24:915–920, 1990.

[83] L. M. Hsiung, W. Cai, and H. N. G. Wadley. Microstructure and phase evolution in rapidly-solidified Ti-24Al-11Nb. *Materials Science and Engineering A*, A152:295–303, 1992.

[84] H. T. Weykamp, D. R. Baker, D. M. Paxton, and M. J. Kaufman. Continuous cooling transformation in $Ti_3Al$ + Nb alloys. *Scripta METALLURGICA et MATERIALIA*, 24:445–450, 1990.

[85] P. B. Aswath and Suresh. Fatigue crack growth behavior of a titanium aluminide intermetallic. *Materials Science and Engineering A*, A114:L5–L10, 1989.

[86] S. M. L. Sastry and H. A. Lipsitt. Ordering transformations and mechanical properties of $Ti_3Al$ and $Ti_3Al$-Nb alloys. *Metallurgical Transactions A*, 8A:1543–1552, 1977.

[87] C. G. Rhodes. Effect of minor alloying additions on creep behavior of $Ti_3Al + Nb$. In P. Lacombe, R. Tricot, and G. Beranger, editors, *Sixth World Conference on Titanium*, pages 199–204, Cannes, France, 1989. Society Francaise de Metallurgie.

[88] R. Wheeler, S. Perungulam, D. H. Hou, S. Banerjee, and H. L. Fraser. Deformation mechanisms at intermediate temperatures in a ternary Nb aluminide compound. In W. O. Soboyejo, T. S. Srivatsan, and H. L. Fraser, editors, *Deformation and Fracture of Ordered Intermetallic Materials III*, pages 409–418, Cincinnati, Ohio, 1996.

[89] David B. Williams and C. Barry Carter. *Transmission Electron Microscopy*. Plenum Press, New York and London, 1996.

[90] J. T. Kandra and E. W. Lee. Temperature and microstructural dependence of the deformation of a high Nb Ti-Al alloy. *Metallurgical and Materials Transactions A*, 25A:1667–1679, 1994.

[91] L. Blaz and A. Korbel. Effect of multipeak dynamic recrystallisation on structure of deformed and annealed copper. *Materials Science and Technology*, 5:1186–1190, 1989.

[92] N. Ridley. Superplastic microstructures. *Materials Science and Technology*, 6:1145–1156, 1990.

[93] R. E. Goforth and M. N. Strinivasan. Testing the superplastic flow characteristics of advanced aluminum alloys. *Journal of Testing and Evalution*, 40:36–43, 1993.

[94] A. Durta and N. C. Birla. Effect of thermomechanical processing on superplasticity in Ti-Al-Mo-Zr alloy. *Materials Science and Technology*, 4:341–347, 1988.

[95] M. T. Cope, D. R. Evetts, and N. Ridlry. Post-forming tensile properties of superplastic Ti-6Al-4V alloy. *Materials Science and Technology*, 3:455–467, 1987.

[96] M. T. Cope and N. Ridlry. Superplastic deformation characteristics of microduplex Ti-6Al-4V alloy. *Materials Science and Technology*, 2:140–145. 1986.

[97] Y. Combres and C. Levaillant. Effects of microstructure on superplastic behavior of nickel based superalloy NK17CDAT. *Materials Science and Technology*, 6:705–713, 1990.

[98] T. G. Nieh, C. M. McNally, and J. Wadsworth. Superplasticity in intermetallic alloys and ceramics. *Journal of Materials*, 41:31–35, 1989.

[99] H. S. Yang, P. Jin, and A. K. Mukherjee. Superplastic behavior of regular $\alpha_2$ and super $\alpha_2$ titanium aluminides. *Materials Science and Engineering A*, A153:457–464, 1992.

[100] B. Mintz, J. J. Jonas, and Abu-shosha. Effects of grain refinement and grain coarsening on shapes of dynamic recrystallization flow curves for C-Mn-Al steels. *Materials Science and Technology*, 7:904–913, 1991.

[101] S. Wierzbinski, A. Korbel, and J. J. Jonas. Structural and mechanical aspects of high temperature deformation of polycrystalline nickel. *Materials Science and Technology*, 8:153–158, 1992.

[102] R. M. Imayev, V. M. Imayev, and G. A. Salishchev. Formation of submicrocrystalline structure in TiAl intermetallic compound. *Journal of Materials Science*, 27:4465–4471, 1992.

[103] F. R. Castro-Fernandez and C. M. Sellars. Static recrystallisation and recrystallisation during hot deformation of Al-1Mg-1Mn alloy. *Materials Science and Technology*, 3:621–627, 1988.

[104] N. Srinivasan and Y. V. R. K. Prasad. Characterisation of dynamic recrystallisation in nickel using processing map for hot deformation. *Materials Science and Technology*, 8:206–212, 1992.

[105] H. I. Aaronson. In V. F. Zacky and H. I. Aaronson, editors, *Decomposition of Austenite by Diffusional Processes*, pages 387–546. New York, Interscience Publishers, 1962.

# VITA

Dah-Liang Guan was born in Hsinchu, Taiwan, the Republic of China, on January 20, 1954. He graduated from Chung Cheng Institute of Technology, Taiwan in August 1977 with a Bachelor of Science degree. He earned a Master of Science degree from Chung Cheng Institute of Technology in July 1984. He enrolled in the University of Tennessee, Knoxville, to continue his education in May 1994 and received his Doctor of Philosophy degree in Metallurgical Engineering in May 1998.

He married to Yuh-Ju Lan in 1986 and they have one daughter and one son. He has been working as an engineer for research in Taiwan.